# UNIVERSIDAD DE CIENCIAS Y ARTES DE CHIAPAS

**INSTITUTO DE INVESTIGACIÓN E INNOVACIÓN EN ENERGÍAS RENOVABLES**

# TESIS

## "DRY REFORMING OF METHANE VIA USE OF $Ni$, $Pt$ AND $Mo$ OVER COMBINED SUPPORTS"

QUE PARA OBTENER EL GRADO DE DOCTOR

**EN MATERIALES Y SISTEMAS ENERGÉTICOS RENOVABLES**

PRESENTA

**JOSEF GALTHIER ROBLERO LUCCHETTI**

DIRECTOR(ES)

**DR. JOSÉ FRANCISCO POLA ALBORES**
**DR. MIGUEL ÁNGEL VALENZUELA ZAPATA**

Tuxtla Gutiérrez; Chiapas Septiembre de 2020

Tuxtla Gutiérrez, Chiapas a 24 de septiembre de 2020
**Oficio No.** DGIP/CP/0158/2020

**Asunto:** Autorización de impresión de tesis

**M.C. Josef Galthier Roblero Lucchetti**
**Candidato al Grado de Doctor en Materiales y Sistemas Energéticos Renovables**
**Instituto de Investigación e Innovación en Energías Renovables**
**UNICACH**
**P r e s e n t e**

Con fundamento en la **opinión favorable** emitida por escrito por la Comisión Revisora que analizó el trabajo terminal presentado por usted, denominado **"Dry Reforming of methane with Synthetic Biogas Mixtures via use of Ni, Pt and Mo over Combined Supports"**, cuyos directores de tesis son los Doctores José Francisco Pola Albores y Edna Iris Ríos Valdovinos, quienes avalan el cumplimiento de los criterios metodológicos y de contenido; esta Dirección General a mi cargo **autoriza** la impresión del documento en cita, para la defensa oral del mismo, en el examen que habrá de sustentar para obtener el **Grado de Doctor en Materiales y Sistemas Energéticos Renovables.**

Es imprescindible observar las características normativas que debe guardar el documento impreso, así como realizar la entrega en esta Dirección General de un ejemplar empastado.

**Respetuosamente**
***"Por la Cultura de mi Raza"***

DIRECCION DE INVESTIGACION Y POSGRADO

**Lic. Aurora Evangelina Serrano Roblero**
**Directora General**

C.c.p. Dr. Pascual López de Paz, Director del Instituto de Investigación e Innovación en Energías Renovables, UNICACH. Para su conocimiento.
Dr. Roilán Iglesias Díaz, Coordinador de Posgrado, Instituto de Investigación e Innovación en Energías Renovables, UNICACH. Para su conocimiento.
Expediente

*AESR/igp/rags/gtr

"Progress is made by trial and failure. The failures are generally a hundred times more numerous than the successes, yet they are usually left unchronicled." – **William Ramsey**

"No hay refrán que no sea cierto, porque todos son hijos de la experiencia, la madre de todas las ciencias." – **Don Quijote**

# Dedication

To Galthier and Rosalía, who showed me life.

# Acknowledgements

First and foremost, I would like to thank Professors José Francisco Pola Albores and Miguel Ángel Valenzuela Zapata. Thanks to their different but good-natured personalities, I found a perfect balance during my time in the lab. Also in my Committee, Dr. Edna Ríos Valdovinos proved to be an astute observer and posed difficult but interesting and necessary questions at important times.

Secondly, even though she was not officially my advisor, Prof. Elizabeth Rojas García was indispensable in the development of my thesis and taught me much regarding characterization. Like my advisors, she is a great human being. Prof. Carlos Meza was always extremely helpful with characterization of materials, and I thank him profusely.

I would also like to thank *The Boys* who started their master's degree just as I started my PhD in 2016 at UNICACH, some of whom have become great friends of mine. Special thanks to Juan Carlos, Jairo, Alfredo, Vicente and Edwin for the great laughs. As for *The Ladies*, thanks to Cousin Andrea, and Adriana, our hard-working Secretary. The latecomers were also a great enhancement to my studies. Thank you for the good times, Weimar (Alfa), David (Bravo), Rocío, Isra, Alina and María.

I would also like to thank the undergrad kids, some of whom became students of mine and are surely underway to great achievements. Special thanks to Didier, Carolina, Darwin, Giselle, Ana (Rho), Elienaí (Sigma), Diana Squarepants, Monserrat and Koller.

My time in Mexico City would not have been worthwhile without the great company at the laboratory of materials characterization at IPN-Zacatenco. Special thanks to Brian, Josué, Robin, Natalia, Karina, Maggy, Dr. José Manuel and Dr. Fernando Plascencia.

Even though we only spent a few weeks together, I would like to thank the German team for the good times at Hochschule Emden-Leer. It was wonderful to be with German Volk once again. Thanks, M. Eng Lena Peters and Eng. Wilfried Paul. Dr. Preseela from India, you too are remembered kindly.

Last but not least, I would like to thank my Maddy, who has been loyal company for many years.

# Abstract

Firstly, synthesis of catalysts was carried out over different types of silicas and a few alkaline supports. Some samples were subjected to a carburization process with $CH_4$ to synthesize metallic carbides. Secondly, these materials were then characterized via X-Ray Fluorescence (XRF), X-Ray Diffraction (XRD), $N_2$-Physisorption, $H_2$-Temperature-Programmed Reduction ($H_2$-TPR), Raman spectroscopy and High-Resolution Transmission Electron Microscopy (HR-TEM). Catalytic tests were evaluated over brief and long-term periods. Some evaluations focused only on carbon deposits, which only took place over nickel/silica mixtures. Finally, spent catalysts were also characterized, mostly by Raman spectroscopy, although XRD and monitoring of carbon formation (by weight) on catalysts also took place. Overall, nickel and nickel-platinum catalysts had higher conversions of $CH_4$ and $CO_2$, which reached an estimated 90% at their point of highest activity. Catalysts with higher conversions were those deposited on Cach, a silica with a high specific surface area (450 $m^2/g$) created at Universidad de Ciencias y Artes de Chiapas. Active phases deposited on a commercial silica (Ald) showed no conversion of reactants. A similar trend was observed for Ni-Mo catalysts on both kinds of silica, but with lower conversions. Combined use of MgO-Cach-Ni-Pt resulted in stable conversions due to formation of solid solutions, as demonstrated by $H_2$-TPR. Carbon monitoring showed that there were greater carbon accumulations on Ni-SBA than over Ni-Cach and Ni-Ald, which can be related to activity of the catalytic materials, or lack thereof. This trend was also observed via Raman spectroscopy and XRD, the latter also revealing the presence of carbon nanotubes. Lastly, carbon studies via Raman showed that catalysts already containing carbon before DRM (due to carburization process) had a greater prevalence of disordered carbon (D band) than samples without carbon, as well as graphene-related Raman bands (D' band).

# Resumen

Primeramente, la síntesis de catalizadores se llevó a cabo sobre diferentes tipos de sílices y algunos soportes alcalinos. Algunas muestras fueron sometidas a un proceso de carburación con $CH_4$ para sintetizar carburos metálicos. En segundo lugar, estos materiales se caracterizaron entonces a través de XRF, XRD, $N_2$-Physisorption, $H_2$-TPR, Espectroscopia Raman y HR-TEM. La siguiente fase fue la evaluación catalítica, que se dividió en estudios a corto y largo plazo. Algunas evaluaciones se centraron únicamente en los depósitos de carbono, que sólo tuvieron lugar sobre mezclas de níquel/sílice. Por último, los catalizadores gastados también se caracterizaron, principalmente por la espectroscopia Raman, aunque también tuvo lugar la XRD y la formación de carbono de monitoreo físico (en peso) en catalizadores. En general, los catalizadores de níquel y níquel-platino tuvieron mayores conversiones de metano y $CO_2$, que alcanzaron un 90% en su punto de mayor actividad. Los catalizadores con conversiones más altas fueron los depositados en Cach, una sílice que fue sintetizada en la Universidad de Ciencias y Artes de Chiapas, que tenía una superficie alta específica (450 $m^2/g$). Cuando las fases activas fueron depositadas sobre una sílice comercial (Ald), se logró poca o ninguna conversión de reactivos. La tendencia fue similar con los catalizadores Ni-Mo para ambos tipos de sílice, aunque las conversiones fueron mucho más bajas. El uso de MgO combinado con Cach y Ni-Pt dio lugar a conversiones estables debido a la formación de soluciones sólidas, como lo demuestra $H_2$-TPR. Por su parte, el monitoreo de carbono mostró que había mayores acumulaciones de carbono en Ni-SBA que sobre Ni-Cach y Ni-Ald, que pueden estar relacionados con la actividad de los materiales catalíticos, o la ausencia de actividad. Esta tendencia también se observó a través de la espectroscopia Raman y XRD, este último también revela la presencia de nanotubos de carbono. Por último, los estudios de carbono a través de Raman mostraron que los catalizadores que ya contenían carbono antes de DRM (debido al proceso de carburación) tenían una mayor prevalencia de carbono desordenado (banda D) que las muestras sin carbono, así como las bandas Raman relacionadas con el grafeno (banda D').

# Table of Contents

**Content**

# List of Tables

# List of Figures

# Nomenclature

| Abbreviation | Meaning |
|---|---|
| ΔG | Free Gibbs Energy variation |
| ADF | Acid Detergent Fiber |
| ADL | Acid Detergent Lignin |
| Ald | Silica by Sigma-Aldrich (used for catalyst nomenclature) |
| BET | Brunauer-Emmet-Teller |
| BJH | Barrett-Joyner-Halenda |
| Cach | Silica developed at UNICACH university |
| CALCOR | Process for CO generation |
| CTAB | Cetrimonium Bromide ($C_{19}H_{42}BrN$) |
| DRM | Dry Reforming of Methane |
| FWHM | Full Width at Half Maximum |
| GHSV | Gas Hourly Space Velocity |
| HR-TEM | High Resolution Transmission Electron Microscopy |
| $H_2$-TPR | Temperature-Programmed Reduction |
| NDF | Neutral Detergent Fiber |
| PDF | Pattern Diffraction File |
| PEI | Polyethanolimine |
| $R_s$ | Stability coefficient for metallic carbides |
| SBA-15 | Santa Barbara Amorphous material |
| SPARG | Sulfur-Passivated Reforming process |
| TCD | Temperature-Controlled Desorption |
| TEOS | Tetraethyl orthosilicate |
| TMB | Trimethylbenzene |
| XRD | X-Ray Diffraction |
| XRF | X-Ray Fluorescence |
| VOA/TIC | Ratio of Volatile Organic acids to carbonate buffer capacity |

# Foreword

The world has produced fuel from food products for many years. Ethanol has been considered as a low-cost alternative fuel that reportedly uses less pollution and increases the gasoline supply via blending. It has also been described as better for the environment, as it offers an alternative to fracking. In a way, it can reduce environmental impact by reducing the need for transcontinental pipelines. However, this process has a huge drawback. It destines millions of tons of food to the production of ethanol. The scientific consensus has been warning that the continued use of basic foods for energy purposes might make hunger problems worse on the planet. Food that would otherwise be exported or sent as aid to impoverished countries is now being used for creating liquid fuels. Examples of food products range from grains to roots such as cassava, sugarcane, corn, and rice plantations or fields. Oil palm and jatropha trees are also planted for these purposes. Thus, large areas that could be allocated to growing food are being used for production of ethanol. Water resources should also be taken into consideration. Using thousands to millions of cubic meters of water for growing food that is to be consumed can be easily justified, whereas apportioning it for food meant for energy production is not so commendable, especially when there are dozens of planets with a population that is uncapable of feeding itself. Ironically, land is being provided for growing crops that will be used for energy purposes in countries that have some of the largest concerns regarding food supplies, namely African countries. If the use of crops for ethanol production increases, there is fear that food itself might become more expensive.

Another aspect of food that should be taken into account is waste from the agricultural industry, as it can be used for generation of biogas. This type of waste can be found in every

farm, town and city on the planet. The production of biogas is a field of study that has become increasingly relevant in the renewable energies realm. Biogas is seen as a supplement to wind and solar energy, as it can supply electricity during times when these other supplies fail. However, other promising applications exist, such as catalytic conversion. Such technologies involve first and foremost the generation of syngas from biogas, which can be achieved in different manners. Multiple reforming methods exist that are capable of transforming methane or carbon dioxide into hydrogen-rich products. Conversely, the products may have a greater CO content or an $H_2$/CO ratio of 1. These syngas mixtures can then be transformed into a wide variety of fuels, depending on the catalyst used and on the ratio of its components. Even though these methods have been studied greatly, there is a race to develop new materials and methods that reduce problems during reforming that are mostly related to temperature and carbon deposits. Energy input into these systems can also make fuel production more challenging, but this is a problem that can be solved via creative options such as solar reforming. Finetuning of these catalytic pathways and synthesis of materials are leading industry towards a promising new path that could contribute to improving environmental conditions by reducing emissions, and that could decrease our dependence on petroleum-based products. Even though we owe petroleum most of our current progress, it is also true that it is the source of military conflicts and environmental destruction. Catalytic conversion of biogas, be it a by-product from farms or an industrial synthetic mixture, might just be the gateway to a cleaner and safer world.

# Chapter 1:

# Introduction and Motivation

The world's energy consumption is on an upward trend, and conventional energy sources are limited and becoming rapidly depleted [1]. Many fuel sources used presently have very negative traits, such as pollution, destruction of wild habitats and urban areas, as well as unfavorable economic balance sheets. Although large reservoirs of coal, gas and oil are suspected of being in deep water, exploitation of these sources is complicated, and their extraction can be extremely hazardous, as has been proven in the Gulf of Mexico spill by Deepwater Horizon [2]. In many cases, the search for oil entails invading areas that have remained untouched for millennia, such as reserves in the Arctic.

Some alternatives to conventional fuel that have been used on a large scale are oil sands, shale gas, and nuclear energy. In the case of tar sands or shale gas, their extraction leads to high levels of water and air pollution due to the excessive use of chemicals during extraction. Wastewater derived from the extraction process is also a factor that needs to be taken into consideration [3]. Tar sands involve heavy use of fuel during bitumen extraction, and the ratio of gained energy to invested energy can be as low as a factor of 3.

Disasters such as Chernobyl and Fukushima, the latter still unsolved, show that, in the use of nuclear energy, risks clearly outweigh the benefits. Finally, geopolitical conflicts can be usually be traced down to disputes over oil and pipeline resources that are still easily accessible [4]. Trafficking of oil from Syria to Turkey during the early years of the Syrian conflict clearly shows that natural resources are a major cause for war [5]. Both nuclear disasters and armed conflicts should be included within energy crises, as they have dire consequences on quality of life [6]. In a nutshell, there are plenty of political and environmental motivations as to why the age of oil and nuclear fuel can become cumbersome to our current lifestyles.

Taking all the previous information into account, the use of renewable energies is a plausible option for the government and private sectors, as they can usually be easily identified and studied without putting entire human settlements and ecosystems at risk, although a downside always exists to any new implementation of technology. In addition to hydropower, solar, wind and geothermal energies, a highly explored option is known as methane reforming, whose goal is usually the synthesis of molecular hydrogen from methane. In addition, a highly coveted product is a mixture known as synthesis gas or *syngas,* which consists of molecular hydrogen and carbon monoxide. Generally speaking, reforming processes can be applied to liquid fuels such as methanol or ethanol [7, 8], and even for longer molecules [9]. The main challenge in any methane reforming is the $CH_3$-H link partition, which has a high dissociation energy of 493 kJ $mol^{-1}$ [10]. When reforming methane with $CO_2$, the reaction is known as dry reforming.

$$CO_2 + CH_4 \rightleftarrows 2CO + 2H_2 \quad \Delta H^{\circ}_{298} = +247.19 \text{ kJ mol}^{-1} \qquad \textbf{(R1)}$$

Human activities have resulted in the release of large amounts of $CO_2$ into the atmosphere, which have been reported to be as large as 30 GT in one year. The most significant increases in $CO_2$ emissions from natural gas consumption were reported in China, Egypt, Mexico and Russia, with 86%, 63%, 28% and 17%, respectively [11]. It is important to know where Mexico lies in this context as it may lead to deeper research regarding the sources of emissions. Solutions that could hinder the release of $CO_2$ into the atmosphere could be its storage or its immediate use as a raw chemical in later reactions. Storage of $CO_2$ is unfeasible in the long run, as storage capacity and compression capabilities require greater expenses. Thus, using $CO_2$ in reforming reactions is a highly recommendable alternative.

Much effort has been put into converting methane to synthesis gas as an option to keep carbon dioxide emissions under control in the energy landscape. This way, a carbon-neutral energy cycle can be developed. Most research and development taking place regarding synthesis gas applications has been conducted on Fischer-Tropsch, as well as generation of hydrogen, methanol, ethanol, mixed alcohols, substitute natural gas [12]. Further downstream processes involve processing of methanol, such as methanol to diesel, methanol to gasoline, methanol to olefins and generation of dimethylether.

Commercial methane reforming usually takes place at higher temperatures, which improves reaction rates due to thermodynamic shifts which allow spontaneous reactions to occur. It is typical to see a temperature range between 500 and 800 °C for reforming reactions, although the trend is to reduce temperatures as much as possible. Such elevated temperatures will include gas-phase reactions, such as methane decoupling or cracking, which can also be restructured into other molecules, such as ethylene. Thus, the catalyst should be optimized to ensure greater yields of the intended products. Reaching these temperatures implies high energy investments, but interesting solutions have been implemented in the past, such as solar reforming.

The beginnings of methane reforming go back to Paul Sabatier and Senderens, who at the beginning of the twentieth century developed the mechanism of catalytic hydrogenation of carbon monoxide to produce methane and water vapor at 250 °C. That is, synthesis gas was used to produce methane [13]. A few decades later, Fischer and Tropsch developed the reforming of methane with carbon dioxide in the presence of nickel and cobalt catalysts, reporting severe deactivation of catalysts due to carbon deposition. In 1975, Kokarev *et al*., began to study reforming applications. The methodology used by them

resembles partial oxidation reform due to use of air. Their goal was to introduce reformed gas into a glass casting system. The reformed gas had a high carbon content, which was then subjected to a flame, thus forming $CO_2$. Due to a feed rich in carbon, the temperature of the flame to which the gas was directed did not decrease [14].

One of the main drawbacks of dry reforming is the deposition of carbon. The reactions that generate carbon deposits are cracking of methane and the Boudouard reaction, which are shown in section 2.6. This can be solved by the creation of small active phase nanoparticles. Beyond a certain limit (7 nm), carbon deposition is guaranteed. If the smaller particle size is achieved, a high dispersion of the active phase is to be expected. There are many ways of increasing this dispersion, such as the use of materials rich in mesopores supports and the use of carrier materials or secondary supports which can generate solid solutions.

Based on the information provided in this introduction, there are three main lines that will be highlighted in this doctoral dissertation.

- First, the design of a suitable carrier material that will allow the creation of smaller particle or crystal sizes in the active phase is a major target.
- Secondly, the evaluation and robustness of monometallic and bimetallic materials in the dry reforming reaction is something that will be widely explored in this work. This does not exclude the formation of complicated and rarely reported compounds, and the compositions intended initially may come to differ, as proven by XRD.
- Lastly, the conditions used in dry reforming of methane are extreme, guaranteeing the formation of different types of carbon deposits. Therefore, these are to be studied separately, as well as the conditions that may lead to carbon-free reactions.

# Chapter 2:

# Theoretical Concepts and Background Studies

## 2.1 Syngas Production and its Relationship with Biogas

The main techniques used to obtain hydrogen on a large scale exploit the processes of reforming light hydrocarbons, especially methane, which is the predominant component in natural gas and biogas. It is worthwhile to mention that several routes produce synthesis gas, also widely used in industries. Obtaining high purity $H_2$ is a costly process, as CO must be removed first [15]. Because of these high expenses, using synthesis gas directly for other purposes is an alternative application. In cases where higher $CO_2$ content is required for synthesis, it is possible to compensate with external sources, which may be of very different natures.

The term synthesis gas is used to describe a mixture containing $H_2$ and CO, along with small amounts of $CO_2$ and $CH_4$. Synthesis gas can be produced from natural gas, refinery discharge gases, heavy hydrocarbons and from coal [16]. Important sources of material for the production of synthesis gas are biogas and biomass [15, 8]. The use of biomass by pyrolytic methods for the generation of synthesis gas has been described in past research [17, 18]. These can be applied to algae, wood waste, crop waste and food processing [19].

Biogas is seen as an energy source that can supplement solar and wind energy on days when there is not enough solar incidence or wind, respectively. However, it can be destined to more complex processes other than simply combusting to obtain electricity. Biogas is formed as a natural process due to multiple ordered transformations that are carried out by different groups of bacteria [20]. The most used sources of biogas are animal manure, food waste, silage, and crops. Depending on the source, biogas can have incredibly variable compositions, which make it highly optimal for catalytic conversion applications. $CO_2/CH_4$

mixtures in a 1:1 ratio are optimal for dry reforming, which in turn creates a 1:1 $H_2$/CO product. However, these methods are highly flexible, especially when oxygen is used as a reactant gas, which can create quasi-tailored syngas combinations. Different combinations are very useful for further catalytic applications, such as fuel production. A general view of the biogas to fuels pathway is depicted in figure 1. Annex B has been dedicated completely to information regarding biogas production and analyses, according to the doctoral stay at Hochschule Emden University of Applied Sciences, in Germany.

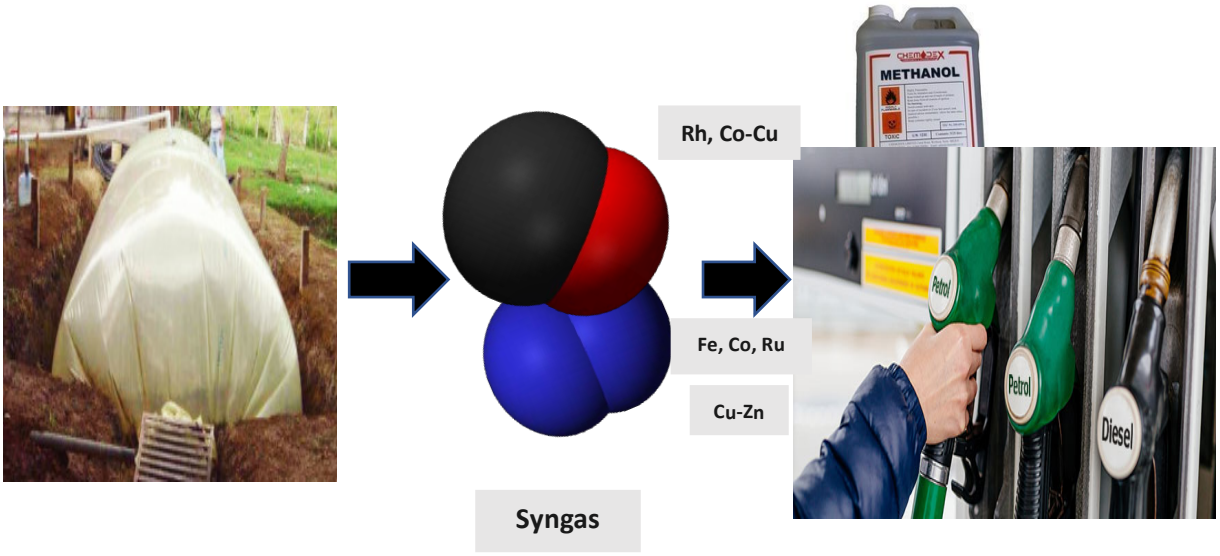


**Figure 1**. From Biogas to Syngas to Fuels.

The selection of the raw material depends on the costs and availability of the raw material, and perhaps more importantly, the end use of the synthesis gas. Synthesis gas has application in the chemical and refining industries, electricity generation, urea and ammonia synthesis, electronic applications and in the production of alternative energies because it is a

reagent for the Fischer-Tropsch process [21]. Synthesis gas applications are shown in figure 2.

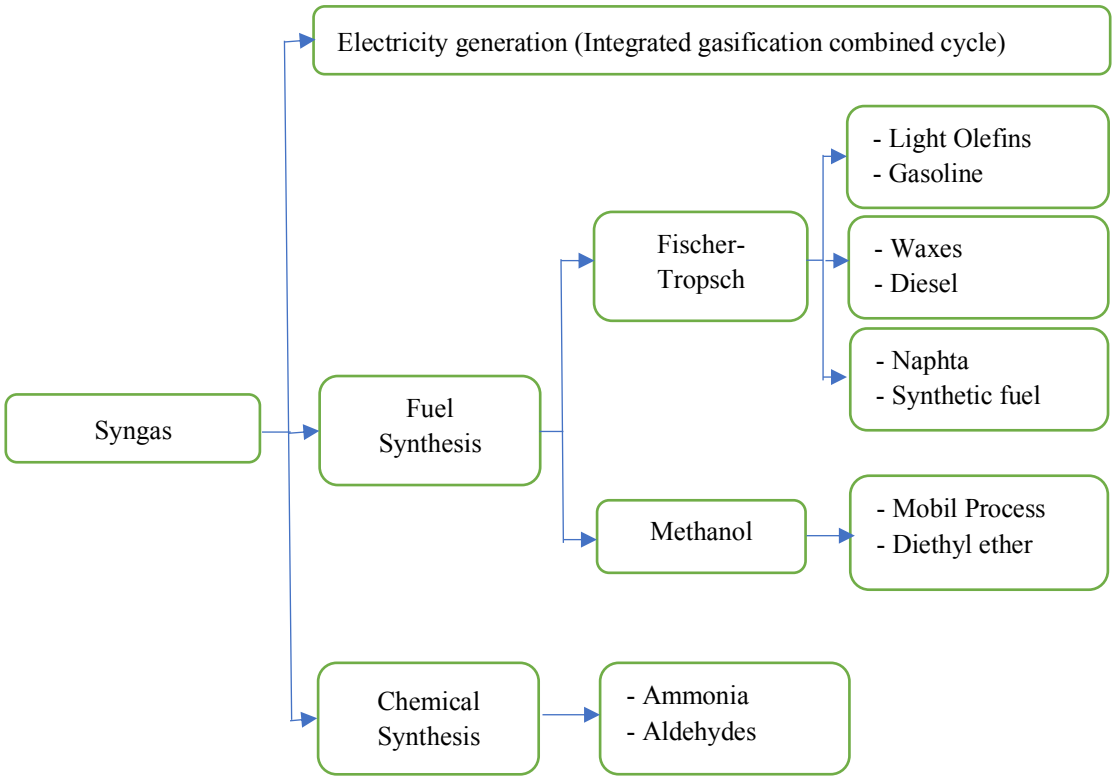


**Figure 2.** Synthesis gas applications for the development of fuels and industrial products.

## 2.2 Types of Reforming

Reforming is a processing technique by which the molecular structure of a hydrocarbon is modified or rearranged, to alter its properties. This kind of procedure is usually applied to low-quality fuels to improve their combustion properties [22]. In the case of methane, its reforming aims to produce either hydrogen or synthesis gas. In general, all methane reform reactions produce CO, albeit in different $H_2$:CO ratios. The production of synthesis gas can be carried out by many reactions, although not all have shown the same

effectiveness. Therefore, at least three pathways are used on an industrial scale, whereas others remain in laboratory or pilot plant phases. The most used methods are steam reforming of methane, partial oxidation reforming and autothermal reforming [23]. There are other explored pathways, which are dry reforming and dry oxidation reforming. Dry reforming of methane (DRM), known also as $CO_2$ reforming of methane, has been known to produce carbon deposits, which then saturate sites of catalytic activity. However, carbon deposition seems to be an obstacle that is being overcome quickly in recent years.

### 2.2.1 Steam Reforming

Steam reforming is an industrial-scale process that involves two reactions, which transform water and $CH_4$ into CO and $H_2$. The process can be summarized in a series of 4 steps, the first of which is the heating of water in a boiler above 800 °C. The generated steam is mixed with $CH_4$ and enters the reforming tubes, and the temperature is kept at temperatures ranging between 650 and 800 °C with help of burners. High temperatures and an active phase form carbon monoxide and molecular hydrogen. The active phase is usually nickel, although there are multiple alternatives. The mixture leaves the reaction tubes, and CO enters the *water gas shift* reactor (WGS), where it reacts with water and generates more amounts of $CO_2$ and $H_2$. After a process involving pressurization, adsorption, and depressurization, $H_2$ leaves the process with a high degree of purity. Despite being a highly energy-demanding endothermic method, it is the most widely used for hydrogen production, and has a yield of up to 70% [15].

$$CH_4 + H_2O \rightleftarrows CO + 3H_2 \qquad \Delta H^{\circ}_{298} = +206.02 \text{ kJ mol}^{-1} \qquad \textbf{(R2)}$$

## 2.2.2 Partial Oxidation Reforming

Partial oxidation reforming uses pure oxygen at high pressures and temperatures. This reaction is exothermic, unlike steam reforming. A source of $CH_4$ is mixed and preheated with oxygen in a reactor. The equipment consists of a partial oxidation reactor, synthesis gas turbine and heat exchangers for the recovery of detached heat, an air separation unit and an oxygen compressor [24]. Oxygen enters through an air separation unit. In a burner they react in a turbulent diffusion flame. Steam is used to maintain an adequate temperature in the process. The turbine activates the air separation unit and compressor and expands the synthesis gas flow to generate power. Heat exchangers preheat the $CH_4$ source and oxygen flow, and use the residual heat contained in the synthesis gas stream that leaves the turbine. The composition of the synthesis gas is controlled by the $CH_4$:$O_2$:$H_2O$ proportion [25]. If an $H_2$/CO molar ratio of 2 is desired (optimal for synthetic diesel generation via Fischer-Tropsch reaction), the $CH_4$:$O_2$:$H_2O$ proportions in the feed is 1.5:1:1 [24]. Due to exothermal conditions, the reaction is conducted autothermally, exceeding 1000 °C. This results in high reaction rates, and therefore in high catalyst space-time yields [26]. That is, the contact time required to trigger the reaction is less than 50 milliseconds. This is orders of magnitude shorter than for the reforming of methane with water vapor.

$$\boldsymbol{CH_4} + \frac{\mathbf{1}}{\mathbf{2}}\boldsymbol{O_2} \rightleftarrows CO + 2H_2 \qquad \Delta H^{\circ}_{298} = -35.96 \text{ kJ mol}^{-1} \qquad \textbf{(R3)}$$

### 2.2.3 Autothermal Reforming

Autothermal reforming combines the thermal effects of partial oxidation and steam reforming reactions, as the reactor is fed with $CH_4$, water and air simultaneously. This route can decrease the maximum temperature in the reactor and increase the $H_2$:CO ratio, as compared to the partial oxidation process. Similar to partial oxidation reforming, the composition of synthesis gas can be controlled by a variation in the constituents of the fed gases. Another important advantage is the speed at which the reactor can be stopped and reactivated. These properties make autothermal reforming a feasible option for hydrogen generation. However, this alternative presents limitations, as increasing the water to $CH_4$ ratio in the feed (as of 4:1), can bring the reaction to a halt due to extinction temperatures being achieved. Also, excess oxygen can give preference to combustion instead of increasing the frequency of reforming reactions [27].

### 2.2.4 Dry Oxidative Reforming

This technique provides a strategy that solves the deposition of carbon during reforming. This requires a simultaneous introduction of oxygen, $CH_4$ and $CO_2$ in the co-feed. The addition of oxygen makes the overall reaction more exothermic, which allows a reduction in the total energy used and eventually requires the addition of little energy. In addition to increasing methane conversions, the use of oxygen contributes as a safeguard against deactivation.

As in autothermal reforming and partial oxidation, the $H_2$:CO ratio is manipulated by controlling oxygen amounts in the inlet. This way, deposed carbon disappears again with an increase in temperature [15].

An experimental setup has been described very thoroughly in recent studies [28]. After the manifold, gases were introduced into the reactor. Products flowed through a condenser and a drying material prior to being injected into a gas chromatograph and an emission analyzer. The best methane conversions (100%) were achieved at 725 °C when adding a $O_2/CH_4$ ratio of 0.3 and 0.5. A higher amount of $O_2$ in the feed resulted in decreased $CO_2$ conversions, which improved upon increasing temperature. The results of these experiments are shown in figure 4. It is observable that a smaller amount of oxygen will decrease methane conversions but increase $CO_2$ conversions.

$$\boldsymbol{CH_4} + \beta\boldsymbol{CO_2} + \frac{(\mathbf{1}-\beta)}{\boldsymbol{2O_2}} \rightleftarrows (\mathbf{1}+\beta)\boldsymbol{CO} + \boldsymbol{2H_2} \qquad \Delta H^{\circ}_{298} = \text{-35.96 kJ mol}^{-1} \qquad \textbf{(R4)}$$

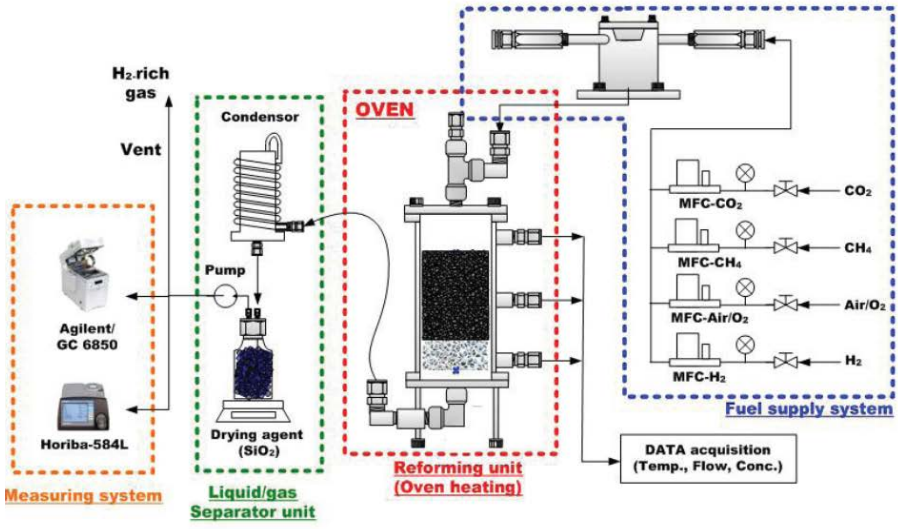


**Figure 3.** Reaction system used for dry oxidative reforming at the laboratory level. Taken from [28].

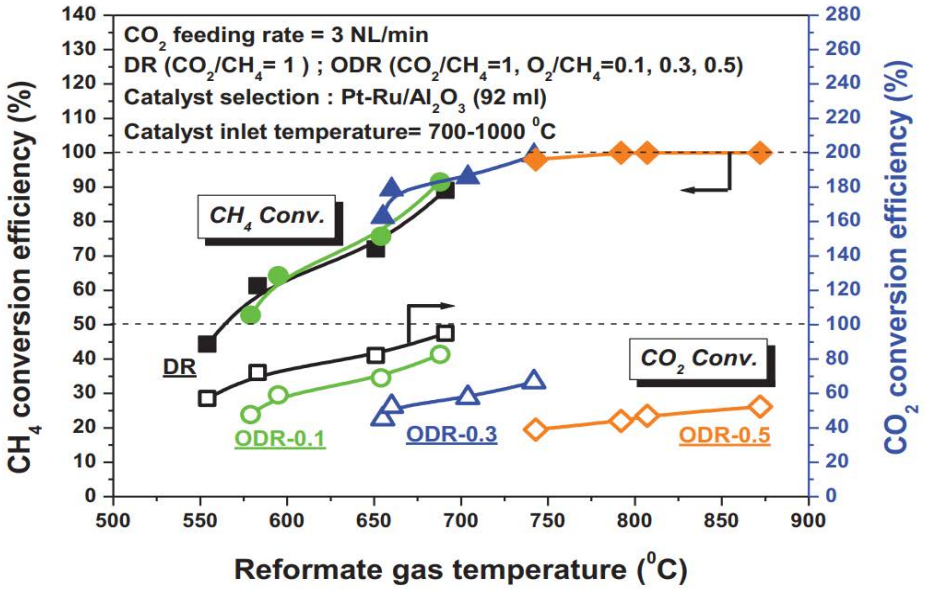


**Figure 4.** Dry oxidative reforming reported with modification of $O_2$ to $CH_4$ ratios, which has an influence on methane and $CO_2$ conversions [28].

## 2.3 Fixed Reaction Beds

Fixed bed catalytic reactors are one of the most important reactors for the synthesis of chemical and intermediate materials. The reactions occur as heterogeneously catalyzed gas reactions and take place on the surface of catalysts that have been inserted into the reactor's fixed bed [29].

Fixed beds for synthesis operate continuously and on a long-term basis. Therefore, the design is concentrated on optimal stationary operation. Those exhibiting a strong exothermic character often exhibit efficient operational behavior. The main component of a fixed bed reactor is the catalyst itself, as well as the reaction site, even if supported. The process can be divided into the steps mentioned below.

1. Diffusion of reactants from the gaseous space to the particle border where the pores are found in the material.
2. Chemisorption in active centers.
3. Surface reactions.
4. Product desorption.
5. Reversed diffusion of products into gaseous space.

Although there are several proposed steps for catalytic processes, the steps mentioned above are essential. Additional stages that can be included are the diffusion stages into and out of the catalytic material.

## 2.4 Catalysts, Supports and Promoters in Reforming

The development of new catalysts, particularly those of great stability and durability in reforming processes, can ensure the reduction of high temperatures used for chemical reactions. New catalysts can also increase in the speed of reaction and at the same time a decrease in the deactivation of the reaction system [15]. Factors that may lead the reaction to and end are the presence of impurities that can deactivate the catalyst, such as sulfur or hydrogen sulfide, or the appearance of coking by different phenomena that will be mentioned in section 2.5.2.1.

Due to market costs, some of the most used catalysts are Ni and Co. There are limitations that can occur when using monometallic catalysts. Therefore, many investigations have been conducted with combinations of Ni and alkaline metals such as Na, MgO, K and $La_2O_3$ [30]. Thanks to these additions, outstanding results have been obtained, as will be discussed in later sections.

Metal active phases that have high prices on the market are Pt, Rh and Ru. These have yielded both positive and negative results, sometimes with high $CO_2$ and $CH_4$ conversions [31, 32], and in other cases lower conversions [33]. These results demonstrate that noble metals are not necessarily a guarantee in obtaining high $H_2$ and CO yields, as compared to traditionally used metals, such as Ni and Co. In fact, experiments with Ni outweigh those using noble metals, especially those using modern techniques, as will be seen in section 2.9.

The use of supports in reforming reactions aims to provide a high surface area for the active component [34]. It has been shown for the most part that the use of an unsupported catalyst results in a short-lived reaction, although the use of bulk catalysts has been reported [35, 36]. It is important to establish compatibility between the catalyst, the amount of the catalyst and the support. Hu and Ruckenstein demonstrated in 1996 that extremely strong interactions (meaning strongly chemisorbed components) between the catalyst metal and the support can exist, which reduces the effectiveness of the reaction [37]. The most used supports are Al, Mg, Si and Ce oxides. There are different types of support, but the feature in common is that they are usually oxides. It is believed that the use of alkaline supports may promote the chemisorption of $CO_2$, which has acidic properties. This attraction or activation can accelerate the overall reaction rate [38]. Activation can also improve contact time with the catalyst. It is important to note that a support functions as a dispersant of the active component in such a way that some deactivation issues are avoided. These issues will be covered in the next section.

To conclude this section, promoters will be described briefly. Promoters are agents designed to assist either the support or the catalyst. Although frequently found in small percentage quantities, it has major effects on catalyst activity, selectivity and stability. In

the case of dry reforming, they can contribute greatly to mitigating the effects of carbon, even contributing to its elimination [39]. In general, it has been observed that the addition of an alkaline promoter increases the dispersion of the active phase. That is, smaller active phase groups are formed, which also reduces particle size. By achieving this effect on size, the sintering chances are getting smaller and lower. Another phenomenon that is exacerbated is the interaction between the support and the metal. The addition of a promoter can also make $CO_2$ dissociation more efficient [40]. Finally, its presence can prevent the appearance of bimetallic compounds, in cases where the support and the active phase can be highly reactive amongst themselves.

## 2.5 Catalyst deactivation problems

Disabling a catalyst can have thermal, mechanical or chemical origins, although an interaction between these mechanisms is highly likely [34]. Both thermal and chemical forces can weaken a particle or groups of particles, and that way the result is mechanical modification. The most common causes of catalytic deactivation in dry reforming may be sintering, poisoning, and carbon deposition. Other causes of deactivation may be by particles from the reaction system (*fouling*) and compound formation [41].

### 2.5.1 Sintering

Sintering of a metal catalyst is a process in which diffusion of supported metal atoms occurs and they make up larger metal aggregates. This process is a direct consequence of time, temperature and age. It is a non-reversible phenomenon, so the original surface area of the metal or catalytic mixture cannot be recovered. When a catalytic material is prepared, the metal is finely dispersed by the support to maximize that surface area. Heating of the

supported catalyst during pre-treatment helps to increase the dispersion of metal particles. If the temperature exceeds certain limits, the metal particles migrate to form aggregates, reducing the dispersion achieved during the synthesis of the catalytic mixture. This effect directly reduces the number of active sites exposed to reagents, thereby drastically reducing catalytic activity. This process has been described many times in the past [42, 43, 41].

### 2.5.2 Poisoning

A poison is an impurity present in the fluid phase of reactants. This can react selectively with active sites, ending catalytic activity. The poisoning effect should be avoided as much as possible. Poisoning occurs by chemical reactions (chemical type) or by the presence of impurities (physical type). A closely related example of biogas and DRM is the presence of $H_2S$ and catalyst inactivation. A chemical type poisoning is irreversible if the reaction product is highly stable. If it is not stable, it can be removed by an appropriate chemical reaction. This process is called regeneration [44, 41].

Physical poisoning occurs when an external substance blocks access of fluids to the active surface. Dust, coke or particles embedded in the surface or pores enter in this category. In the case of coke formation, an oxidative process can reverse the effects of poisoning, although it is better to find catalytic mixtures that do not allow carbon deposits at all [34].

#### *2.5.2.1 Coking*

Coke is a general term used to describe carbon residues on the surface of a catalyst. It can vary in structure, from aromatic polymers to graphite. These deposits are found in amounts of up to 20% by weight of the catalyst when feeding a reaction system contains

carbon [34]. Most catalysts can experience this type of deactivation. In an extreme case, active sites can be wrapped or encapsulated by carbon, resulting in pores becoming blocked. Carbon deposition can occur by reactions that occur on acid supports, by dehydrogenation and by catalytic reforming. Any of these situations can occur in DRM, although deposition on acid supports and acidic site deterioration [45].

The presence of carbon has been equated with multiple deactivation scenarios. For example, the presence of carbon has been described as a form of poisoning on the metal surface, and as a pore and cavity obstructer, as well as physical disintegration of the active phase of the catalyst [46]. One of the most prevalent forms during DRM are carbon filaments [47]. These have great structural strength and can mechanically interfere with the catalyst and permanently deactivate it, thus beginning to accumulate in the reactor walls [48, 49]. Deactivation has been described as a change in reaction rate in major reactions, thus starting to show selectivity towards more parallel reactions. This phenomenon occurs along the catalytic bed and in the catalyst particle [50]. Carbon fiber growth is thought to come to an end as soon as they surround catalyst particles. In the case of dry reforming, the coating does not bring the reaction to its end, as long as a portion of the active phase is still in contact with the reactants. In this way, carbon deposits can be consumed in part. Carbon diffusion and segregation depend on the surface of the active phase, as some planes are more active than others [51].

There is a direct relationship between the structure of carbon deposits and reactants, as well as products formed during a reaction. The initial phase in the deposition of carbon is thought to be the dissociative chemisorption of $CH_4$ on the active metal surface, resulting in surface hydrogen and carbon. Carbon accumulation is the result of disbalance between

carbon formation and removal. This leads to the restructuring of the catalytic surface, which begins to block active sites [52]. Alternately, the dynamic balance between formation and removal will result in a stable catalyst, which depends on the presence of metal oxides [53]. Different coking structures can form by varying temperature, even when using simple reactants and catalysts [54]. It is important to note that the damage done by carbon deposits is more related to the structure and location of the coke, than to the quantities produced. However, carbon deposits can influence the flow of reactants through the catalytic bed, making carbon amounts something that must be avoided at all costs [55]. Ginsburg *et al.* (2005) stated that there are three routes for the deposition of carbon deposits, depending on temperature [56]. Temperatures above 450 °C induce the formation of carbon whiskers, which do not interfere with the activity of the metal phase [57]. However, clogged pores in the support can occur [58]. Temperatures below 500 °C form the hydrocarbon films by a combination of adsorption and polymerization processes. Hydrocarbon cracking occurs above 600 °C, resulting in carbon deposits. These last two carbon sources result in the creation of encapsulating films, which block and deactivate the catalytic surface. Specifically for DRM, the existence of intermediaries has been reported at 300 °C, due to the exchange reactions between $CH_4$ and $CO_2$ [59]. These intermediaries disappear at 600 °C. Other possible intermediaries are $C_2$ structures [60]. Elevated $CH_4$:$CO_2$ ratios from are highly responsible for the appearance of carbon deposits, something that has been extensively studied before [61].

Carbon formation has been explained as a function of particle size and the factors that affect it, such as the age of the catalytic bed and the degree of sintering in the batch [62]. There are older reports stating that the most prevalent forms among carbon deposits can be

encapsulating films and pyrolytic carbon. More recently, multiple forms of carbon have been reported, such as amorphous carbon, graphite, carbon nanotubes, and even graphene and structures similar to this [63, 64]. Other forms include adsorbed carbon or surface carbides, amorphous polymer films, amorphous fibers or whiskers, carbides, and crystalline graphic films. Nanofibers are a typical form of surface carbon [65]. Carbon whiskers are tubular graphic structures that tend to have the same diameter as that of metallic glass. On the other hand, graphite films spread across the metal surface, developing ordered layers that run parallel to the carbon-metal interface.

Bychkov *et al.* (2013) made detailed observations between nanofibers and carbon derived from carbides (carbide carbon) that appeared during DRM. They stated that nanofibers are less likely to participate in catalytic activity with nickel particles. Moreover, carbidic carbon is quickly formed and consumed during the reaction, depending on the temperature [66]. At 400 °C, $CH_4$ begins to be consumed, and the first traces of carbon are observed. The removal of carbon deposits is made possible by the presence of $CO_2$ via Boudouard's reaction starting at 500 °C. Carbide coal is considered a variant of graphitic carbon, as it is derived from metastable metal carbides [67]. The appearance of carbon nanotubes is mediated by nickel particles, appearing in large numbers on nickel and silica catalysts [68].

## 2.6 Dry Reforming: Background and State of the Art

This reaction is endothermic and involves the reaction between $CO_2$ and $CH_4$ (see Reaction 1). Due to reactants, this reaction is particularly attractive due to the possibility of using biogas directly [15]. An approximate composition of biogas is 50-70% $CH_4$ and 30-50% $CO_2$ [69], depending on the source used to produce biogas. Contaminants such as $H_2S$ exist in small amounts, which can be eliminated via adsorption processes. Methane and $CO_2$ have been linked to the greenhouse effect, so this route is an alternative to harnessing and eliminating both. However, the method needs great energy investments to reach temperatures between 700 and 900 °C needed for the reaction, which reduces the overall effectiveness of the reaction to eliminate $CO_2$. To heat 1 mole of biogas from 30 to 700 °C, considering a CH4/CO2 mix of 60%/40%, 34.61 kJ must be invested. Data for these calculations was found in thermodynamics tables [70]. If the mixture is to be heated up to 900 °C, 47.85 kJ are needed. This can be covered easily with less than 1 gram of natural gas. However, using renewable sources would reduce the need for fuel. See section 2.7.

From an industrial perspective, the dry reforming of $CH_4$ produces a ratio of $H_2$ to CO very close to 1, which makes it uninteresting to produce $H_2$, but is ideal for the equimolar production of synthesis gas. This reaction was shown in chapter 1.

There are three parallel reactions that can affect the generation of the synthesis gas, which are: reverse water gas shift, $CH_4$ cracking and Boudouard reaction (reactions 2, 3 and 4, respectively). Of these, the Bouduard reaction is exothermic, although reverse water gas shift and cracking are only slightly endothermal. Boudouard's reaction consists of the breakdown of CO, which also results in carbon deposition.

$$CO_2 + H_2 \rightleftarrows CO + H_2O \qquad \Delta H^{\circ}_{298} = +247.19 \text{ kJ mol}^{-1} \qquad \textbf{(R5)}$$

$$CH_4 \rightleftarrows C + 2H_2 \qquad \Delta H^{\circ}_{298} = +74.65 \text{ kJ mol}^{-1} \qquad \textbf{(R6)}$$

$$2CO \rightleftarrows C + CO_2 \qquad \Delta H^{\circ}_{298} = -172.54 \text{ kJ mol}^{-1} \qquad \textbf{(R7)}$$

Dry reforming is a method that received relatively little attention in the last decades of the 20th century. However, interest has increased in recent years due to the attractive possibility of reacting $CO_2$ and $CH_4$, which are two of the greenhouse gases that are impacting global temperatures. Figure 5 shows how a modification of catalysts can have an impact on the composition of syngas. This depiction was submitted for publication as a graphical abstract [71]. All credits for this image go to M.S. Juan Carlos Navarro Escobar from IIIER-UNICACH.

Alves *et al*. (2013) reported that in situations where $CH_4$ *cracking* occurs at a faster rate than carbon removal, coking is a serious problem [15]. Boudouard's reaction can generate carbon at low temperatures, between 550 and 700 °C. The carbon produced by this reaction is generally less reactive [72]. In general, cracking of methane becomes a greater problem as temperature increases. Thus, the biggest problem with DRM is coking formation, which can accumulate in the support or in the active phase of the catalyst. The consequences are then the deactivation of the catalyst and obstruction of the reactor.

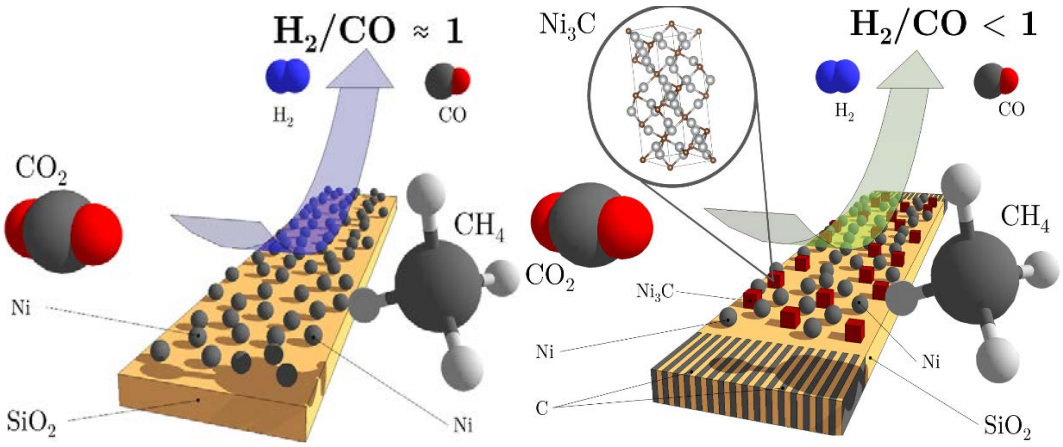


**Figure 5.** Image showing how a modification of the catalyst can render different compositions in the product [71].

Regarding particle size issues, Bychkov *et al*. observed that carbon is deposited if the particle is above 7 nm [66]. This same conclusion is in agreement with another research team, which also concluded that the formation of carbon filaments generates changes in the specific surface area [73].

In the case of nickel, there are crystalline phases that have a greater preference for breaking down methane than others. The Ni (100) and Ni (110) phases are more active than the Ni (111) phase. On the other hand, the carbon present in some phases tends to spread better in the catalytic lump than others. For example, carbon on Ni (110) can be better spread than carbon attached to Ni (100). Thus, surface phenomena are highly dependent on the crystalline phase [51].

## 2.7 Industrial applications for DRM

As mentioned previously, there are multiple difficulties in carrying out the DRM reaction. Because of this, it is also difficult to find large-scale applications of this reaction. Although there are well-developed plants for steam and autothermal reforming of methane, DRM has lagged somewhat in its development (but not at laboratory level). However, there are industrial and US government reports whereby DRM is used. These applications include the Sulfur-Passivated Reforming (SPARG) and Calcor systems, as well as the Sunexus solar reform system. A more recent case is that of the German company Linde, which is setting up a plant in the Bayern region.

The SPARG technique extends catalyst life by slight poisoning of active sites with $H_2S$, which is continuously added to the gas feed. This poisoning prevents the formation of excessive carbon deposits. As is well known, poisoning does not necessarily result in catalyst deactivation, but can modify selectivity. The passivation process results in low catalytic activity but enough activity remains in the catalyst to obtain high conversions of methane. In addition, an increase in temperature may be necessary to compensate for the loss of activity. A variation in $CO_2$ levels as well as the addition of steam allow the production of synthesis gas with an $H_2$:CO ratio lower than 1.8 [74]. Relating to DRM, and in the assumption that biogas can be used directly from the biodigestor, this technique could be used for academic installations, provided that a fraction of $H_2S$ is removed. Adsorption with help of ZnO has been described in the past [75].

For its part, the Calcor system generates larger amounts of CO in chemical manufacturing plants. The production and/or processing process is carried out only on site,

due to the risks associated with the transport of CO [74]. The system has been optimized to produce a few amounts of $H_2$. CALCOR requires the prior removal of sulfur impurities and does not depend on poisoning for its operation. The catalysts can be of different composition, and the system operates at high temperatures, but low pressure.

The Sunexus solar reformer was developed by the Renewable Energy Institute International (California, USA), with the participation of Sandia National Laboratories and Desert Research Institute, in Nevada and New Mexico, respectively. This project consisted of both pilot plant and industrial testing, as well as many quantitative analyses. The system consists of a solar concentrator and a set of tubular reactors loaded with nickel catalyst [76]. With the solar reformer, multiple tests were performed, whereby steam reforming of methane, DRM, birreforming and trireforming stand out. In addition to synthesizing a sintering-resistant catalyst, the report mentions the absence of carbon deposits. This catalyst also allowed some resistance to impurities such as ammonia, particulate matter, oxygen, non-methane hydrocarbons, and low concentrations of $H_2S$ (200 ppb) and HCl (20 ppm).

The system emulates designs used for steam reforming and other reforming applications. However, the heating mechanism is not placed in a lower, upper or lateral section. The solar reactor consists of a series of 30 U-tubes, placed in a circle and leaving a central space which will be heated by concentrated sunlight. Solar energy comes from a 12 kW solar disk (hub), which concentrates energy at a focal point in the central space mentioned above. The temperatures reported for DRM reach up to 900 °C, although they report excellent conversions at 800 °C for both methane and $CO_2$. The long-term tests were conducted for up to 1,750 hours. Finally, the effluent was connected to a system called "Pacific Renewable Fuels and Chemicals Process Development Unit", from which synthetic,

sulphur-free diesel was obtained with high ketane value (reverse ignition time), as well as high lubricating power. Figure 6 was extracted from the research carried out by Schuetzle *et al.* (2010), where details of a solar reformer can be seen [76]. Figure 7 shows a solar reformer once it has been attached to a concentrating dish, extracted from the same report.

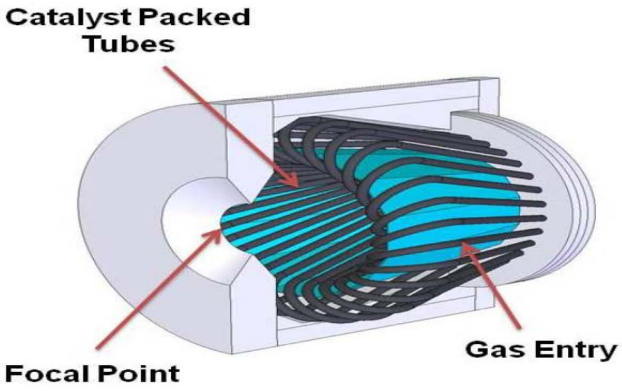


**Figure 6.** Solar reformer design showing area where maximum solar incidence is achieved, as well as location of catalyst. Taken from [76].

**Figure 7.** Sunexus solar reformer attached to a concentrating dish. Taken from [76].

Also, Figure 8 shows input data regarding a Lifecycle assessment made for the Sunexus reformer, whereby production of fuels from synthetic biogas is analyzed. By use of

solar systems, a reduction of $CO_2$ can be achieved. A similar analysis can be seen in section 2.9.1.

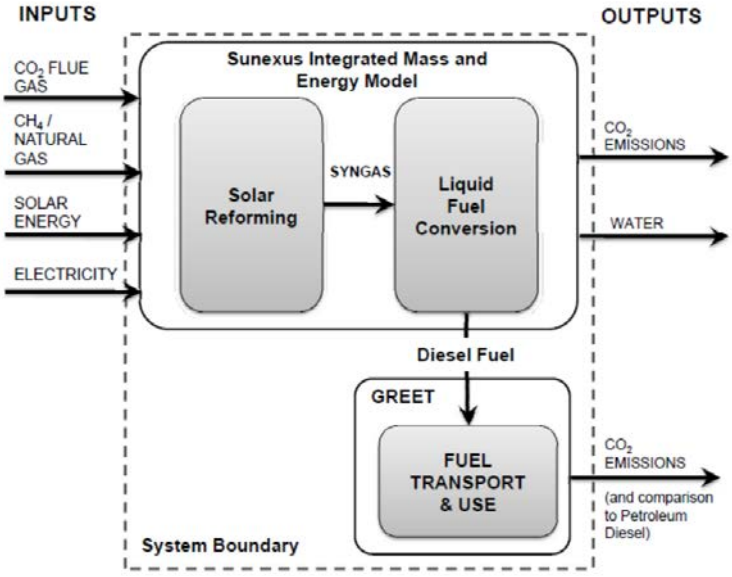


**Figure 8.** Lifecycle Assessment performed on production of fuels from synthetic biogas mixtures via dry solar reforming. Taken from [76].

Finally, two pilot projects are included in this section. The German company Linde (in conjunction with BASF and the Karlsruhe Institute of Technology) opened a pilot plant for DRM. This company specializes in the production of synthesis gas from natural gas, liquid gas, naphtha, waste oils and coal. This plant is located in Pullach, Bayern. The plant was installed to study and optimize all kinds of reforming processes. Currently, the level of success of this plant [77] is being determined.

Similarly, the Chiyoda Corporation implemented a process that combines dry reforming with steam reforming. It uses a low-quality natural gas and $CO_2$-containing waste gases for producing synthesis gas. The process is more efficient than the traditional process

of steam reforming. A proprietary material is used as a catalyst. Also, a demonstration plant called Japan-GTL was inaugurated, which produces synthesis gas [78].

## 2.8 Laboratory strategies for dry reforming of methane

As stated earlier, supported metal catalysts tend to be deactivated with high temperatures via sintering phenomena or irreversible reactions between metal and support. Therefore, the development of the catalytic system is the crucial stage DRM. It is necessary to take the existence of secondary reactions into account, as well as the need to maximize the conversions of the reactants at a given temperature. Also, there are multiple factors that can improve the performance of a catalyst. These include surface area, presence of basic sites, metal dispersion of the active phase, the interaction between the support and the active phase. While the trend in research is focusing on all the aspects mentioned above, the search for more robust interactions between support and active phase is where efforts in DRM are directed. Before reviewing the latest advanced synthesis techniques, a brief recount will be provided of the work that was carried out before the year 2000 by Ruckenstein and Hu, as well as the research with metallic carbides by Brungs, Thomson and a few other authors. Research wherein third components were added to traditional materials or techniques will also be mentioned. Towards the end, the most modern catalysts that are currently being developed will be mentioned.

### 2.8.1 Research by Ruckenstein and Hu

Ruckenstein and Hu investigated in 1995 the impact on DRM when using NiO in combination with alkaline earth metallic oxides. These were the MgO, CaO, SrO and BaO. Mixtures were prepared by impregnation of alkaline earth metal oxides with an aqueous nickel nitrate solution [79]. The paste was left to dry at room temperature and calcined at 800 °C for 1.5 hours. The reaction was carried out at atmospheric pressure in a flow system, using a quartz tube as a reactor, and the catalyst powder was sustained in quartz wool. A molar ratio of 1 was maintained between feed gases. The catalyst was reduced with a flow of $H_2$ to 500 °C, and reaction temperature was 790 °C. The effectiveness of catalyst mixtures was also investigated without reduction of oxides. The total time investigated for reduced catalysts was 120 h, while for non-reduced catalysts it was approximately 24 hours. Conversion via the reduced Ni/Mg catalyst produced conversion rates above 90%, for both $CO_2$ and $CH_4$, while CO and $H_2$ yields were also very high. On the other hand, the unreduced catalysts showed little effectiveness, except for the NiO/CaO mixture during the first hours of testing. A similar catalytic material was synthesized by Shamsi (2006), which was composed of Ca/Ni/K, but the method of synthesis is not disclosed [80]. This material made by Shamsi stayed on stream for 360 hours at 800 °C without deactivating.

Finally, the effect of gas hourly space velocity (GHSV) was investigated with use of two flows and with the NiO/MgO catalyst. This final test showed that a larger feed (60,000 ml $g^{-1}$ $h^{-1}$) produces higher CO yields (up from 90%), since a lower (approx. 25,000 ml $g^{-1}$ $h^{-1}$) reduces performance to as little as 60%. From this it could be assumed that a more turbulent flow contributes to more points of contact with the catalyst, or that it allows a shorter contact time between the non-alkaline and methane areas. However, other reports

describe an opposite effect. That is, increasing the GHSV value reduces the conversion rates [81, 38]. This is because a higher space velocity value is interpreted as a shorter contact time between the reactants and the catalytic material (inverted value of τ, which is given in $V_{cat}/V_0$). $V_{cat}$ is the volume of the catalyst bed, and $V_0$ is the value of the gas feed.

In 1997 they stated that the effectiveness of DRM depends on the conditions under which the catalyst is prepared. Also, Ruckenstein and Hu later discovered that the addition of small amounts of chlorine further improved the stability of the catalytic mixture [82].

Ruckenstein and Hu demonstrated in 1996 the importance of using a support and the variation of the percentage levels by weight of the catalyst [37]. The effect of reducing NiO without support and with an $Al_2O_3$ support was investigated. They also compared the conversion and performance rates between NiO and $NiO/Al_2O_3$, $NiO/SiO_2$ (1% of Ni after reduction) and $NiO/Al_2O_3$, $NiO/SiO_2$ and $NiO/TiO_2$ (containing approx. 14% by weight of Ni after reduction). The unsupported and unreduced Ni showed a relatively high conversion rate of both $CO_2$ and $CH_4$ (approx. 60 and 80%, respectively), before the first hour of reaction was completed. Subsequent measurements resulted in little to no conversion. The reduced and unsupported Ni had negligible conversion rates from the outset. Meanwhile, unreduced $NiO/Al_2O_3$ mixture was initially much more effective than the reduced mix in the performance and conversion of $CO_2$ and $CH_4$. However, after 24 hours of reaction, measurements for reduced and unreduced mixtures began to converge (about 45% for all). $NiO/Al_2O_3$ and $NiO/SiO_2$ blends with 1% Ni reduced showed high conversion rates initially, which began to decline steadily. In contrast, the non-reduced catalysts (with 1% Ni) started with lower conversion values, which raised slowly but never exceeding 30% for the whole study. Mixtures containing $Al_2O_3$ were highly effective in all cases. The use of Ti in the

support produced strong interactions between metal and support, which resulted in lower CO yields. Carbon formation was less visible in the mixtures $NiO/Al_2O_3$ and $NiO/SiO_2$ with 1% Ni. However, the mixture of 14% Ni with alumina generated enough deposed carbon to stop the experiment after 6 hours. The $NiO/SiO_2$ blend with 14% Ni maintained high activity (close to 90% CO yield) for 50 hours of testing. This article demonstrates that the presence of a support does not play an auxiliary role in the reforming process but is essential for a prolonged catalytic activity. On the other hand, it shows that the likelihood of a reduced catalyst being more effective than an unreduced catalyst is greater. Thus, a greater amount of active phase does not necessarily translate in high conversions of $CH_4$ and $CO_2$, and activity will depend instead on the type of support.

Ruckenstein and Hu also investigated the effect of precursor molecules and MgO support preparation conditions on dry reforming [82]. In this research they mixed MgO with NiO. The precursors that gave rise to MgO were $Mg(NO_3)_2$ , $Mg(OH)_2$ and $(MgCO_3)_4$ and $Mg(OH)_2$. They were prepared in contact with air by calcination at different temperatures, which ranged from 400 to 1100 °C to a maximum of 3 hours. The catalyst contained approximately 13% weight of Ni. Following the same procedure with the 1995 experiment, the catalytic reaction was performed at atmospheric pressure and 790 °C in a flow system in a vertical quartz tube reactor. In general, MgO/NiO catalysts had high conversion rates of both $CH_4$ and $CO_2$, with values between 60-75% and 80-95%, respectively. In addition to maintaining activity, catalysts improved conversion slowly. CO yield percentages fluctuated between 70-85%.

### 2.8.2 Use of gels in catalyst synthesis

The use of gels is somewhat common during synthesis of catalysts for DRM. Briefly, aerogels are obtained when the liquid phase of a gel is replaced by a gas. In this way, the solid network within the gel is preserved, and shrinking is not highly visible in this type of product. The liquid within the network may be alcohol (alcogel) or water-based (hydrogel). Lastly, xerogels are obtained when the liquid phase of a gel is eliminated by evaporation. Even though it can retain its original shape, shrinking is highly likely and thus prone to cracking when drying, although some techniques have been developed to prevent formation of cracks [83]. The information provided in this paragraph contributes to explaining the results contained in this section.

Jiang *et al.*, compared in 2013 the differences between the effectiveness of an aerogel support and a xerogel, using Ni as a catalyst on $Al_2O_3$ support [84]. In the case of the aerogel, the conversions of $CH_4$ and $CO_2$ had only a slight decrease over a 30-hour period and remained always above 90%. In contrast, the effectiveness of the xerogel remained in constant decline, starting at about 90% and reaching 50% after 30 hours. The difference in conversions and yields is explained by the form of preparation, since the conversion of a hydrogel to aerogel allows a more uniform distribution of catalytic particles, while the xerogel allows a diffusion mechanism, losing quality by shrinking drastically. Effectiveness in initial conversion can be explained by a temperature programmed reduction (TPR) analysis, where the maximum consumption of $H_2$ occurs for the aerogel catalyst occurs at 730 °C. The loss of xerogel activity is based on high particle density of nickel, as well as the larger size of the formed crystals.

Xu *et al*. (2003), prepared $ZrO_2$ supports from zirconyl chloride and used 11-13% Ni as the active phase. This precursor was first converted to zirconyl hydroxide, which was later transformed into hydrogel and alcogel [85]. Nanocrystals were prepared under different conditions: calcinate from hydrogel and alcogel, dried with $N_2$ from hydrogel and alcogel, dried with $N_2$ from alcogel after digestion in ethanol. Finally, the alcogel was subjected to supercritical drying. Catalysts were prepared via impregnation, and the mixture improved its dispersion by rotary evaporation.

The catalytic reaction was conducted at 757 °C in a U-bed fixed-bed quartz reactor. $CO_2$ and $CH_4$ were fed at a molar ratio of 1:1. The reduction of the catalyst was carried out with a flow of 10% $H_2$. The catalysts prepared on hydrogel had conversions close to 90% but were deactivated before 50 h reaction. The alcogels that were dried with $N_2$ and supercritical ethanol maintained higher conversions of $CO_2$ and $CH_4$. The catalyst dried with supercritical ethanol remained at 85% conversion even after 250 h reaction. In separate tests, they reported the stability of supported catalysts prepared by drying with $N_2$ and digestion in ethanol. For the digested mixture in ethanol, the conversion rates were approximately 85% for a period of 1200 h.

In 2013, Arbag *et al*., studied the effect of two main pathways of alumina preparation. The first preparation route was in a sun-gel medium, while the second followed a hydrothermal pathway [86]. The variables used in sol-gel were impregnated with Ni, Mg and Ni, and W and Ni. For the hydrothermal pathway, alumina was impregnated with Ni, and Ni using one-pot procedure, where catalyst preparation changed order. $HNO_3$ was used in both processes of alumina catalyst preparation. The final content of the catalyst (except in pure alumina measurements) was always 16%. The reaction time was 4 hours.

DRM was carried out in a tubular quartz-based flow reactor with internal diameter of 6mm, which was fed with $CH_4$, $CO_2$ and Ar in equal parts. Prior to activity testing, catalysts were reduced under $H_2$ flow. $CO_2$ conversion rates were generally higher than $CH_4$. Regardless of the catalyst type, $CO_2$ conversions remained between 40% and 50%.

### 2.8.3 Use of metallic carbides

Before proceeding with the examination of previous findings, it is necessary to clarify that the use of metal carbides in dry reform requires in addition to certain important factors to prevent oxidation of metal carbide. Some of those factors involve high temperatures. The use of metal carbides and a ratio called stability ratio $R_S$, is expressed in equation 1. A ratio greater than 0.8 has an effect that prevents oxidation.

$$R_s = \frac{P_{H_2} + P_{CO}}{P_{CO_2} + P_{H_2O}} \qquad \text{(Eq. 1)}$$

where P refers to the partial pressure of each compound indicated.

However, it can then be observed that the experiments analyzed here resort to high pressures, even though dry reforming is generally carried out at atmospheric pressure.

Lamont and Thomson studied in 2004 the importance of the factors mentioned above, regarding the stability of $Mo_2C$. They proposed that any increase in the rate of molar flow of the system, as well as any pressure decrement in the system, resulted in oxidation of carbides. Specifically, they sought a relationship between partial pressures and mass transfer [87].

First, they mentioned that despite the protective effect of $CH_4$ against oxidation of carbides, this gas does cannot prevent the disappearance of carbide. Therefore, it is not included in the calculations of the stability quotient.

Due to large changes in $Mo_2C$ content (between 3 and 45%), they were able to keep the molar flow independent of the GHSV. Two of the experiments will be mentioned briefly, which are closely related.

1. An increase in molar feed velocity was found to produce a less stable active phase of the catalyst. To avoid this effect, temperature needed to increase (if molar flow was to be kept at higher levels).
2. It was found that a reduction in experimental pressure also results in a need to increase the temperature of the system.

In the first case, they worked with 4 variations in GHSV (between 3,000 and 30,000). For each GHSV, molar feed velocities between 0.1 and 0.6 mol $cm^{-2}$ $h^{-1}$ were used. In 3 of the 4 cases, an increase in molar flow rate resulted in a need to increase the temperature of the reaction system to avoid losing the carburized phase. For a GHSV value of 3,000, no temperature increase had an influence on catalyst preservation. Similarly, in the second case it was discovered that a carburized catalyst can be preserved if pressure descends to atmospheric levels, as long as the temperature rises above 900 °C. On this basis they conclude that it is necessary to protect the surface of the reaction bed from conditions that may lead to oxidation of the carbide. These experiments showed that it is possible to strike a balance between reaction kinetics and mass transfer. These findings help explain why Brungs *et al*. increased pressure in the system to 8 bar in the two studies reported here (see below in this same section).

Finally, a further part of this research will be briefly discussed, where Lamont and Thomson worked with pure $Mo_2C$, and found that as the temperature increased, oxide began to turn into carbide. When it reached 850 °C, the sample was carburized and became an active catalyst. This concludes importantly that lower temperatures favor oxidation and high carburization.

In support of equation 1, Darujati and Thomson (2005), made modifications to the stability quotient, also working with $Mo_2C$. They compared the effect that this ratio ($R_s$ = 0, 1.5, 3.0) has on DRM. The change of $R_s$ ratio was achieved by the initial addition of CO to the system [88]. In addition to this, other variations were handled, which are explained below.

The modification of this ratio by addition of CO can also be related to a principle by Le Chatelier, which states that any modification to equilibrium will be counteracted, with a possible change in direction. This helps to correlate a protective effect by CO and the need for mass transfer phenomena to preserve carbides during DRM. The experiments carried out in that study are described below.

a) $Mo_2C$ was supported on alumina, MgO and $ZrO_2$, but left unpromoted.
b) The impregnation order of the promoter and catalyst was changed. Due to the great effect that the addition of CO had on $CH_4$ conversions, the analysis of the article will be limited only to research with variations in the stability quotient. The researchers conducted a study of 27 hours.

For its part, the 27 h study with CO in the initial feed was much larger, as it also applied an intermediate $R_s$ with a value of 1.5, in addition to the values of 0 and 3. The initial

conversion values of $CH_4$ were 97%, and after 27 hours of reaction the catalysts with values of 1.5 and 3 were the most stable, while those with values of 0 were quickly deactivated. Slow deactivation of catalysts kept conversion values above 90%.

In 1999, Brungs *et al*. experimented with different types of metal carbides as a catalyst in dry reforming [89]. Their article published focused on transition metal carbides from groups V and VI. They found that the use of Mo and W carbides were more effective than the Nb, V and Ta carbides. The temperature used for most tests was 950 °C. The measurements reported for these three parameters start close to 87%, decrease to 82% and after 4 days of reaction reach a maximum limit of 90%, remaining at that percentage until the fifth day. This period is undoubtedly one of the longest reported in terms of catalyst stability, only lower than studies conducted by Xu *et al*. (2003) and Shamsi *et al*. (2006), where the respective reaction times were 50 and 15 days, respectively [85, 80].

The diffractometric analysis between the samples (pre and post-catalysis) reveals that there were no major differences in Mo carbide, thus revealing the high resistance of this catalyst. Even after such an extended period, no significant differences were revealed for the active phase.

A year later, Brungs *et al*. (2000) reported an experiment in which only Mo carbide was used [90]. The explored variables consisted of exploring their effectiveness for DRM using the variables mentioned below.

1. A lower amount of $Mo_2C$ within the support (3.8%).
2. A comparison between calcination times (4 and 24 h). $Mo_2C$ was dispersed in $SiO_2$, alumina, $ZrO_2$ and $TiO_2$, respectively.

A solution of ammonium heptamolybdate was prepared, which was mixed with $Al_2O_3$, $SiO_2$, $TiO_2$ and $ZrO_2$. After 12 h drying, the mixture was calcined at 450 °C for 4 h or 24 h. After calcination of the mixtures, the carbide was formed by a temperature-programmed reaction with ethane and $H_2$. The use of this mixture reduced carburization temperatures (630 °C). DRM was carried out at 950 °C, and 8 bar pressure for 38 h. The effectiveness of the catalyst with $TiO_2$ was extremely low. Conversion rates ($CO_2$ and $CH_4$) were initially higher for $SiO_2$ than alumina (close to 100%) and the $ZrO_2$, but lost activity after a few hours of reaction. In the end, the conversions over alumina and $SiO_2$ were very similar (between 80% and 90%). Meanwhile, the $ZrO_2$ started with 90% conversions, and maintained a very subtle reduction up to 8 hours of reaction, deactivating faster after 10 hours. Catalyst mixtures with 3.8% $Mo_2C$ were quickly deactivated after only 6 hours of reaction.

Finally, the comparison between calcination times revealed that the stability of a mixture calcined by 4 h is of high stability (35 h), whereas 24 h of calcination led to rapid deactivation.

To conclude, Hirose *et al*. (2011) managed to synthesize a bimetallic carbide with Mo and Ni at 510 °C. No $MoO_2$ or mono-metallic carbide were found after the carburization process, according to the diffractometric analysis [91]. When other carburization temperatures were used, it was seen that $MoO_2$ did not carburize fully. The catalysts had a nickel content between 25 and 75%, the rest of the material being Molybdenum. Conversion values of $CH_4$ and the formation of $H_2$ in mmol/min show great loss of activity within a few minutes of testing. However, they manage to stabilize and regain some activity after a few hours. This recovery has an explanation similar to that offered by Lamont and Thomson

(previously analyzed), whereby increasing reaction temperatures, the fractions of $MoO_2$ begin to form carbides, so activity is somewhat increased.

## 2.9 Cutting-edge Techniques

Before describing the most recent treatments, the use of alloys or amalgamated metals will be briefly discussed. Alloys are effective methods for increasing catalytic properties in materials, thanks to synergistic effects. Nickel can be reinforced with other metals to create nanoalloys. One of the benefits of catalysis is increased resistance to sintering. The addition of small amounts of noble metals further increases the oxidation resistance of nickel particles. However, lower-than-expected yields are presented, as the effectiveness of an alloy depends on the shape, crystal structure and particle size [92]. An alloy that does not meet these characteristics will probably lack the proper physicochemical properties to improve a catalytic mixture. Therefore, it is necessary to resort to other strategies, which revolve around the synthesis of highly resistant supports. Some structures are core-shell, core-sheath, and lamellar. The insertion of active phase into mesopores is a recent trend as well.

One of the recent treatments that have been studied aims to incorporate particles into the pores of a support by using third-party agents in mesoporous $SiO_2$ supports. The other major variations in recent years is the design of core-shell and yolk-shell systems for silica supports.

SBA-15 has been used very frequently for DRM. A solution of $Ni(NO_3)_2 \cdot 6H_2O$ with polyethylene glycol, glycerol and ethanol has previously been added to this silica [93]. Ethanol was not a major contributor towards introducing the nickel precursor particles into

the silica's mesopores, but glycerol and ethylene glycol did achieve the intended goal. On the downside, the viscosity and high boiling point of glycerol make it difficult to use in materials science. The use of polyethylene glycol managed to insert the precursor particles of nickel into mesoporous channels. When comparing this catalyst to one prepared by the traditional incipient wetness methods, catalysts using polyethylene glycol will be less active. Regarding terms of carbon deposits, these were harder to detect. In a similar study, polyethylenimine (PEI) was used in a solution of $Ni(NO_3)_2 \bullet 6H_2O$, which were mixed in with SBA-15. Some of these syntheses also use mesitylene (used to expand pores), and their effectiveness was compared to a negative control that used neither PEI nor mesitylene. PEI was successful in drawing the nickel precursor into the mesopores thanks to interactions with silanol groups in SBA-15 channels. Thanks to this insertion, this technique helps to avoid sintering phenomena, as well as formation of carbon deposits. Catalysts used as negative control tended to deactivate faster, whereas in the other samples conversion of reactants remained around 85%, with little loss of activity over a 40-hour period [94].

The use of spheric silica along with oleylamine, oleic acid and nickel has been reported for DRM. The conversion of reactants in this case was approximately 70%. However, these values can be increased by adding $La_2O_3$ to nickel and silica systems, which also are an obstacle for carbon deposits. The stability of these catalysts can be explained by the presence of amines, which then turn into amides [95]. Annex A is a study describing the how the use of alkaline materials is crucial in improving both $CO_2$ conversions and eliminating carbon deposits.

A separate study synthesized mesoporous and spherical silica in alkaline conditions and introduced cetrimonium bromide (CTAB) and dodecanol into the synthetic pathway.

Dodecanol was the template used for the creation of mesopores. Upon creating spherical $SiO_2$, nickel nitrate was finally added [96]. Catalytic studies reveal that upon adding more dodecanol during synthesis, better reactant conversions are to be expected. However, they do not mention at which level of dodecanol addition there is a reduction in activity. These references do not explain if their spherical silica is SBA-15.

Another modern trend consists in using core-shell or yok-shell structures for DRM. Nickel phyllosilicates are laminar silicate structures that are gaining importance in synthesis of material. Phyllosilicates consist of SiO4 tetrahedron sheets, with a central silicon molecule at the center of the basic structure. Upper vertices will then coordinate with metal oxide octahedrons, which are usually Mg or Al. Layers of tetrahedrons and octahedrons are set up as sheets, giving rise to phyllosilicates [97]. Nickel phyllosilicates are structures that allow the active phase to disperse finely over $SiO_2$ by heat treatment. Some studies have achieved good catalytic activity in DRM with temperatures as low as 600 °C, showing little carbon formation thanks to the addition of a $CeO_2$ nucleus [98, 99]. The use of $CeO_2$ has been described as an enhancer of redox potential and oxygen storage. Now, a core-shell structure can convert into a yolk-shell structure if proper time and pH of hydrothermal treatment are provided. Using nickel acetylacetonate as an active phase precursor for nickel phyllosilicates can result in increasing specific areas and decreasing carbon deposits [100]. Carbon deposits that form cannot easily increase in quantity, as nickel particles are tightly confined within the structures. Figure 9 shows a synthesis process going from silica to nickel over a nickel phyllosilicate (forming a hollow sphere) with $CeO_2$ over the shell structure.

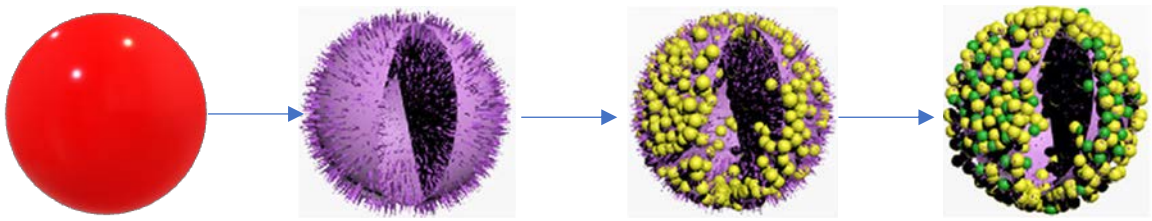

**Figure 9.** Process that shows formation of nickel phyllosilicates in the shape of a hollow sphere and with $CeO_2$ particles over the shell structure. Taken from [99].

The combined use of nickel and magnesium phylosilicates has been reported, giving rise to stable, alkaline catalysts [101]. The combined catalysts have allowed DRM to continue for 48 hours, with little loss of activity (about 80% of conversions for both). Figure 10 depicts how nickel phylosillicate hollow spheres have a greater tendency towards eliminating carbon deposits. Finally, a stable structure with a novel satellite system has been used for DRM. The formation of this material is depicted in figure 11, whereby a nickel core is obtained first, after which a silica shell and surfactants are added, resulting in the formation of nickel "satellites". TEM micrograhps are shown in parellel to sketches. Using this system has resulted in conversions over 90% at 800 °C [102].

Finally, an effective but little-published method has been used for DRM, which basically consists of applying an $H_2$ pretreatment to finished catalysts prior to reforming. After wetness impregnation, the dry catalyst is subjected to a hydrogen flow at 400 °C, and a calcination at 700 °C. The role played by the hydrogen flow consists in eliminating oxygen radical presence while increasing dispersion of nickel particles. In fact, this dispersion has been so great, that nickel was not detectable by XRD [103]. Also, by eliminating oxygen molecules, sintering was avoided. After calcination, interactions between active phase and support are augmented. Materials treated solely with hydrogen or air resulted in unproper

materials for DRM. There are a few reports that have also used hydrogen treatment prior to calcination [104, 105].

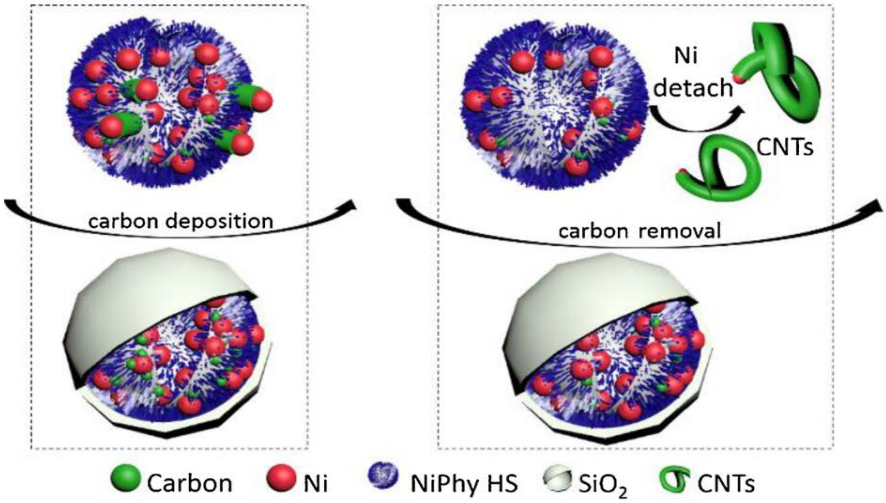


**Figure 10.** Elimination of carbon deposits by nickel phyllosilicates. Taken from [101].

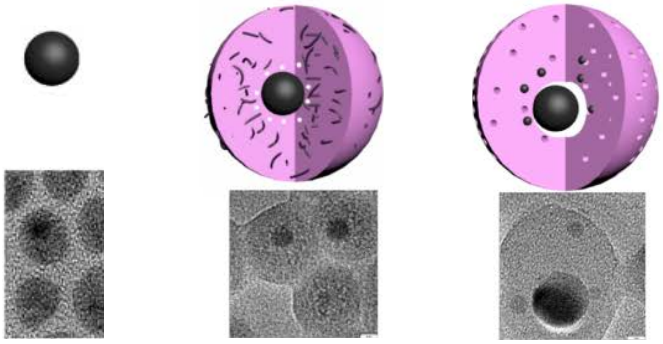

**Figure 11.** A scheme showing the evolution form nickel particle to nickel-yolk systems with nickel satellites. Taken from [106].

### 2.9.1 Use of simulation for DRM applications

Navas-Anguita *et al*. (2019) made a significant contribution regarding the feasibility of converting biogas to liquid fuels, with DRM as an intermediate step [107]. This was carried out with help of Life Cycle Assessment methodologies, which was used to compare two types of diesel. One diesel was obtained by conventional refining, and the other via FT synthesis with syngas derived from DRM. Life Cycle Assessment is a well-established methodology that allows potential impacts and environmental aspects to be evaluated upon implementation of a process. To carry out this assessment, a series of input and output inventories is inserted into specialized software. The parameters and databases that were introduced into this methodology were global warming potential, cumulative non-renewable demand, ozone layer depletion, acidification and eutrophication. Energetic analyses were carried out on Aspen Plus, going from biogas to Fischer-Tropsch reaction. Upon completion of analysis, conventional fossil diesel was superior in 3 of the parameters, which were global warming potential, acidification and eutrophication. This means that by using currently available DRM and Fischer-Tropsch technology, diesel produced via catalytic reactions will surpass conventional fuel in only in cumulative non-renewable energy demand and ozone layer depletion. According to this document, much still needs to be researched to assure superiority of catalytic processes over conventional fuel sources. The Sunexus solar project mentioned earlier for DRM could improve many of these parameters.

## 2.10 Hypothesis and Objectives

### Hypothesis

It is possible to synthesize nanostructured nickel-based catalysts with alkaline and mesoporous properties that allow DRM at reaction temperatures below 800 °C in order to obtain syngas at a molar ratio of 1, and that also allow the reaction to continue properly without deactivation for extended periods of time.

### Overall goal

To design new and efficient nickel-based catalysts by combining alkaline and textural properties, which allow dry reforming of methane to occur below 800 °C over extended periods without losing activity and without coking problems.

#### Specific goals

1. To create multiple catalysts that combine properties of alkalinity and porosity that allow DRM to be carried out.
2. To compare the properties of materials via advanced characterization methods, which allow the comprehension of deactivation mechanisms in the synthesized catalysts.
3. To study coke formations over spent catalysts in order to determine carbon elimination strategies.

# Chapter 3:
# Materials and Methods

## 3.1 Materials Synthesis

### 3.1.1 Silica

The mesoporous silica that is essential to this thesis was named Cach, after the Universidad de Ciencias y Artes de Chiapas (UNICACH). Even though Cach is synthesized in similar manner to that of SBA-15, these materials are very different. Cach is essentially a disordered mesoporous silica, which does not diffract at low angles by use of SAXS and lacks a hysteresis loop pertaining to ordered mesoporous materials. Cach was prepared in a similar way as has been described for SBA-15 [108]. In short, 3 g of Pluronic P123 (Sigma-Aldrich) were dissolved in 78 ml of distilled water and 15 ml of concentrated HCl (Fermont, Mexico). Once Pluronic P123 was dissolved, 6.4 TEOS (tetraethylortosilicate, the silicon source) were added by slow dripping to avoid the formation of agglomerates. Once TEOS was added, 3 g of mesitylene (1,3,5 trimethylbenzene, Sigma-Aldrich) were introduced to the mixture. The final mixture was kept at 35 °C for 24 h. The sediment was separated by filtration and washed 5 times with distilled water. The sample was dried at room temperature and subjected to 100 °C for 24 h. Finally, the product was calcined at 500 °C by 6 h to remove Pluronic P123 from the mixture. A very important precaution in this synthesis is that drying, and calcination should be done under the flow of the extraction hood, as mesitylene releases very potent odors during these stages. If this calcination is not performed in an extraction hood, the stench remains for days. This serves as a reminder that finding a substitute for mesitylene could improve the process. A condensed depiction of Cach synthesis is shown in figure 12. This material appears as “Cach” when used in nomenclature of catalyst names. For more information concerning Cach, see Annex C.

The commercial silica used in this thesis (Ald) is a nanoparticulate material and was acquired from Sigma-Aldrich. Its reported particle size was between 10 and 20 nm.

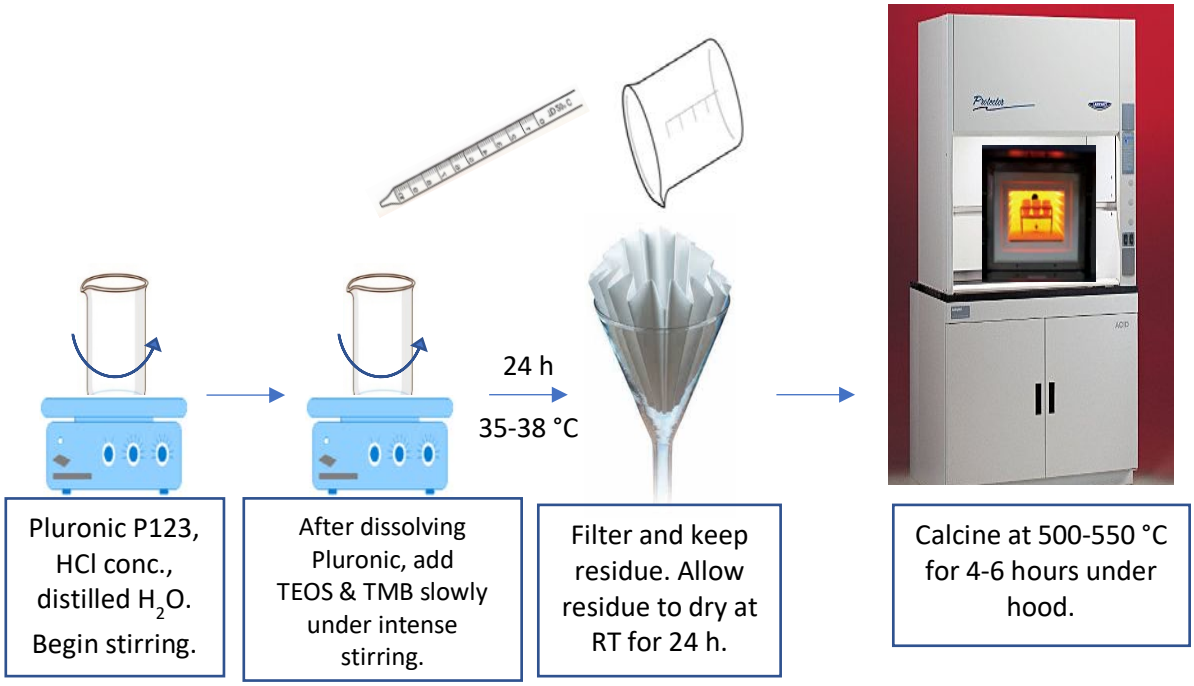


**Figure 12.** A depiction showing the Cach synthesis process, including the important step of calcination under the hood to avoid harmful fumes.

On the other hand, SBA-15 synthesis was performed in the traditional way. First, 3 g of Pluronic P123 were dissolved in a mixture of distilled water and hydrochloric acid (as indicated above for the Cach material). Following the dissolution of Pluronic P123, 6.4 g of TEOS were added very slowly. After being left in agitation for a period of between 2 and 4 hours at room temperature, the solution was transferred to a bottle with a Teflon cap. The bottle was kept between 48 and 72 h at 95 °C. Once this time was completed, the SBA-15 samples were left to dry at room temperature. The calcination was carried out at 500 °C. It is possible to see that the biggest difference between Cach and SBA-15 materials is the use of mesitylene, as well as the use of higher temperatures. The SBA-15 material was designated

as SBA when used in nomenclature. SBA-15 was used only in the evaluation of carbon formations for comparison purposes between mesoporous materials (chapter 6).

### 3.1.2 Other supports

The alkaline supports used in this work were ZnO, MgO and nanoparticulate ZnO. The precursors for ZnO and MgO were Zinc and Magnesium hexahydrated nitrates (Fermont, Mexico), respectively. Nanoparticulate ZnO was purchased from Sigma Aldrich.

Finally, even though the use of carbon appeared as a side effect of a carburization process, it enabled catalysts to endure the harsh conditions of DRM. A catalyst name including a C at the end of the nomenclature indicates that the material was subjected to carburization.

### 3.1.3 Active phases

The active phases in this study were nickel, platinum and molybdenum. As can be expected during calcination processes, there were occasions where new compounds formed. Some of these were formed via reactions with ZnO, which was initially only meant as a support. The precursors for NiO, Pt and $MoO_3$ were $Ni(NO_3)_2*6H_2O$ (Fermont, Mexico), $Pt(acac)_2$ (97% purity, Sigma Aldrich) and ammonium heptamolybdate tetrahydrate (Sigma Aldrich), respectively.

## 3.2 Wet impregnation and carburization

The addition of the precursor of the active phase (NiO, $MoO_3$) or secondary supports (MgO and ZnO) was carried out by the incipient wetness impregnation method [109, 110]. A solution containing the proper amount of the desired metal was prepared and then added to the dry supports. For each case, the formed mixture was left drying for 12 h at 65 °C, then calcined at 400 (calcination of precursors of MgO and ZnO) or 500 °C. was dissolved in

dichloromethane and added directly to the materials, as needed. The precursor of Pt was maintained as such until the reduction stage during the reaction of the formation.

Finally, the carburized samples (Ni-Cach-C, Ni-MgOAld-C, Ni-ZnOAld-C and NiMo-$Z_{np}$-C) were prepared with160 mg of the calcined mixture, which were placed on a bed of quartz wool inside a stainless steel reactor (DI 9 mm) created at UNICACH. The reactor was preheated with a flow of 50 ml $min^{-1}$ Ar (Praxair) to 500 $^{o}$C. Subsequently, a flow of $CH_4$ (Praxair 20% v/v) was introduced, and the total flow was adjusted to 150 ml $min^{-1}$ until reaching 700 $^{o}$C.

Finally, $CH_4$ and the heating were switched off, and the Ar flow was adjusted to 50 ml $min^{-1}$ for the cooling stage. The synthesis of carbides was made in the reaction system "CACH", shown in Figure 13.

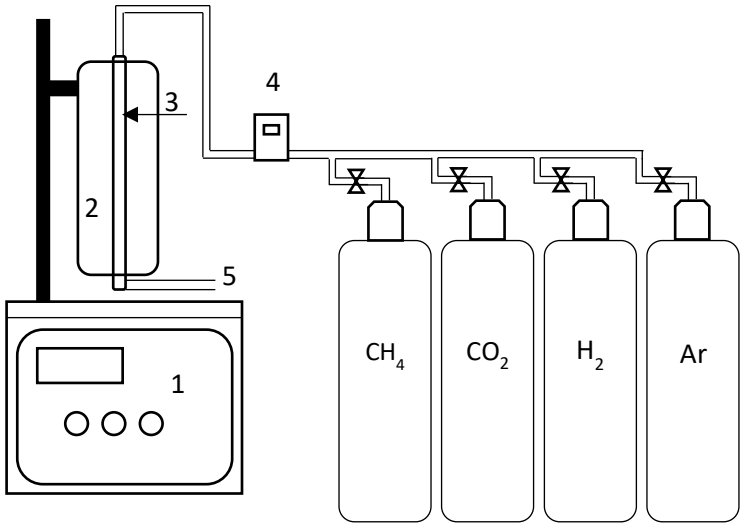


**Figure 13.** Reaction system used for carbide synthesis.

1) Time and temperature control, 2) Muffle Furnace, 3) Detachable Reactor, 4) Aalborg Flowmeter, 5) Gas Exit from system

## 3.3 Nomenclature of catalysts

Table 1 shows the active phases and supports to be used throughout the thesis.

**Table 1.** Codes assigned to each material used in this section. Active phase, support and carburization rows also indicate the order in which the codes appear in a catalyst name.

| Element/compound | Abreviation | Active phase | Support | Carburized |
|---|---|---|---|---|
| Nickel | Ni | X | | |
| Platinum | Pt | X | | |
| Molybdene | Mo | X | | |
| $SiO_2$ commercial | Ald | | X | |
| $SiO_2$ Cach | Cach | | X | |
| $SiO_2$ SBA-15 | SBA | | X | |
| Zinc Oxide | ZnO | | X | |
| Magnesium Oxide | MgO | | X | |
| Zinc oxide n.p. ** | $Z_{np}$ | | X | |
| Carbon | - C | | | X |

** n.p. nanoparticulate ZnO (Sigma Aldrich).

To easily interpret the nomenclature, the order mentioned below was used throughout the dissertation. The active phases were assigned to the beginning of the catalyst code. The supports were placed after the first hyphen. If the material was subjected to a carburization process, a C was attached after a second hyphen.

For example, NiPt-MgOCach material will have nickel and platinum as active phases, and a mixture of MgO and $SiO_2$-Cach as supports.

## 3.4 Characterization of Materials

Characterization of catalysts is provided in this section, along with complementary information of each method.

### 3.4.1 Extended description of characterizations

#### *3.4.2.1 WDXRF*

The chemical composition of materials was determined by wave dispersion X-ray fluorescence (WDXRF), on a Rigaku Supermini 200 unit with Pd anode (200 W of power), coupled with an RX25 and LiF crystals (200) and a Zr filter and a P-10 gas flow. Basically, an electron can be pushed from its atomic orbital by absorbing a wave of light or photon with enough energy. The energy of the photon must be greater than the energy with which the electron is attached to the nucleus of the atom. When an electron of internal orbitals is expelled from an atom, an electron of a higher energy orbital will be transferred to a lower energy level (from where the electron was expelled in the first place). This is a transition that can emit energy from the atom. This emitted energy constitutes the phenomenon of fluorescence and is known as an X-ray characteristic of an element. The energy of an emitted photon is equal to the energy difference between the orbitals occupied by the electron that is undergoing the transition. Since there is a constant energy difference between orbitals, the emitted photon will always have the same energy. If the wavelength of the emitted energy is determined, it is possible to identify the identity of each element. However, there are secondary fluorescence phenomena that can lead to inaccurate results.

*3.4.2.2 XRD*

Quantitative phase identification and analyses were carried out with X-ray diffraction (XRD). The diffraction patterns were captured with a Rigaku Ultima IV equipment (Rigaku, Japan) configured with Bragg-Bentano geometry, using a copper anode (K-alpha-1.5418). Measurements were made between 2θ angles of 15 ° and 100 °, with a step size of 0.02 ° and a rate of 1-degree $min^{-1}$.

X-ray diffraction is one of the most important and rapid material analysis techniques for characterizing crystalline materials. They are mainly used to identify phases of a crystalline material that can provide information on the dimensions of unit cells, and interatomic spaces.

Typically reported measurements are performed by a scan that starts with 2 degrees θ from low to higher angles. The reported angles are usually between 10 and 90 °. Diffracted radiation is captured by a mobile detector that can always collect diffracted rays. In this way, the diffractogram provides information on crystalline planes that diffraction depending on the angle 2θ. In general, diffraction will only be available when the Bragg equation (Equation 6) is complied with, although angles that differ slightly may cause the diffraction phenomenon. This equation indicates the relationship between the crystalline spacing $d_{hkl}$, the wavelength used, and the angle of the diffracted X-ray beam.

$$n\lambda = 2d_{hkl}\text{sen}\theta \qquad \text{(Eq. 2)}$$

In equation 2, $2d_{hkl}$ is the final summation required for the equation, and is derived from two interplanar spaces $d_{hkl}$. The term "n" is a multiple of (λ). These experiments were performed on a Rigaku Ultima IV X-ray diffractometer.

Another equation used widely is the Scherrer equation, as it allows the particle size to be calculated from X-ray diffraction data. The equation establishes the relationship between the average wavelength of applied X-rays and the FWHM of the diffraction peaks.

$$t = \frac{0.9\,\lambda}{B cos\theta} \qquad \text{(Eq. 3)}$$

In equation 3, t is the particle size, λ the average wavelength given in Å, B is the FWHM value, and the angle at which the diffraction peaks appear. However, all values provided in this work are in nm. It should be noted that only θ is used and not the 2θ value that appearing in the diffractogram. FWHM calculations can be done visually on the screen of crystallographic software, but it is more accurate to use specialized software with regression calculations. For this purpose, FullProfSuite was downloaded, which includes the WinPLOTR software that allows an accurate FWHM measurement to be found. FullProfSuite is a product of Institut Laue-Langevin (Grenoble, France).

*3.4.2.3 $N_2$ Physisorption*

Specific surface area was determined by $N_2$ physisorption (BET areas). The experiments were conducted with a Bel Japan Belsorp Max at -196 $^oC$, but samples (approximately 60 mg) were degassed prior to testing for 16 h at 150 $^oC$ on a Bel Japan Bel Prep II instrument.

The relationship between adsorbed molecules and pressure can be visualized over an adsorption isotherm. When the adsorption paths do not match the desorption paths, it is called hysteresis. An isotherm of this type allows you to calculate the surface area of a solid, pore size, and distribution.

Before carrying out any measurement, the samples of supported catalysts must be degassed. This eliminates adsorbed gases and water, the presence of which yields uncertain surface area results. The maximum possible temperature is chosen in such a way that it does not damage the structure of the sample, and should be used to shorten the degassing time, which is optimally 16 hours. This time ensures that unwanted vapors and gases are removed from the surface of the catalyst. An estimated 60 mg of sample is used for this test. For both degassing and measuring, catalytic mixtures must be placed in glass bulbs (elongated holders). To degas, they are placed in a BelSorp equipment. Subsequently, the sample holder is introduced in a container with $N_2$, so that the mixture is kept at temperatures of liquid $N_2$ (-196 °C). In this way, the interaction between gas molecules and the sample surface will be large enough for an adsorption capable of being recorded. Gas $N_2$ (adsorbate) is injected into the cell by a calibrated piston.

The surface area is obtained by adjusting the information obtained from bet isotherms with a $P/P_0$ range of 0.05 to 0.33, using consumption of $N_2$. This range is used because it is

the only region in which the chart is linear. The pore volume is reported at a $P/P_0$ close to 1. The BJH method was used to determine the average pore size.

#### *3.4.2.4 H2-TPR*

The temperature programmed reduction with $H_2$ ($H_2$-TPR) of the catalysts was carried out with a Bel Japan Belcat-B. The samples were pre-treated at 250 °C for 3 h to remove organic particles (in the case of $Pt(acac)_2$ samples). The reducing gas contained 5% $H_2$ (balanced with Ar) at a flow of 50 ml $min^{-1}$ and a heating speed of 10 $^oC$ $min^{-1}$. After reaching 900 $^oC$, the samples were kept for 5 min at this temperature before cooling began. $H_2$-TPR is one of the most valuable thermal methods available for the study of catalysts [111]. This method is based on the consumption of $H_2$, which is directly related to the reduction of oxidized components in the samples. This type of analysis allows to obtain information about the number and type of reducible components present in a catalyst, its reduction temperature, and even on the interactions between the support and the active phase.

A common procedure involves reducing approximately 0.15 g of catalyst in a flow of 60 ml/min to 20 °C at atmospheric pressure. The flow consists of 5-10% $H_2$ in $N_2$ or argon. The temperature starts to rise linearly from 100 to 1000 °C, with increments of 10 °C per minute. $H_2$ consumption is measured by a thermal conductivity detector (TCD), using a pure $N_2$ or Ar flow for reference. The result of the interaction between $H_2$ and $O_2$, as well as the decomposition of precursors is the formation of water, which must be trapped using molecular sieves. This prevents interference in the measured signal. The TCD is calibrated by this same method and with the reduction of pure metal oxides.

The measuring device was a BelCat equipment, equipped with a TCD and connected to a data station.

#### *3.4.2.5 Raman Spectroscopy*

Raman spectra were collected with a Raman Renishaw inVia (Renishaw, UK) microscope equipped with a 532 nm green laser, using only 10% of the total laser power to prevent damage to the sample. Additionally, Raman spectra were collected for spent samples.

Raman spectroscopy is a technique based on an inelastic scattering process, which is induced by monochromatic light, which is usually a laser [112]. The photons of this laser light are absorbed by matter and then remitted. After interaction with matter, the frequency of remitted photons may increase or decrease from that of monochromatic light. This frequency change provides information about rotational and vibrational transitions in molecules. Approximately 99.99% of photons go through an elastic vibration or dispersion process. That is, there are very few molecules in a material that will produce a Raman effect.

A sample is usually exposed to a light source, which can be UV, visible or IR. The dispersed light is then collected through a lens, after which an interference filter is used to obtain the Raman spectra.

#### *3.4.2.6 Scanning Electron Microscopy (SEM)*

Scanning electron microscopy is a technique used to analyze the morphology of solid materials of all kinds, such as metals, polymers and biological samples. The technique involves influencing a beam of electrons on a sample, resulting in the appearance of different signals. With the signal of secondary electrons, an image of the surface morphology of the sample is obtained. The scatter signal generates a qualitative image of areas with different

mean atomic number, and the X-ray signal (if used) provides spectra and images about the composition of chemical elements in the sample.

#### *3.4.2.7 High Resolution Transmission Electron Microscopy (HR-TEM)*

TEM is a technique that allows high-resolution atomic scale images of crystallographic structures to be obtained. Like SEM, a beam of electrons is also used. However, it also consists of focusing the beam using two condensing lenses on a sample. The electrons that manage to pass through the lenses are focused to form the first image, which will also be augmented with projector lenses. The final image is displayed on a fluorescent screen, which can be seen by a digital camera.

## 3.5 Evaluation of catalytic properties

Evaluation of catalytic properties involved multiple activities, which are described below.

### 3.5.1 Determining equilibrium constants

The calculation of equilibrium constants is explained in detail in Appendix 1.

### 3.5.2 GC-Calibration curves

Calibration curves were generated for $H_2$, $CO_2$ and $CH_4$. To generate these curves, gas samples were taken from directly from gas lines and temporarily stored in a Supelco bag. These bags have a cylindrical socket for gas access, which can be sealed when needed by use

of septa, preventing the release of the content. After filling the bag, a known amount of gas was taken, ranging from 0.1 to 1 mL with a special chromatography syringe. This amount is injected into the manual injection port of the gas chromatograph. If there are no leaks in the system, each injection should provide a reproducible area in the chromatogram, although small variations may occur. Thus, peak area should be directly proportional to the injected volume. Linear regression is applied with the injection volumes and corresponding areas, which in turn provides chromatographic constants for each gas. Before applying regression, it is important to force the resulting line to cross the origin coordinates, thus making sure that chromatographic constants are very basic values. Because no high purity CO was available, obtaining a reliable regression line was complicated. Thus, CO was calculated by use of mass balances.

### 3.5.2 Dry Reforming of Methane

The activity and stability of the catalysts was tested on an RXM-100 Advanced Scientific Designs Inc (ASDI) catalyst multifunctional equipment. The experiments were conducted at 700 °C with a power supply of $CH_4/CO_2$ in a ratio of 1:1, with 67% v/v of Ar flow. The total flow was 90 ml $min^{-1}$. The reaction was carried out at 0.76 atm, at atmospheric pressure of Mexico City. In a typical run, 100 mg of catalyst were placed in a bed of quartz wool and inserted into a stainless-steel U-reactor. After a reduction with $H_2$ for 1 h at 580 °C, the flow of $H_2$ was replaced with an Ar flow for 30 min. At the end of this time, the temperature rose to 700 °C, and the flow of $CH_4/CO_2$ was opened, as described above. The temperature was monitored with a thermocouple, which was placed in the catalytic bed. The

output flow was analyzed with a gas chromatograph (HP 6890 equipped with a CarboxenTM 1010 PLOT Supelco column), using a TCD for the detection of reaction products. Initially, a screening phase was carried out to determine which catalysts were most stable, and these tests lasted 4 hours. The long-term tests were done with the best materials and lasted between 35 and 55 hours. This reaction system is shown in Figure 14.

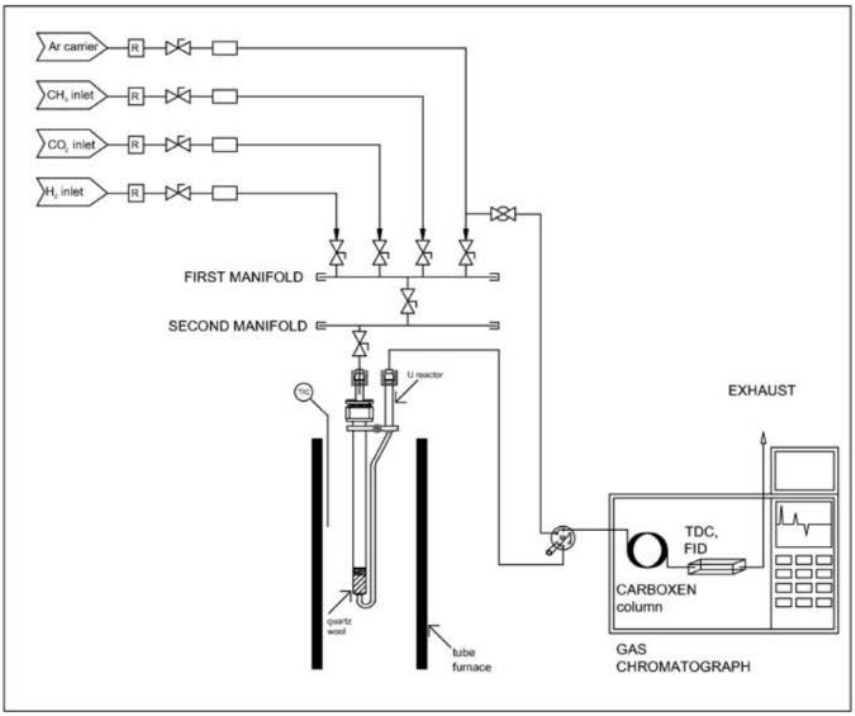


**Figure 14.** Reaction system used for DRM at IPN-Zacatenco. Taken from [71].

### 3.5.3 Carbon formation studies on Ni-silica catalysts

Synthesis of catalysts in this section were identical to what was described above. The reduction and DRM stages were carried out separately. In order to have plenty of material, 130 mg of material were reduced per batch. This was done with a flow of 120 ml/min Argon and 30 ml/min $H_2$ inside the 50 cm piston flow reactor. For the reaction, 50 mg of catalyst were taken, which were placed on a bed of quartz wool inside the reactor. The flow of Ar was maintained at 60 ml/min, and the flows of $CH_4$ and $CO_2$ were 15 ml/h for each. The flows of $CH_4$ and $CO_2$ remained closed until the system temperature reached 700 °C, thus avoiding carbon formations below that temperature. The experiment was held for 5 hours at that temperature. However, it is made clear here that the reaction was stopped once every 60 minutes, thus monitoring the mass increases of the reactor, which would be attributable only to carbon deposits.

In addition to this, characterizations were made on fresh and spent materials. The fresh materials were studied by XRF, $N_2$-Physisorption and $H_2$-TPR. Lastly, the spent materials were studied by monitoring by weight, XRD, Raman spectroscopy, SEM and HR-TEM.

# Chapter 4:
# Nickel and Platinum Catalysts over $SiO_2$, MgO and ZnO

## 4.1 Generalities Pertaining to this Chapter

This section will begin with a few reminders, which are listed below.

a) Most of the focus of this chapter is given to six materials, which were heavily discussed in the article submitted to and published in the International Journal of Hydrogen Energy, titled "**Ni and $Ni_3C$ catalysts supported on mesoporous silica for dry reforming of methane**". Those materials are Ni-Ald, NiPt-Ald, Ni-Cach, NiPt-Cach, NiPt-MgOCach and Ni-Cach-C.

b) The ZnO used in this section was not nanoparticulate, and was added as a solution of $Zn(NO_3)_2*6H_2O$ by incipient wetness impregnation.

c) The results for materials subjected to carburization process (designated by "-C") are presented as non-carburized material for XRF characterization.

d) For these same materials an $H_2$-TPR profile is not presented, as the materials did not consume hydrogen. For other characterizations, the results correspond to the carburized materials.

e) Some of the materials with poor catalytic efficiency may have incomplete characterizations, as those materials with good activity were deemed to be more important.

### 4.1.1 List of catalytic materials

The materials used in this section are condensed in Table 2.

**Table 2.** Catalysts used in this experiment.

| **Catalyst Name** | **Content** |
|---|---|
| Ni-Ald | Ni-$SiO_2$ Aldrich |
| NiPt-Ald | Ni-Pt-$SiO_2$ Aldrich |
| Ni-Cach | Ni-Cach |
| NiPt-Cach | Ni-Pt-Cach |
| NiPt-ZnOCach | Ni-Pt-ZnO-Cach |
| NiPt-MgOCach | Ni-Pt-MgO-Cach |
| Ni-Cach-C | Ni-Cach-C |
| Ni-ZnOAld-C | Ni-ZnO-$SiO_2$ Aldrich-C |
| Ni-MgOCach-C | Ni-MgO-$SiO_2$ Aldrich-C |

## 4.2 Characterization of Materials

### 4.2.1 XRF

The results presented here are grouped according to the type of silica used. Table 3 corresponds to those supported on the Ald material, while Table 4 corresponds to those supported on the Cach material.

**Table 3.** XRF results corresponding to materials with Ald as main support.

| **Ni-Ald** | | **NiPt-Ald** | | **Ni-MgOAld-C** | | **Ni-ZnOAld-C** | |
|---|---|---|---|---|---|---|---|
| Material | % | Material | % | Material | % | Material | % |
| $SiO_2$ | 78.64 | $SiO_2$ | 79.85 | MgO | 16.56 | $SiO_2$ | 50.21 |
| Ni | 21.25 | Ni | 19.42 | $SiO_2$ | 58.4 | Ni | 19.58 |
| | | Pt | 0.73 | Ni | 24.97 | ZnO | 30.07 |

**Table 4.** XRF results corresponding to materials with Cach as the main support.

| **Ni-Cach** | | **NiPt-Cach** | | **NiPt-MgOCach** | | **NiPt-ZnOCach** | | **Ni-Cach-C** | |
|---|---|---|---|---|---|---|---|---|---|
| Material | % | Material | % | Material | % | Material | % | Material | % |
| $SiO_2$ | 74.01 | $SiO_2$ | 79.85 | $SiO_2$ | 54.74 | $SiO_2$ | 47.34 | $SiO_2$ | 77.13 |
| Ni | 25.99 | Ni | 19.42 | MgO | 17.19 | Ni | 19.61 | Ni | 22.87 |
| | | Pt | 0.73 | Ni | 27.06 | ZnO | 31.77 | | |
| | | | | Pt | 1.0 | Pt | 1.28 | | |

The previous tables show nickel percentages in a range between 20% and 25%, while platinum percentages barely exceed 1%. It should be mentioned that the nominal nickel content was estimated at 15%, MgO and ZnO levels were also considered at 15%. However, it should be noted that there are secondary fluorescence phenomena that can substantially modify the values. This phenomenon is discussed in more depth in the next paragraph.

Even though fluorescence can be a very powerful tool, it has a downside that can be easily spotted. Secondary fluorescence emissions can arise when absorption and emission borderline values are extremely close to one another. I.e., if an element emits energy at a value that is too close to another element's absorption value, data provided by the instrument will almost surely be distorted. This is the case for a mixture containing nickel and silicon, for example. A case where such secondary interactions do not exist is that of zinc and nickel. These examples are related to absorption and emission values explained above. In this way, possible errors in stochiometric calculations are excluded.

### 4.2.2 XRD

The results for the XRD patterns are shown in Figure 15. Samples Ni-Ald, NiPt-Ald, Ni-Cach, NiPt-Cach, and NiPt-MgOCach show peaks that correspond to the NiO phase (PDF card: 47-1049), identified as bunsenite (cubic structure with Fm3m space group), with lattice

parameters a=b=c=0.417 nm. Peaks corresponding to platinum could not be observed, due to the small amounts that were added (below 1% m/m), as is evidenced in XRF results. Similar patterns were reported for $SiO_2$/NiO mixtures in other studies, reporting an approximately equal percentage of NiO in the catalyst [113]. As for NiPt-MgOCach, it was not possible to detect peaks corresponding to MgO in the respective diffraction pattern. This is because NiO peaks overlap with MgO peaks, as both have the same space group. Regardless, the MgO phase (PDF card: 43-1022) was identified as periclase. The diffractogram pertaining to Ni-Cach-C showed that the material has two phases. One of them is metallic nickel (PDF card: 4-0850) and graphite (PDF card: 75-1621). Graphite is related to the carburization process and is one of the expected forms of carbon due to cracking of methane. It is important to remember that the values for $SiO_2$ were not considered as part of the quantitative analysis, since the diffraction pattern obtained is amorphous (with maximum height at 22 degrees 2θ).

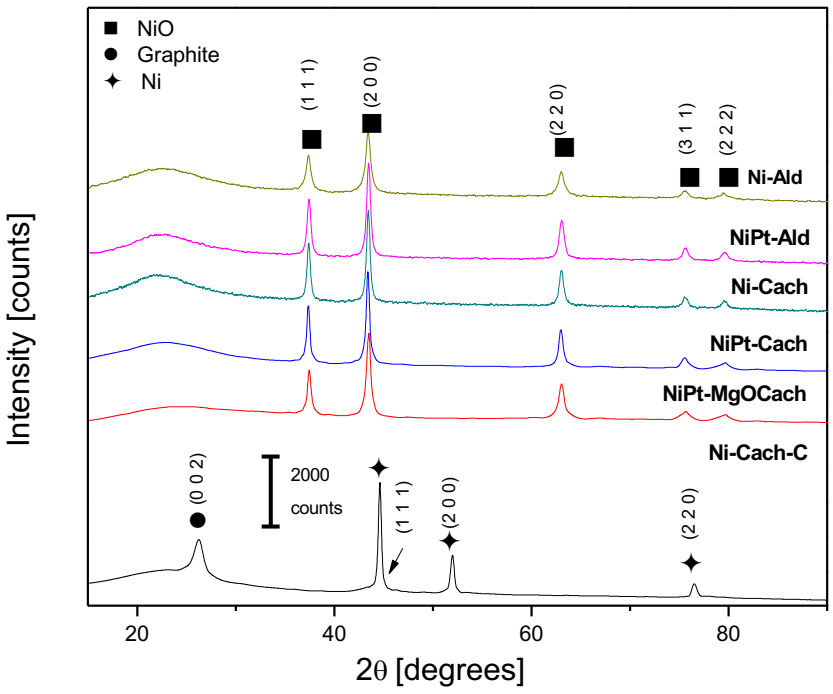


**Figure 15.** Diffraction patterns corresponding to materials used for scientific publication.

Quantitative XRD results for NiPt-MgOCach sample bears a strong resemblance to those obtained by XRF. On the other hand, a crystalline phase corresponding to nickel carbide could not be detected by XRD. The absence of this phase implied several possibilities. For example, it was possible that no nickel carbide was formed, or that if its synthesis was achieved, the particles were so finely dispersed that it could not diffract. Results have been previously disclosed for other metals where the phase is so finely dispersed that it is unable to diffract, due to particle size [114]. Further attempts at identifying nickel carbide were carried out with Raman spectroscopy techniques and high-resolution transmission microscopy.

Table 5 shows the average crystal size for both NiO and metal nickel phase. It also shows the quantitative XRD results, which were made with the relative intensity ratio. This table lists all the materials used in the initial screening. Differences in average crystal size are not necessarily a main factor in the activity a catalyst might have. However, it can make great contributions to catalyst stability, which will be discussed briefly below.

**Table 5.** Quantitative XRD results and cristal size pertaining to largest peak.

| Material | **Mean cristal size (nm)** | **Phases (%m/m)** |
|---|---|---|
| Ni-Ald | 20.8 | NiO (100%) |
| NiPt-Ald | 20.4 | NiO (100%) |
| Ni-Cach | 15.9 | NiO (100%) |
| NiPt-Cach | 22.2 | NiO (100%) |
| NiPt-MCach | 17.3 | MgO (33.8)/NiO (66.2%) |
| Ni-Cach-C | 23.6 | C-graphite (92.6) / Ni (7.4%) |
| NiPt-ZCach-C | 14.8 | NA |
| Ni-MgOAld-C | 27.3 | NA |
| Ni-ZnOAld-C | NA | NA |

NA: Not available

The 3 materials that were not submitted for publication are now discussed, which were Ni-MgOAld-C, Ni-ZnOAld-C and NiPt-ZnOCach. A diffractogram for Ni-MgOAld-C is not available and will therefore not be mentioned further here. Material Ni-ZnOAld-C features a pattern of zinc and nickel carbide (PDF card 28-713), which is a cubic structure with parameters a=b=c=0.366 nm. Ni-ZnOAld-C material also contains diffraction patterns corresponding to metallic nickel and Carbon. The PDF cards are 4-0850 and 26-1080, respectively. The structure of carbon is hexagonal, with lattice parameters a=b=0.2456, and c=1.3392 nm. Corresponding angles are α=β=90 °, and γ=120 °.

Finally, NiPt-ZnOCach material contains only two visible patterns, which are ZnO and NiO. PDF cards are 1-075-0576 and 44-1159, respectively. The lattice parameters for ZnO correspond to a hexagonal structure, where a=b=0.3243, and c=0.5195 nm. The angles of this structure are α=β=90 °, and γ=120°. The structure of NiO is trigonal, with lattice parameters a=b=0.2955, and c=0.7228 nm. The angles of this structure are identical to those of ZnO. It was not possible to detect a ternary phase with nickel and zinc.

### 4.2.3 $N_2$ Physisorption

The physisorption characterization contributed to elucidate important details in textural properties, especially the differences between Cach and Ald materials, which can be translated into stability during catalytic tests. BET area for Ald-supported materials is significantly smaller than for Cach-supported materials. It is possible that Cach support has a similar structure to that of the SBA-15, due to the similarity that there is in the synthesis of the material. This explains the increase in specific surface area, as well as the large difference in structural stability (compared to Ald). Table 6 summarizes the textural properties of the

materials under study, including the 3 materials that were submitted for publication. Subsequent confirmation of the differences between Cach and SBA-15 materials was obtained using the SAXS technique.

**Table 6.** Textural properties of materials used throughout this chapter.

| Material | Specific Surface area ($m^2/g$) | Pore diameter (nm) | Pore volume ($cm^3/g$) |
|---|---|---|---|
| Ni-Ald | 105.9 | 44.9 | 1.25 |
| NiPt-Ald | 120.8 | 40.3 | 1.24 |
| Ni-Cach | 222.1 | 7.1 | 0.41 |
| NiPt-Cach | 224.2 | 9.1 | 0.53 |
| NiPt-ZnOCach | 94.4 | 11.6 | 0.3 |
| NiPt-MgOCach | 50.6 | 18.6 | 0.25 |
| Ni-Cach-C | 188.9 | 10.1 | 0.49 |
| Ni-MgOAld-C | 64.6 | 31.2 | 0.62 |
| Ni-ZnOAld-C | 75.5 | 32 | 0.52 |

A comparison between adsorption and desorption isotherms shows significant differences between the materials supported on Ald and Cach. Ni-Ald and NiPt-Ald catalysts show a typical type II isotherm according to the IUPAC classification, which belongs to the characteristics of macroporous materials. Materials synthesized with Cach support show a type IV isotherm, which corresponds to mesoporous materials. The hysteresis cycle provides information on pore size distribution, pore geometry, and connectivity. On the other hand, samples containing Cach have a hysteresis cycle type $H_2$, characteristic of disordered materials in which the shape and pore size distribution are not well defined. Similar patterns have been reported by Cai *et al.* (2014), who also worked with finely dispersed nickel in mesoporous silicas [115].

Finally, materials that have not been included in the article submitted to the *International Journal of Hydrogen Energy* are mentioned. NiPt-ZnOCach material reminds somewhat of a mesoporous material, due to the use of Cach as a majority support. Also, this

material has a pattern similar to that of the Ni-Cach-C material, which has an irregular hysteresis cycle. N-MAld-C and N-ZAld-C have adsorption and desorption isotherms corresponding to macroporous materials. These materials do not differ at all from the other materials, probably due to the larger pore diameters (with respect to the diameters of materials supported on Cach).

The adsorption and desorption isotherms for samples included in the publication are shown in Figure 16. Isotherms not included in the publication are shown in Figure 17.

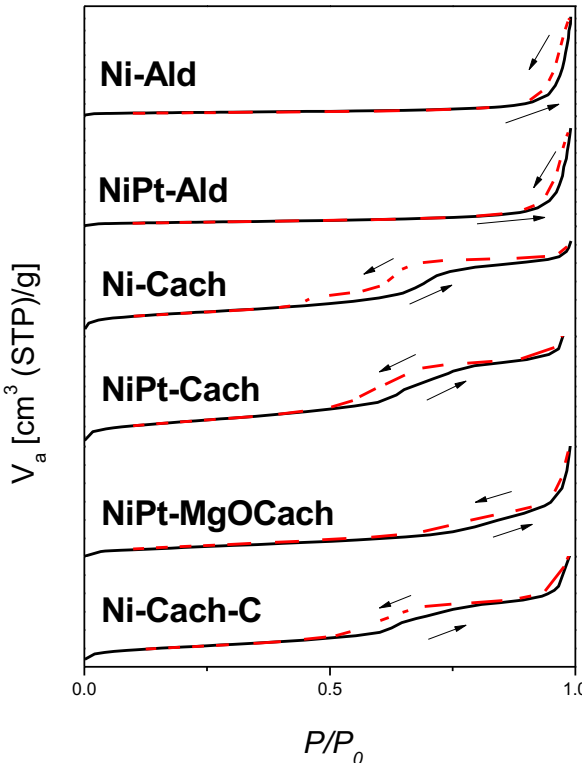


**Figure 16.** Isotherms corresponding to materials submitted for publication.

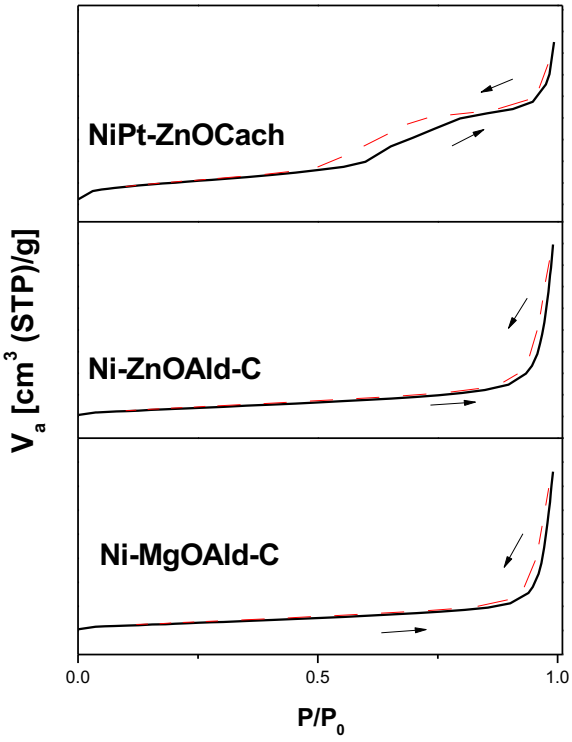


**Figure 17.** Adsorption and desorption isotherms that were excluded from publication.

### 4.2.4 $H_2$-TPR

$H_2$-TPR results are condensed in Figure 18. Ni-Ald, NiPt-Ald, Ni-Cach and NiPt-Cach have a simple composition in common, where NiO clearly dominates. Therefore, the maximum consumption peaks of $H_2$ are in virtually the same temperature range (363-373 ºC). Maximum consumption of NiO at similar temperatures has been reported previously [116]. Cai *et al*. (2014) reported similar temperatures of maximum consumption of $H_2$ which began to increase as the nickel content increased [115]. This phenomenon occurred even though the nickel content was below the one used in this thesis. Hydrogen consumption for Ni-Cach suggests that nickel oxide could be present in a second oxidation state, due to a shoulder with a maximum consumption of $H_2$ to 490 °C. There is also the possibility that the NiO is heavily trapped in the porous structure of the Cach material, which

makes it more difficult to reduce. Finally, NiPt-MgOCach material shows a pattern similar to those previously reported [117, 118]. It has been suggested that interactions between the support and the metal phase (or between metals and oxygen) tend to shift hydrogen consumption temperatures to higher temperatures. Peaks above 500 °C are related to the formation of solid solutions. In the NiPt-MgOCach sample there is only a peak at 828 °C. It should be mentioned that the peak reduction in this material at 411 °C is most likely NiO interacting strongly with the support, since the temperature is slightly higher than the materials Ni-Ald, NiPt-Ald, Ni-Cach and NiPt-Cach. A TPR pattern is not shown for materials Ni-Cach-C, Ni-ZnOAld-C and Ni-MgOAld-C, as the carburization process they were subjected to is highly reductive.

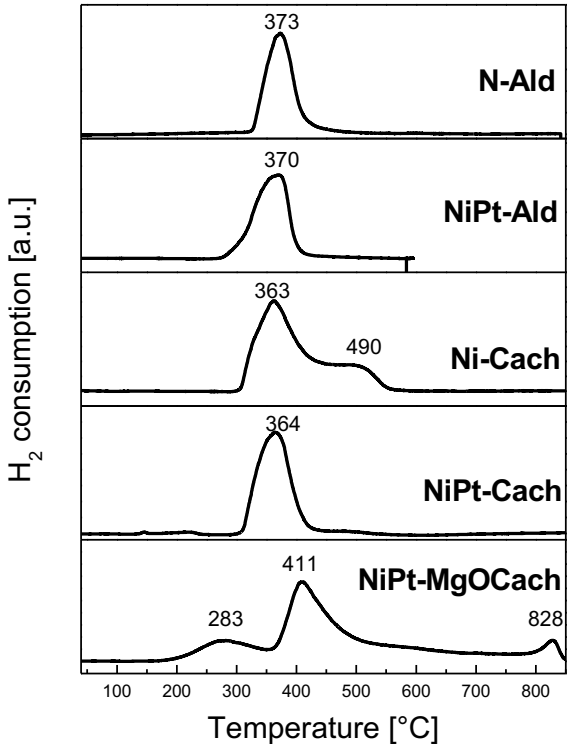


**Figure 18.** $H_2$-TPR profiles corresponding to non-carburized materials.

### 4.2.5 Raman spectroscopy

The Raman spectra of fresh samples are shown in Figure 19. Analyzing samples by groups allowed certain inferences to be made. The first group discussed here includes samples Ni-Ald, NiPt-Ald, Ni-Cach and NiPt-Cach, which are simple in composition. NiO peaks appeared at approximately 490 and 1030 $cm^{-1}$ in the Ni-Ald, NiPt-Ald and Ni-Cach materials, in which the last peak is a bulge. This bulge was moved 15 $cm^{-1}$ in NiPt-Cach material, which could be related to the presence of the Pt precursor or an interaction with the support. Modifications due to interactions between certain metals and the corresponding support have been reported in the past [119]. The resulting peaks of the samples supported on Cach material have a displacement of up to 5 $cm^{-1}$ compared to the materials supported on Ald. The spectra generated by NiPt-MgOCach initially suggest that some complex structures may have formed during calcination. However, similar spectra have been reported for NiO samples with MgO in other studies [120]. Mironova-Ulmane *et al*. (2005) worked with mixtures of NiO and MgO where similar patterns to those reported for NiPt-MgOCach [121]. Between 300 and 800 $cm^{-1}$, 5 peaks are visible, as well as displacements in the NiO bulge, which is displaced up to 1020 $cm^{-1}$. The large peak at 490 $cm^{-1}$ has an upward displacement. These complex structures were not found for each exposure to laser, and many of the resulting spectra were identical to those found for the Ni-Ald and Ni-Cach assays. That is, because no MgO peaks were displayed, the pattern was very similar to those containing only NiO and silica.

Ni-Cach-C is the only material with carbon prior to the catalytic testing so it will not be included in an analysis presented below. The spectrum of this material correlates well with the description of disordered crystalline carbon formations, as they have D and G peaks. D-peaks have previously been associated with double resonance effects, while G-peaks are

more related to intraplanar graphite stretching. Bayer *et al*. (2016) suggested that there is bulk carbon displacement of a nickel-carbon system due to annealing happening at higher temperatures, around 800 °C [122]. These carbon displacements are related to the 2D band. Leng *et al*. (2006) reported the formation of $Ni_3C$ at 256 °C with the use of hydrocarbons [123]. It is highly likely that any carbidic or metallic structure that has been synthesized in this doctoral dissertation was lost at 700 °C, and only a tiny fraction remained after the process was completed.

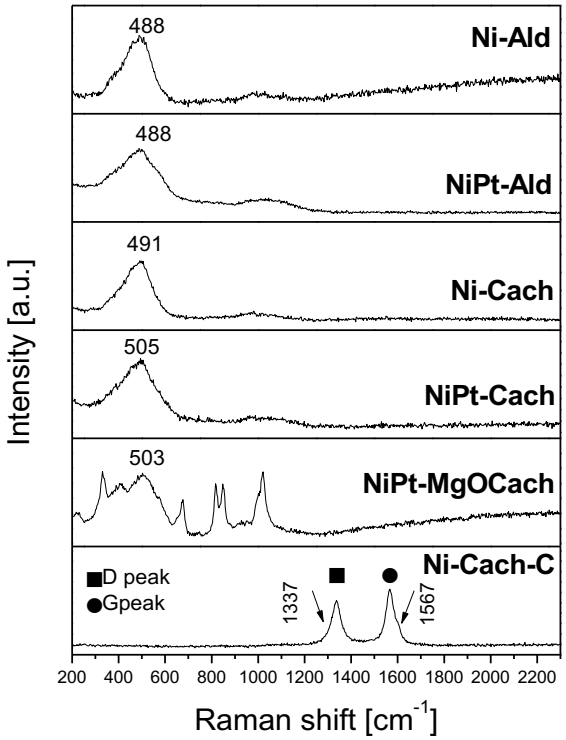


**Figure 19.** Raman spectra corresponding to samples prior to DRM. Only simples included in the article are shown in this figure.

NiPt-ZnOCach material contains ZnO and NiO patterns that are very easy to distinguish and can be compared with literature reports [124].

Finally, N-MAld-C and N-ZAld-C materials are analyzed. These were materials subjected to the carburization process but with no activity. In the case of Ni-ZnOCach-C, carbide formation was successfully synthesized, as visualized by XRD. However, carbidic compounds could not be visualized using Raman spectroscopy. Therefore, only an analysis of carbon peaks will be done. G-bands appear at 1575 and 1567 $cm^{-1}$ for N-MAld-C and N-ZAld-C, respectively. D-bands appear at approximately 1340 $cm^{-1}$ for both. While it is not possible to deduce greater differences between the two. Peak intensities are much higher for Ni-Cach-C, and much lower for Ni-ZnOAld-C (where the bimetallic carbide was confirmed). Regarding Ni-Cach-C and Ni-ZnOAld-C assays, the spectrum N-MAld-C has an intermediate value for the G-band, while its D-band has a value very similar to that of N-ZAld-C. It can be inferred from this that the carbon present in N-MAld-C and N-ZAld-C are considerably less disordered than in Ni-Cach-C. Raman spectra for fresh materials that were not submitted for publication are shown in Figure 20.

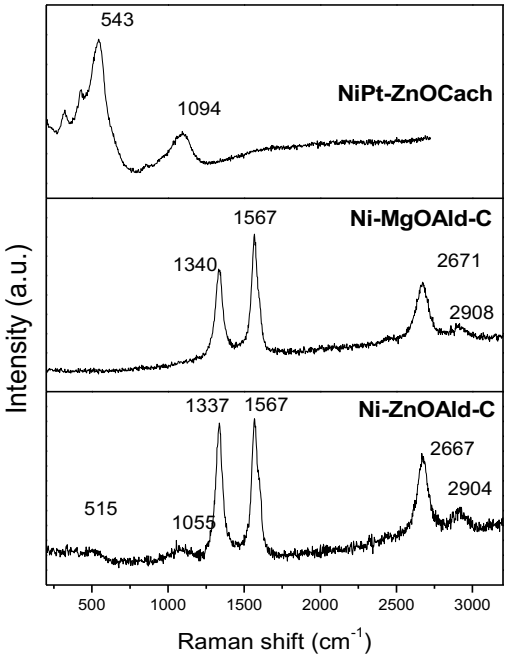


**Figure 20.** Raman spectra corresponding to fresh materials excluded from publication.

## 4.2.6 HR-TEM

HR-TEM micrographs were only taken from samples Ni-Cach and Ni-Cach-C prior to DRM, which allowed to make some conclusions regarding characterization. The analysis confirmed that the carburization process was successful in synthesizing nickel carbides, as crystalline $Ni_3C$ was visualized. According to d-spacing of (104) planes, particle sizes were only a few tens of nanometers. The carbide phase was evidenced by HRTEM, but it was not detectable by XRD. This suggests that $Ni_3C$ was present in concentrations below the lower limit of detection (<1% m/m). The micrographs also reveal $Ni_2O_3$ particle being surrounded by deposited carbon during the carburization process (Figure 21). The fact that these particles are encircled by carbon helps explain why no carbide phase was visualized via Raman spectroscopy, as it is a surface-only study.

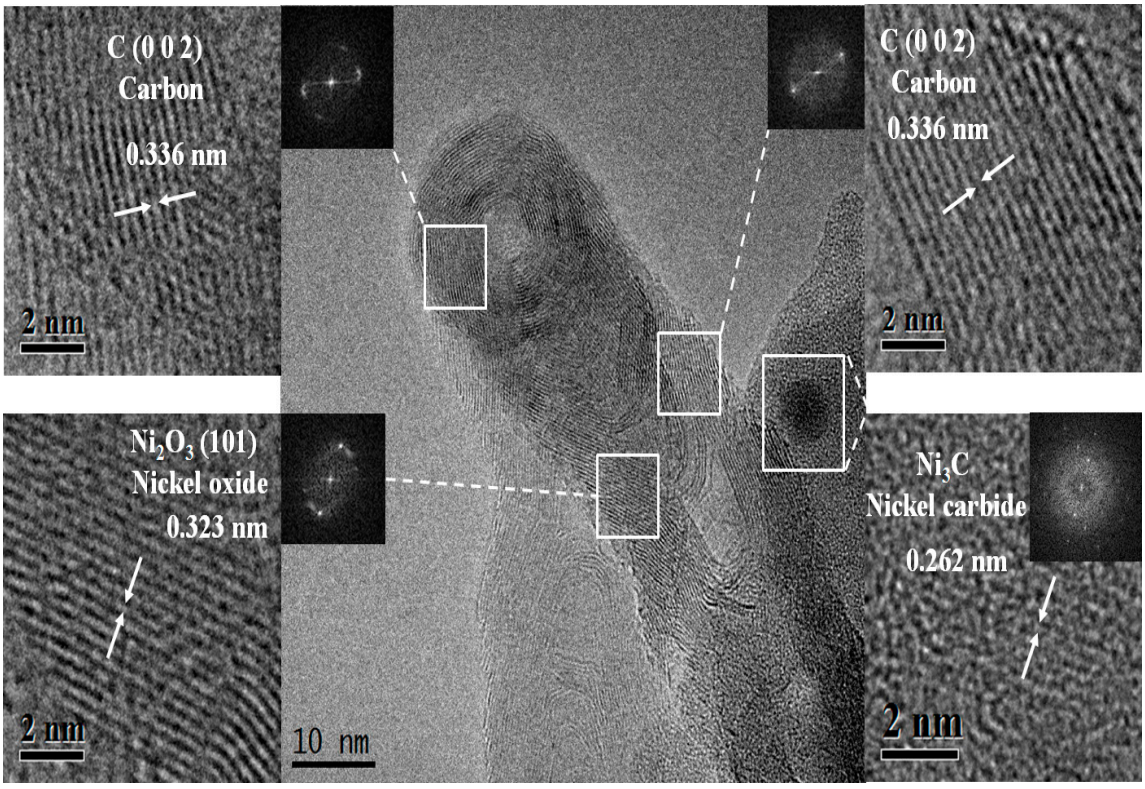


**Figure 21.** Micrographic evidence of the successful synthesis of $Ni_3C$.

## 4.3 Catalytic Tests

Before proceeding with this section, it will be noted that NiPt-MgOCach was synthesized completely by incipient wetness impregnation for short-term testing. However, for long-term testing, MgO was added as a powder to the synthesis. This may contribute to explaining the stark contrast between short and long-term testing.

### 4.3.1 Short-term testing

Short-term evaluations were used to determine which materials had catalytic activity. Of the 9 materials available in the initial group, only 4 of them had acceptable conversions of $CH_4$ and $CO_2$ for a period of 4 hours. Of the other 5, one of them had very low conversions (around 10%) and remained stable. The 4 materials that withstood the high reaction temperatures without losing activity will be discussed below. Results corresponding to active materials are shown in Figure 22, which includes $CO_2$ and $CH_4$, conversions, as well as the $H_2$/CO ratio.

The materials with high catalytic activity were the mixtures Ni-Cach, NiPt-Cach, NiPt-MgOCach and Ni-Cach-C. As has been described previously, the material subjected to carburization processes contained high amounts of graphitic carbon. It was already expected that materials containing mesoporous $SiO_2$ would be the best catalysts, as they increase the quality of active sites thanks to their channels and high surface area [96].

The material with extremely low catalytic activity but without deactivation was NP-MAld. The gas conversions were at an estimated 10%. Even though this activity is very low, an interaction occurring between MgO and the carburization process is suspected.

As for the other 4 materials, the Ni-Ald and NiPt-Ald mixtures started with high activity but deactivated before the first hour of reaction. The fact that NiPt-Ald deactivated even though it contained Pt was contrary to expectations.

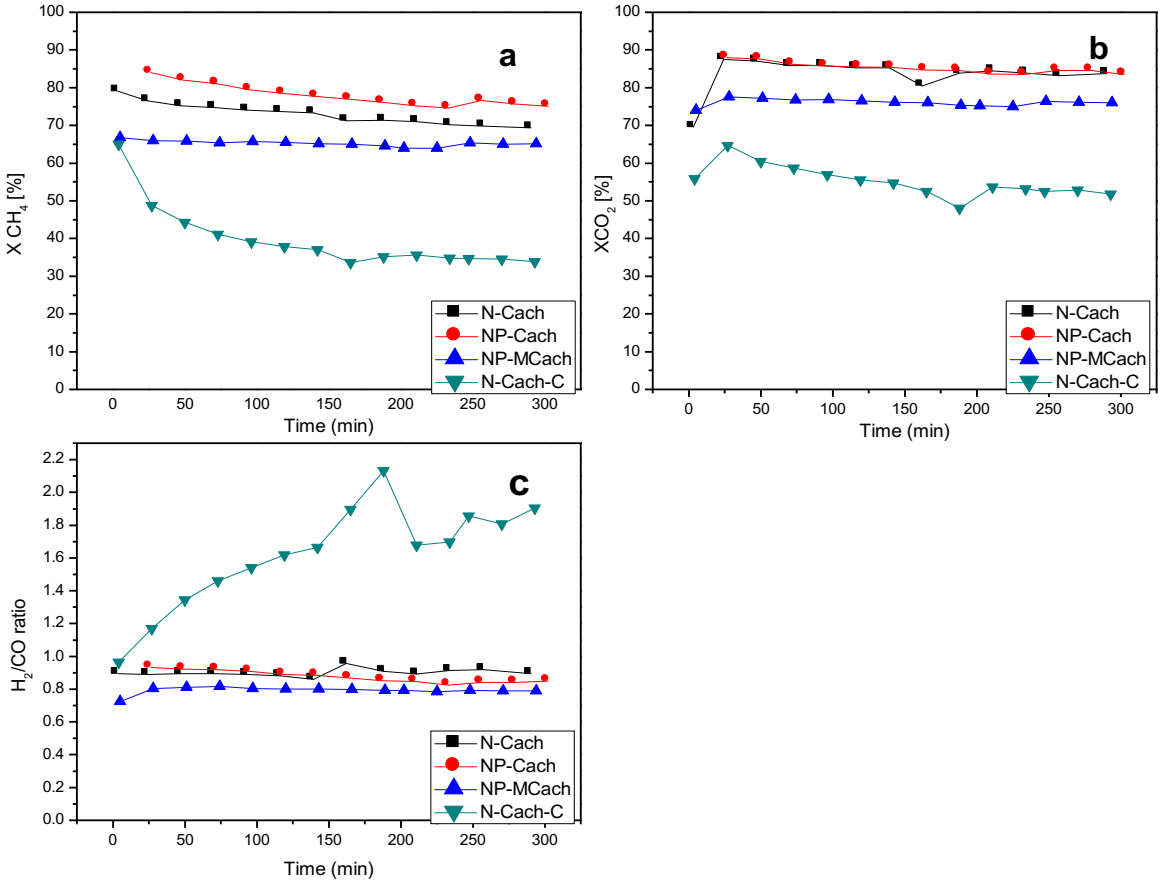


**Figure 22.** Results for short-term catalytic activity for materials Ni-Pt. a) $CH_4$ conversion, b) $CO_2$ conversion, c) $H_2$/CO ratio. T= 700°C, P= 1 atm, GHSV= 57450 $cm^3\ g._{cat}^{-1}\ h^{-1}$.

With these observations, the possibility that $SiO_2$ supports could be of very different textural properties began to be considered (later confirmed by $N_2$-Physisorption). A visual inspection of the samples after the reaction suggested that they all had carbon deposits. Hence, the inference was made that the materials supported on Ald were more susceptible to

high temperatures than Cach materials, which had been synthesized with Pluronic P123 macromolecular template.

On the other hand, the materials with ZnO were not effective in catalytic conversions, as there was low production of hydrogen and CO. In terms of alkalinity, questions of interest appear. What fundamental difference is there between MgO and ZnO that allowed one to convert reactants and the other not? What interaction can occur between SiO2 support and ZnO intervening in active sites? It was logical to think that, if the alkalinity of MgO contributed to the stability of the catalyst, then ZnO can also positively influence results.

Finally, the presence of carbon for all spent samples would not be confirmed until Raman analysis could be undertaken. This is shown in Chapter 6, concerning carbon formations.

### 4.3.2 Long-term Testing

Long-term catalytic tests were carried out for the 4 best catalysts after the screening phase was over. Perhaps the most interesting of the results obtained is the simplicity of catalyst Ni-Cach, from which little stability was expected prior to short-term testing. This sample contains about 20% by weight in nickel and does not have a promoter, but still exhibited very high stability and a ratio of $H_2$/CO slightly higher than 1. Stability was maintained for 55 hours. The sample started with better $CH_4$ conversions, contrary to $CO_2$, which started with lower conversions and stabilized after 1 h. While the average crystal size obtained by XRD is greater than the average pore size, there is a wide variety of particle sizes, as revealed by HR-TEM microscopy. This allows to to assume that there is a population

of nickel particles that are deeply interned in the mesopores of the material [93, 96]. This possibility becomes more feasible when analyzing $H_2$-TPR results, which show a primary peak corresponding to NiO, and a secondary region of hydrogen consumption, which reaffirms that there is a more difficult fraction of NiO to reduce. In the case of the sample with MgO, this becomes more noticeable due to the peak consumption close to 900 °C.

The use of platinum and nickel did not have a greater influence on conversions, although arguably it may have had a positive effect on stability. $H_2$-TPR characterization reveals how the maximum consumption of $H_2$ is confined to only one thermal region, so it could be assumed that a fraction of encapsulated nickel in this material does not exist or is much smaller, which is why no $H_2$ consumption peaks appear at greater temperatures. Despite this, the catalytic activity of this material is practically identical to the material without platinum. This may be because the presence of a second metal (bimetallic catalysts) can improve the reduction of the active phase and facilitate an oxide-reduction system in the catalyst, thereby regenerating the material. On the other hand, similar conversions of the catalyst with Pt from the one lacking it suggest that the dispersions of the noble metal could have been very low. Poor dispersion of the metal could be related to the way it was mixed into the material, which consisted only of dissolving Pt $(acac)_2$ in dichloromethane before adding it. It has previously been reported that there is an optimal ratio of Pt to Ni, since exceeding that limit could lead to an excess in methane chemisorption, thus reducing $CO_2$ conversions [125]. Thus, it is likely that the limit in a Pt to Ni ratio was surpassed.

Contrary to expected, the long-term test for NiPt-MgOCach material was not as stable in long-term testing as in the short testing. This can be explained in part by the way MgO was added, which has already been described at the beginning of section 4.3 which may have

interfered in proper formation of solid solutions. $CH_4$ conversions were slowly in decline (without being completely deactivated), and still had a 70% conversion after 30 hours. However, the $CO_2$ conversion remained at higher levels. These results are consistent with some previous results in which MgO and SBA-15 have been used in conjunction with Ni as an active phase [117]. Also, there are reports that mention the effectiveness of MgO in catalyst stability [126, 127].

Regarding catalytic activity of Ni-Cach-C, the high presence of graphitic carbon should be considered (according to the results of XRD and Raman). It is therefore interesting that, despite the high carbon percentages, there was no catalyst deactivation, which seemed to stabilize after 30 hours of reaction. This suggests that bulk and surface modifications occur resulting in the generation of a stable catalyst. This would imply that coal is acting as a kind of support, which could be further explored in future studies. The addition of carbon *(carbon black* type) has been linked with modifications in textural characteristics previously. These modifications are mainly an increase in total pore volume and mesopore volume, although it is also possible to visualize large changes in the hysteresis cycle. These variations are achieved at the cost of losing specific surface area [128]. It is important to comment on the rapid deactivation of the material with respect to the other samples supported on Cach. This rapid deactivation could be related to the disappearance of $Ni_3C$ species detected by HR-TEM, which were present at the start of the experiment. It is highly likely that there has been a carbon separation from the nickel carbide phase, after which only metallic nickel would have remained as an active phase. The material would then have been mainly dependent on the intrinsic resistance of the mesoporous support. This would be further confirmation for the

quality of nickel carbide species to be metastable [Bayer]. Long-term test results are shown in Figure 23, which include $CO_2$ and $CH_4$ conversions, as well as $H_2$/CO ratio.

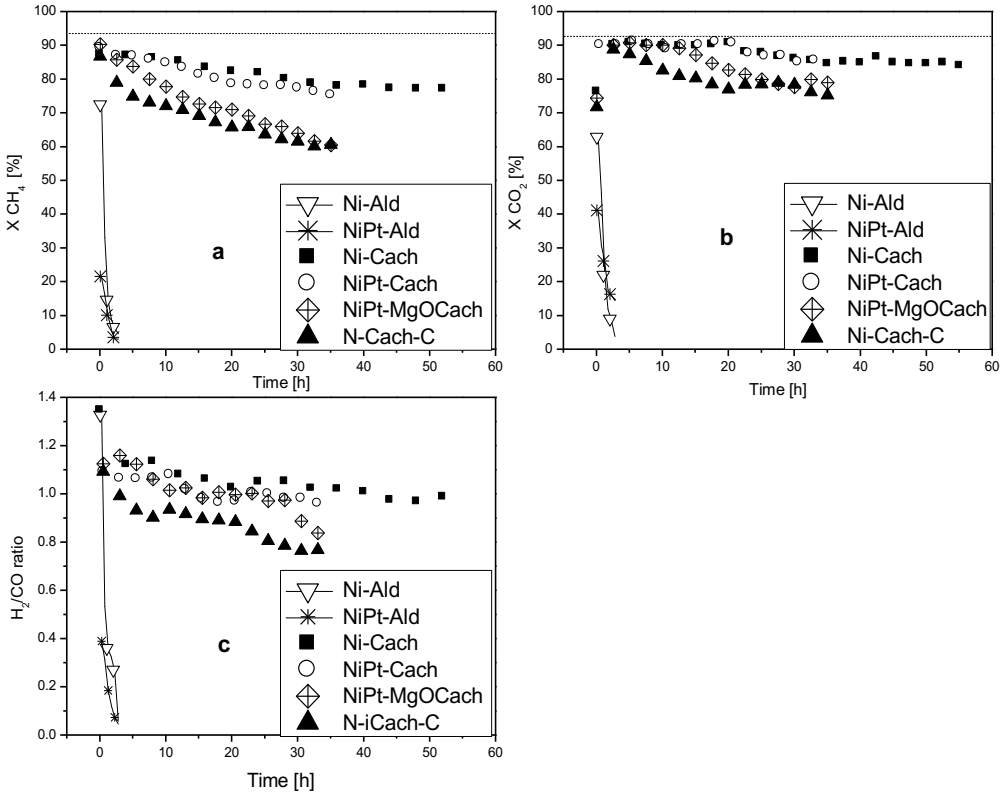


**Figure 23.** Long-term catalytic test results. a) Methane conversions, b) $CO_2$ conversions, and c) $H_2$/CO ratio. T= 700°C, P= 1 atm, GHSV= 57450 $cm^3\ g_{.cat}^{-1}\ h^{-1}$

## 4.4 Chapter Conclusions

Short-term Evaluations

In the initial screening with nickel and platinum samples, nine samples were studied. Of the nine samples, only 4 of them had catalytic activity. These are the Ni-Cach, NiPt-Cach, NiPt-MgOCach and Ni-Cach-C samples. Short-term evaluations were interrupted after 4 hours. The most interesting results at this stage were the high stability of the NiPt-MgOCach

material and the activity of the Ni-Cach-C material. This is not to say that Ni-Cach and NiPt-Cach materials do not provide interesting information and will also be discussed briefly here.

NiPt-MgOCach was of great interest at this stage as it shows no deactivation signals over the 4 hours of testing. $CO_2$ and $CH_4$ conversions show no decrease in that period.

Ni-Cach-C material, on the other hand, had relatively rapid deactivation, but within 4 hours it began to stabilize (%). This was a clear indication of the presence of carbon and its positive properties for catalytic reactions. However, the notion of carbon importance would be strengthened in subsequent studies. In the initial tests it was concluded that deposed carbon did not induce immediate deactivation. The physisorption tests reveal that the Cach material does not completely lose its properties. It is natural that there is a reduction in specific surface area, but the hysteresis cycle allows to see that mesoporosity has been maintained in part at least.

On the other hand, the Ni-Cach-C material once presented an $H_2/CO$ relationship close to 2. This trend was not maintained in other experiments. However, a common behavior to this material is a drop in $CH_4$ and $CO_2$ conversions before stabilizing around 40%. It is to be suspected that in this case there was a rapid destruction of $Ni_3C$ particles, which were separated into their individual components before the system stabilized.

There were no major differences between the Ni-Cach and NiPt-Cach materials. The reactant conversions are slightly higher in NiPt-Cach material, approximately by 3%. It is surprising that, despite the addition of Pt, there is no better conversion of reactants in NiPt-Cach material. However, the most interesting differences are found in the analysis of spent materials.

Materials supported on Ald were not suitable for use in DRM, even with the addition of platinum. This low activity is due to the textural characteristics of the Ald material. Although pore diameter would suggest that Ald belongs to mesoporous materials, the adsorption isotherm reveals a pattern corresponding to macroporous materials. Macroporous materials necessarily efficient for catalysis, as they do not contribute as much to the encapsulation of the active phase, and therefore does not sufficiently prevent the appearance of carbon deposits.

Even though 5 materials were discarded, one of them remains attractive from the point of view of Raman spectroscopy. In the case of N-ZAld-C material, carbon peaks show a ratio of $I_D/I_G$ greater than 1, which means that there is more disordered carbon than graphitic. It should be remembered that this material contained high amounts of carbon prior to the reaction of the reaction, and the ratio between D-peaks and G peaks was slightly less than 1.

Long-term evaluations (Ni-Pt)

The most interesting results of this section can be found in the Ni-Cach and NiPt-Cach materials. There was no real difference between these materials, despite the presence of platinum in NiPt-Cach material. The central explanation here lies in how the platinum precursor was added. An explanation that helps explain the small or no difference between the Ni-Cach and NiPt-Cach materials is found in $H_2$-TPR. The Ni-Cach material has two sections of hydrogen consumption. The first consumption area is at a temperature of 370 ºC, while the second maximum consumption temperature is 490 ºC. NiPt-Cach material only has the peak consumption at the lowest temperature. Therefore, the Ni-Cach material has a

fraction of nickel that is more difficult to reduce, which may be due to stronger interactions between support and active phase.

Another interesting case in long-term evaluations is that of NiPt-MgOCach. This material was not as effective converting $CH_4$. However, it was more successful in $CO_2$ conversion. The conversions of this reactant remain very stable after an initial decrease and can be interpreted as a capability on the part of the material to chemisorb to $CO_2$ due to attraction by alkaline materials, which has been observed in the past [129].

Finally, material Ni-Cach-C entered the reaction with carbon formations derived from the carburization process. The Raman spectrum of this sample indicated that there is a more orderly carbon at the start of the reaction than at the end of the reaction. Of the 4 materials that were evaluated for more than 30 hours, this is the only material that presents a Raman spectrum with highly disordered carbon formations, in addition to a D' peak related to faulty graphene. This indicates that the reforming process was more severe for this sample, probably due to a forced restructuring of existing deposits at the start of the reaction. Interestingly, there was no deactivation in this sample, although the reactant conversions were very similar to those of NP-MgOCach material.

A reduction in the $H_2$/CO ratio in NiPt-MgOCach and Ni-Cach-C indicates that there might be a mechanism that favors producing CO. In NiPt-MgOCach material it is easier to explain, as there is a tendency to chemisorb better $CO_2$ due to pH differences, making it easier to transform it into CO. It is not so easy to explain this mechanism in the Ni-Cach-C material, but it is likely that there is a mechanism that follows the oxidative path of C-H groups, which can contribute to raising the amounts of CO produced.

Differences between short and long-term evaluations (Ni-Pt)

In general, behaviors between short and long evaluations follow the same behavior. However, the pattern is broken for conversions in the NiPt-MgOCach material. The explanation lies in the mode of preparation. A description of the synthesis is then made as a reminder.

The active phase was added using the incipient wet impregnation technique. In cases where there was addition of ZnO precursor, incipient wetness impregnation was also used. When there was addition of MgO precursor, the wet impregnation method was used. However, there was one case in which MgO was added directly to the synthesis, without an impregnation. The impregnation-synthesized catalyst was used for short-term evaluations, whereas the catalyst with direct addition of MgO was applied for long-term evaluations.

It was mentioned in the previous subsection that NiPt-MgOCach material showed no deactivation signals in the 4-hour period for any of the reactants. However, this behavior was not as ideal for long-term tests, although at no point did it show any signs of being completely deactivated, especially for $CO_2$ conversions. In this case it can only be concluded that the mode of addition of materials is defining in the quality of the catalyst. Although the direct addition of MgO to the catalyst was done with the help of ultrasound (in order to improve mixing), the final quality is lower compared to the material completely synthesized by the impregnation method.

# Chapter 5:
# Ni and Mo catalysts on
# $SiO_2$ and nanoparticulate ZnO

## 5.1 Generalities pertaining to this Chapter

Before beginning this section, some details that should be kept in mind are shown in a list below.

1) Problems regarding argon supply arose and worsened after technical issues.
2) Therefore, only short-term catalytic evaluations took place (4 h).
3) The results presented herein are thus not conclusive, as new compounds could arise if given enough time and enough carbon deposition.
4) One of the materials is not characterized fully (Mo-Cach), but most results are presented.

### 5.1.1 List of catalytic materials

Table 7 summarizes the materials used for studies with nickel and molybdenum. It should be remembered that the ZnO used in this section is nanoparticulate and was thus not synthesized via incipient wetness impregnation.

Table 7. Materials and nomenclature used for nickel and molybdene studies.

| Name | Content |
|---|---|
| Ni-$Z_{np}$ | Ni (10)/ZnO |
| Ni-$Z_{np}$Cach | Ni (10)/ZnO (15)/Cach |
| Ni-$Z_{np}$Cach2 | Ni (10)/ZnO (40)/Cach |
| NiMo-$Z_{np}$ | Ni (10)/Mo (10)/ZnO |
| NiMo-Cach | Ni (10)/Mo (10)/Cach |
| Mo-$Z_{np}$ | Mo (10)/ZnO |
| Mo-Cach | Mo (10)/Cach |
| NiMo-$Z_{np}$-C | Ni/Mo/ZnO (carburized) |

## 5.2 Characterization

All materials were characterized in their oxidized state, except for sample NiMo-Znp-C.

### 5.2.1 WDXRF

Table 8 concentrates the results of the X-ray fluorescence analysis corresponding to the materials in this section.

**Table 8.** XRF results corresponding to materials with NiO, $MoO_3$ and ZnO.

| **Material/Componente** | **NiO (%)** | **$MoO_3$ (%)** | **ZnO (%)** | **Cach (%)** |
|---|---|---|---|---|
| Ni-$Z_{np}$ | 15.13 | -- | 84.87 | -- |
| Ni-$Z_{np}$Cach | 18.33 | -- | 21.73 | 59.94 |
| Ni-$Z_{np}$Cach2 | 17.98 | -- | 17.41 | 64.61 |
| NiMo-$Z_{np}$ | 13.32 | 18.85 | 67.83 | -- |
| NiMo-Cach | 21.09 | 17.46 | -- | 61.45 |
| Mo-$Z_n$ | -- | 21.3 | 78.7 | -- |
| Mo-Cach | NA | NA | NA | NA |

NA: Not available.

### 5.2.2 XRD

XRD patterns for the materials in this chapter are shown in Figure 24. Diffraction characterization revealed major differences (with respect to the materials used in section 3.1) in terms of active-support phase interactions, as well as active phase interactions. These interactions can be correlated with Raman spectroscopy results, and also allow inferences to be made with $H_2$-TPR and $N_2$ physisorption techniques. It is also conspicuous that there is a higher degree of complexity in terms of formed compounds, which expands the possibilities in terms of catalytic properties.

The Ni-$Z_n$ material showed two defined patterns, one of which was a non-stochiometric nickel oxide with the formula $Ni_{1.875}O_2$ (PDF card 01-072-4521). This structure was identified as monoclinic and with a space group C2/m. The other pattern was ZnO (PDF

card 1-074-9939), identified as zincite, with hexagonal structure and space group P63mc. A mixed oxide pattern was not detected.

Ni-$Z_{np}$Cach and Ni-$Z_{np}$Cach2 materials have very similar patterns, as they contain the same materials, albeit in different proportions. These patterns are characterized by an amorphous curve with center at 22 degrees 2θ, corresponding to $SiO_2$ (Cach). Discernible patterns are zincite (PDF card 1-073-8765) and a mixed nickel and zinc oxide with formula $Ni_{0.9}ZnO_{0.1}$ (PDF card 1-079-7848). This material has a trigonal structure and with space group R-3m. Interestingly, mixed oxides of nickel and zinc were not able to form in the Ni-$Z_{np}$ material, even though the proper precursors were present.

NiMo-$Z_{np}$ material features a combination of mixed oxides. One of them is nickel molybdite (PDF card 01-086-0362), with monoclinic structure and spatial group P2/c. The other pattern identified corresponds to the zinc molybdate (PDF card 01-070-5387), with triclinic structure and P-1 space group. The other phases present are non-stochiometric nickel oxide with formula $Ni_{1.875}O_2$ (PDF card 01-072-1464) and zincite.

NiMo-Cach was not a particularly crystalline material, although some phases were identifiable. Such phases were nickel molybdate (PDF card 1-086-0362) and non-stoichiometric nickel oxide with a $Ni_{15}O_{16}$ (PDF card 1-074-6700). In addition to these oxides, molybdite was also identified (PDF card 1-074-7911), with an orthorhombic structure and space group Pbnm. An amorphous curve pertaining to Cach is also to be seen.

Mo-$Z_{np}$ showed a pattern corresponding to zinc molybdate (PDF card 1-070-5387). Zincite was also identified on this pattern. As to Mo-Cach, no analysis is presented. Due to non-existing activity, no diffraction pattern is shown.

Finally, the use of XRD confirmed the presence of multiple compounds and alloys in NiMo-$Z_{np}$-C. The compounds that were identified were a mixed carbide of zinc and nickel ($Ni_3ZnC_{0.7}$, PDF card 28-0713), as well as molybdene carbide (1-076-8649). The mixed carbide is of a cubic structure with a Pm-3m space group, whereas molybdenum carbide is hexagonal, with a P63/mmc space group. As for the alloys, these were MoNi and NiZn, with PDF cards 1-071-9762 and 1-072-2668, respectively. MoNi is also hexagonal with a P63/mmc space group. NiZn is tetragonal and with a space group I4/mmm. NiZn and nickel and zinc carbide were both reported by Sokolov *et al*. (2017), where the conversion from NiZn to a mixed carbide is confirmed [130].

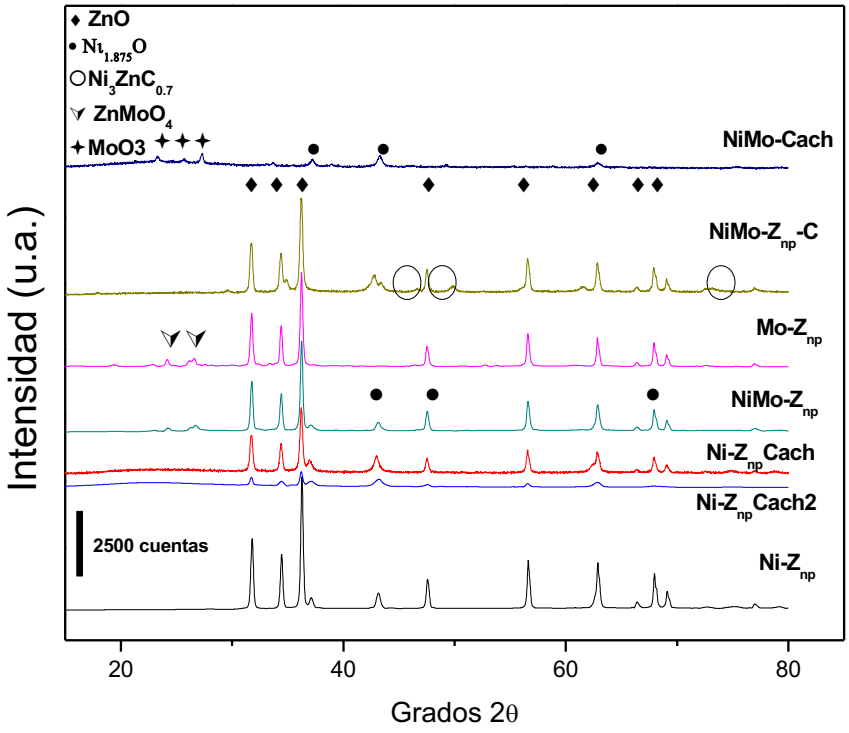


**Figure 24.** XRD patterns corresponding to Ni-Mo materials.

*5.2.2.1 Crystal size determined by XRD*

Table 9 shows the average crystal size for both NiO and metallic nickel phase.

**Table 9.** Crystal size for Ni-Mo materials.

| Material | Crystal size (nm) |
|---|---|
| Ni-$Z_{np}$ | 60.1 |
| Ni-$Z_{np}$Cach | 49.9 |
| Ni-$Z_{np}$Cach2 | 53.1 |
| NiMO-$Z_{np}$ | 61.4 |
| NiMo-Cach | 21.7 |
| Mo-$Z_{np}$ | 58.2 |
| Mo-Cach | NA |
| NiMo-$Z_{np}$-C | 47.7 |

NA: Not available

## 5.2.3 $N_2$-Physisorption

Adsorption and desorption isotherms are shown in figure 25. $N_2$ physisorption provides multiple data, as two types of adsorption and desorption isotherms can be distinguished easily. Those materials supported on Cach have isotherms of mesoporous materials, while those using ZnO as support have macroporous characteristics. Although many new materials are formed (according to diffraction patterns), there are no variations in the textural characteristics of the majority supports. Materials with mesoporous characteristics are Ni-$Z_{np}$Cach, Ni-$Z_{np}$Cach2, NiMo-Cach and Mo-Cach, while those with macroporous characteristics are Ni-$Z_{np}$, NiMo-$Z_{np}$, Mo-$Z_{np}$ and NiMo-$Z_{np}$-C. Interestingly, the characteristics of Ni-$Z_{np}$Cach and Ni-$Z_{np}$Cach2 materials are not modified despite the strong presence of ZnO. The macroporous characteristics of NiMo-$Z_{np}$-C material, remain unmodified despite the high presence of graphite carbon.

The isotherms corresponding to mesoporous materials show an unusual hysteresis cycle. These bear some resemblance to the H5 hysteresis cycle, which is related to materials that have both open and closed pores. These situations can occur in syllables manufactured with template, which is the case for this material. On the other hand, it also has similarity to the type H1 cycle, even if it is highly deformed. This deformation suggests that there is a fairly large pore size range. That is, it is repeated what is observed for Ni-Pt catalysts, where it is concluded that there is little uniformity in pore size. Table 10 contains the results for $N_2$ physisorption over Ni-Mo catalysts.

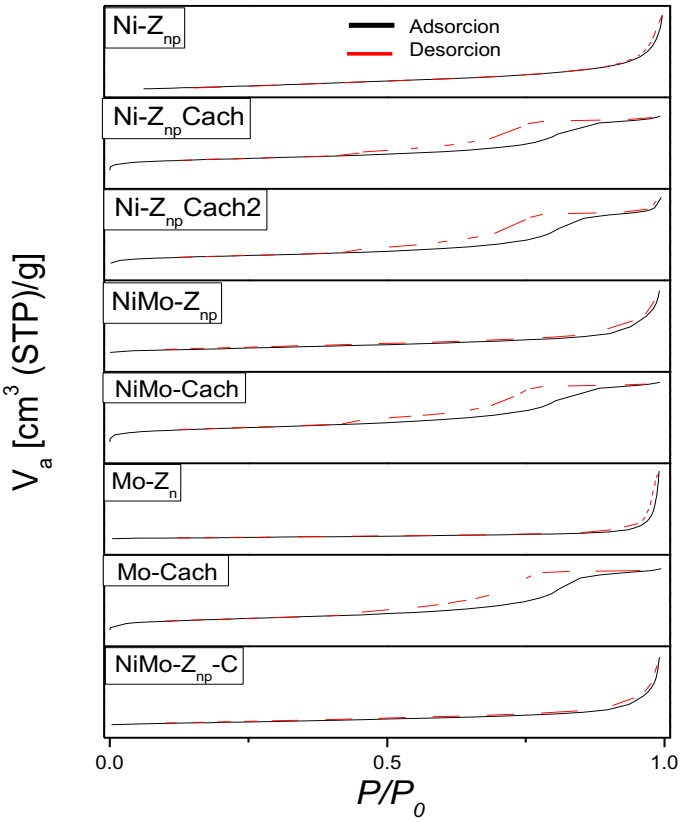


**Figure 25**. Adsorption and desorption isotherms corresponding to Ni-Mo materials.

**Table 10.** Physisorption results corresponding to Ni-Mo catalysts.

| Material | Surface area ($m^2/g$) | Pore diameter (nm) | Pore volume ($cm^3/g$) |
|---|---|---|---|
| Ni-$Z_{np}$ | 8.3 | 13.3 | 0.03 |
| Ni-$Z_{np}$Cach | 327.1 | 7.1 | 0.58 |
| Ni-$Z_{np}$Cach2 | 150.3 | 10.5 | 0.39 |
| NiMo-$Z_{np}$ | 10.6 | 19.4 | 0.05 |
| NiMo-Cach | 312. | 6.8 | 0.53 |
| Mo-$Z_{np}$ | 12.6 | 53.7 | 0.17 |
| Mo-Cach | 380.1 | 8.0 | 0.76 |
| NiMo-$Z_{np}$-C | 14.0 | 25.4 | 0.09 |

### 4.2.4 $H_2$-TPR

Results corresponding to $H_2$-TPR are without doubt some of the most interesting ones, as it shows metal oxide fractions that are very easy to reduce (at normal NiO reduction temperatures), and metal oxide fractions that are more difficult to reduce or nearly impossible (above DRM reaction temperatures). These results are of high importance as they have high correlation with the catalytic activity of the catalyst batch. $H_2$-TPR graphs pertaining to Ni-Mo materials are shown in figure 26.

The first group of catalysts analyzed in this section is the one that has only NiO as a precursor to the active phase. These catalysts were still reduced to relatively low temperatures, within a range considered normal for NiO [131].

The next group of catalysts is one containing both nickel and molybdenum (mixed oxide), as has been suggested previously [132]. These materials were harder to reduce, but without excessively high temperatures. This suggests that the addition of nickel facilitates the reduction of compounds formed during calcination of materials. Thus, several peaks or regions of maximum hydrogen consumption can be visualized.

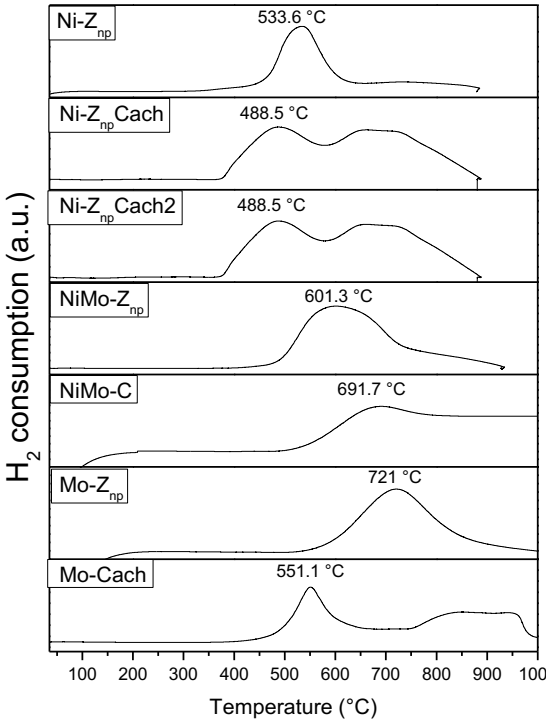


**Figure 26.** $H_2$-TPR results for Ni-Mo materials.

The last set to be analyzed includes only the two molybdenum oxide materials. These catalysts are characterized by being practically impossible to reduce, exceeding normal limits of dry reforming. The difficulty of reduction explains why the vast majority of experiments reporting the use of molybdenum have chosen to synthesize a carbide with this metal instead of using it as an oxide. Synthesis temperatures of molybdenum carbide are around 800 ºC, and this temperature is lower than the reduction temperature seen in these experiments.

## 5.2.5 Raman (fresh samples)

Raman spectra have a high correlation with diffractograms, regarding the materials formed during synthesis. That is, by firstly identifying X-ray diffraction patterns, a search of the corresponding Raman patterns could be done. Subsequently, these confirmed materials were searched separately to find the corresponding Raman spectrum. It should be mentioned that not all phases present in X-ray analyses could be visualized by Raman for each spectrum. The Raman spectra for Ni-Mo materials are shown in Figure 27.

The easiest patterns to discern are those that correspond to the NiO and ZnO. NiO is easy to visualize in Ni-$Z_{np}$, Ni-$Z_{np}$Cach, Ni-$Z_{np}$Cach2, NiMo-Cach and NiMo-$Z_{np}$-C, especially at a frequency of approximately 530 $cm^{-1.}$ Although there is a bulge (approximately 1100 $cm^{-1}$) that agrees with the results of the Ni-Pt section, this second formation does not appear in all materials as it is not present in NiMo-Cach.

Meanwhile, the formations corresponding to the ZnO coincide with approximately 330 and 425 $cm^{-1}$ in the materials Ni-$Z_{np}$, Ni-$Z_{np}$Cach, Ni-$Z_{np}$Cach2, Mo-$Z_{np}$ and NiMo-$Z_{np}$-C. However, the peaks appear to be of lower intensity in the Mo-$Z_{np}$ material, but the pattern remains identifiable.

The most interesting resulting phases are those corresponding to molybdates (confirmed via XRD). It is difficult to make a comparison between zinc or nickel molybdate, as the patterns reported in the literature are very similar [133, 134]. Materials containing molybdates are NiMo-$Z_{np}$, NiMo-Cach, Mo-$Z_{np,}$and NiMo-$Z_{np}$-C. Thus, there is a possibility that what is being observed in the graph is the excitation of the Mo-O links, as opposed to viewing Raman spectra for a defined compound. The pattern of the NiMo-Cach material (which is most likely nickel molybdate, due to the material content) differs from the other

materials as it lacks the band at approximately 880 $cm^{-1.}$ This peak can be found in both zinc molybdate or nickel. Alternatively, the pattern in Mo-$Z_n$ is very different from other patterns, as it has more peaks.

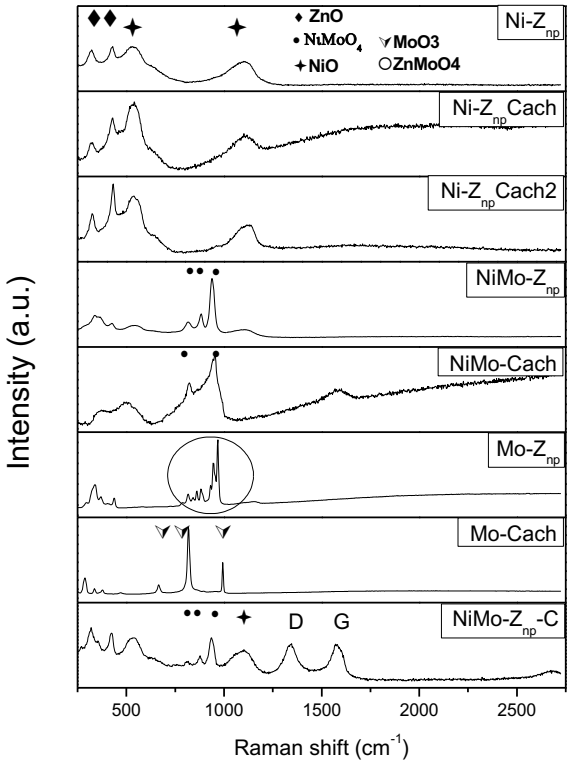


**Figure 27.** Raman spectra corresponding to Ni-Mo, some of which contain carbon-related peaks.

Mo-Cach material has a strong similarity with molybdenum oxide in its molybdene form ($MoO_3$), and is not related to molybdenum patterns [135].

Finally, the NiMo-$Z_{np}$-C material also has peaks corresponding to disordered graphite carbon, some of which lack crystallinity. As seen previously, these peaks are called D and G, and appear at 1346 and 1570 $cm^{-1}$, respectively. These values are close to those reported for Ni-Cach-C material in the Ni-Pt catalyst section.

## 5.3 Catalytic Evaluations

The active catalysts in this section had minor conversions with respect to Ni-Pt catalysts, although they also appeared to have a slow deactivation pattern. These materials were Ni-$Z_{np}$, NiMo-$Z_{np}$, NiMo-Cach and NiMo-$Z_{np}$-C. The deactivation mechanisms in non-active materials will be explained first. The results of the catalytic evaluation are shown in Figure 28, and include $CO_2$ and $CH_4$ conversions, as well as the $H_2$/CO ratio. Only the profiles of 4 materials are displayed, as only one hour of evaluation could be done for the others.

Materials Ni-$Z_{np}$ and Ni-$Z_{np}$Cach are mixtures resulting from nanoparticulate ZnO, nickel and Cach. In the adsorption and desorption isotherms it was possible to see that, despite using ZnO, the catalytic material did not lose its mesoporous characteristics. Diffraction patterns did not present NiO as a precursor to the active phase but to a mixed zinc nickel oxide. Since the mesoporous characteristics of the material did not disappear, only two things can be concluded. According to the $H_2$-TPR diagrams, mixed oxide is not as easy to reduce as pure NiO, but the reduction temperature is also not excessively high. It can be inferred from this that the remaining phase is a likely ZnNi or an alloy of these two metals, which has no catalytic activity. The deactivation was almost immediate and with no signs of improvement. However, if longer tests were to be carried out, it is likely that the formation of a bimetallic carbide could result, which could improve activity.

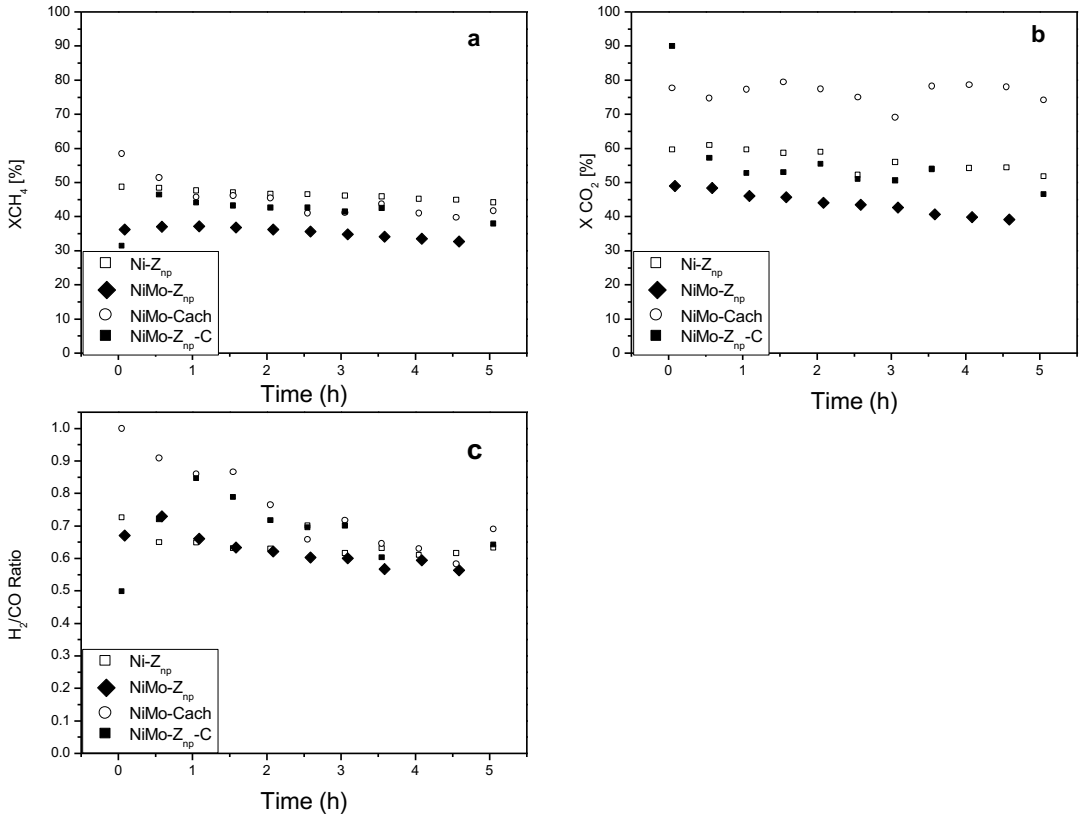


**Figure 28.** Catalytic conversion results for Ni-Mo materials. a) Methane conversions, b) $CO_2$ conversions, c) $H_2$/CO ratio. T= 700°C, P= 1 atm, GHSV= 57450 $cm^3\ g._{cat}^{-1}\ h^{-1}$

Mo-$Z_{np}$ and Mo-Cach materials contain zinc molybdate and molybdite (molybdenum oxide) as active phases, respectively. These formations were very difficult to reduce via $H_2$-TPR. At the reforming temperatures used in these studies (700 °C), the materials probably could not be reduced sufficiently to be able to have an active phase. The difficulty in reducing molybdene oxides is likely the reason why molybdenum carbide is almost always synthesized for use in DRM. The molybdenum carburization technique is more feasible than a reduction, since carbide synthesis temperatures have been reported to be achieved as of 700 $^oC$, depending on the carburizing agent [136]. In contrast, temperatures needed for reduction may be much higher.

As for catalysts that did have activity, the trend in the 4 materials to be more selective towards CO production than $H_2$ is of interest. However, it is interesting to note how the NiMo-$Z_{np}$ material produces a mixture with a ratio closer to 1 than the Ni-$Z_{np,}$ NiMo-Cach and NiMo-$Z_{np}$-C materials. As time went on, the relationship was reduced to values similar to those found for the other materials. The ratio closer to 1 is initially because NiMo-Znp contains ZnO, which by alkalinity effect can attract more $CO_2$. It is valid to assume that methane chemisorption decreased due to the alkalinity of the material. Ironically, the material that had deactivated the fastest was NiMo-$Z_{np}$, probably also due to nanoparticulate ZnO, which can sinter more easily than Cach.

Another peculiarity is that all materials convert less $CH_4$ and $CO_2$ than the best catalysts of the Ni-Pt group. Due to the presence of molybdenum in most of them, it is highly conclusive that the presence of molybdenum has acted in detriment of catalytic activity. The percentages are discussed below.

The Ni-$Z_{np}$ material began with methane conversions close to 50%, and after 4 hours these had decreased to only 44%. $CO_2$ conversions started at around 60% and declined to 54%. This was apparently the material with slowest deactivation.

Conversions for NiMo-$Z_{np}$ material started at 58% and 77% for $CH_4$ and $CO_2$, respectively. Methane conversions decreased to 43% after 4 hours. However, $CO_2$ conversion lessened at a lower rate, which explains why the $H_2$/CO ratio has lower values over time. It is highly likely that the carbon deposition was stronger in this material than in others, so that the methane chemisorption was at a disadvantage. Thus, formation of $H_2$ seemed to decrease.

The NiMo-Cach material had low but seemingly stable conversions. Methane conversions showed little change during the experiments (starting at 37% and ending at 33%), while $CO_2$ conversions started at around 50% and, after 4 hours, were at 40%. Thus, it is possible to assume that there is a preference for chemisorbing methane, which could be explained by a regenerating surface [72]. $H_2$-TPR analyses suggest that, at reaction temperatures, it is highly likely that a part of the metals has remained in an oxide state, which could contribute to the elimination of deposed carbon. The existence of these oxides could therefore influence a lower $CO_2$ chemisorption.

Finally, the NiMo-$Z_{np}$-C material has a low conversion, but similar to those mentioned above. Methane conversions start at around 46% and end at 38%, while $CO_2$ conversions start at 58% and end at 46%.

## 5.4 Chapter Conclusions

This round of materials was only studied for short periods. Ni-Mo materials were active, although they did not have the effectiveness of the materials presented in the Ni-Pt section. Much of the explanation for the regular activity of these catalysts lies in the difficulty in trying to reduce the oxides in the sample. Of all evaluated materials, 4 had catalytic activity. Two of the materials served to reaffirm results of the Ni-Pt study where ZnO was used.

The Ni-$Z_{np}$ material had some of the highest conversions, despite its low specific surface area. One thing that undoubtedly had a big effect on the effectiveness of the material was the property of the nanoparticulate ZnO. While it does not replace the effectiveness of a

mesoporous material, a nanoparticulate material will certainly allow for better particle dispersion, even if only achieved superficially.

For their part, the materials Ni-$Z_{np}$Cach and Ni-$Z_{np}$Cach2 were intended to combine alkalinity properties with mesopores, but they had low conversions, and had already deactivated after a few hours, without having achieved significant conversions of methane or $CO_2$. This agrees with NiPt-MgOCach (Ni-Pt series) material, which also failed to achieve significant conversions of methane or $CO_2$, even with the addition of platinum. This establishes that mesoporous silica and ZnO are not effective overall when used together, although using smaller amounts of ZnO could have the expected effect. These results are strongly at odds with MgO results in terms of alkalinity. Although they are alkaline materials, ZnO cannot work together with mesoporous silica at the levels used. It is likely that at the promoter level, ZnO can work better.

A combination of NiMo-$Z_{np}$ resulted in moderate conversions (45%) with a slow deactivation. NiMo-Cach was slightly more stable, and its $CO_2$ conversions are near 80%, which is one of the highest conversions achieved. Mo-$Z_{np}$ and Mo-Cach materials were materials impossible to reduce at reaction temperatures, so catalytic activity is zero for these materials with $MoO_3$. $H_2$-TPR reveals that temperatures above 900 $^oC$ are required before the reduction of these materials takes place. Thus, it is no surprise that these materials lacked catalytic activity. Moreover, the carburized material at 700 $^oC$, NiMo-$Z_{np}$-C, offers an important alternative to achieve catalytic activity in molybdenum materials.

The results for this section explain why a large majority of articles that use nickel and molybdenum together as active phases use the carburization process before starting DRM.

As could be seen in $H_2$-TPR results, these materials are more difficult to reduce than Ni-Pt materials.

Within the batch of Ni-Mo materials, the most difficult materials to reduce are those with only molybdenum as an active phase, although a fraction of molybdenum oxide was reducible at 550 $^{o}$C. Therefore, the Mo-$Z_{np}$ and Mo-Cach materials were two of the materials with less catalytic activity. Materials with nickel and molybdenum usually formed nickel molybdate, which were easier to reduce than molybdenum oxide species. The combination with nickel is highly likely to reduce the electronic density of molybdenum, which makes this type of compounds easier to reduce.

# Chapter 6:

# Carbon Studies on Spent Catalysts

## 6.1 Generalities pertaining to this chapter

a) Most of the analyses herein presented are Raman spectra of Ni-Pt series and Ni-Mo series.

b) The last study presented is a full characterization on both fresh and spent catalysts and does not include catalytic evaluation.

c) A comparison between weighed-out carbon deposits, XRD and Raman spectroscopy is offered.

## 6.2 Raman spectroscopy for Ni-Pt spent catalysts (short duration)

This section focuses only on a few catalysts. The Ni-Ald and NiPt-Ald materials are compared to each other, and NiPt-ZnOCach and Ni-ZnOAld-C materials are discussed.

The Ni-Ald material had little carbon content, due to the inert nature of the Ald material, which does not allow for longer contact time between the reactants and the catalyst. However, it is even more interesting to note that NiPt-Ald material does not contain carbon at all. Although it is also a bad catalyst, the absence of carbon-related peaks could be linked to the presence of platinum, which is a metal resistant to these formations.

As for NiPt-ZnOCach, this material was only evaluated for short-term periods, and had no activity whatsoever. However, the absence of carbon peaks is of great interest to virtually all laser exposures. This can be attributed only to the presence of ZnO, as the NiPt-Cach mix was effective. While the presence of this material results in loss of effectiveness of the Cach material, it apparently can prevent the appearance of carbon formations. However, the low surface area of this material could also have mean that there is little interaction with the reactant gases, which reduces the likelihood of finding carbon

formations. The absence of D, G and 2D peaks is common to all materials with ZnO. Figure 29 shows Raman spectra corresponding to spent samples with ZnO content.

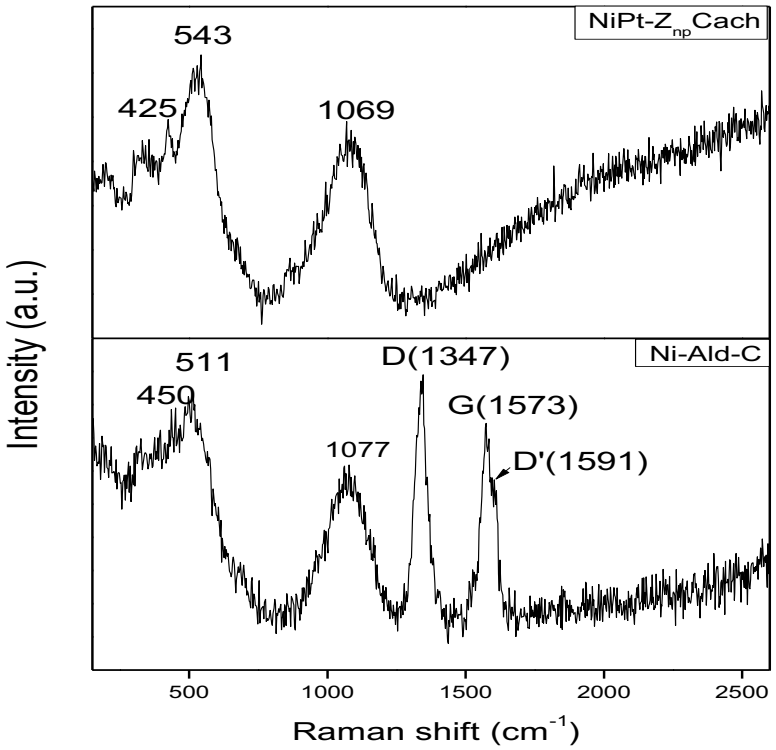


**Figure 29.** Two spent materials with ZnO content. Ni-Ald-C contained carbon prior to reaction.

In support of the feasibility of the elimination of deposed carbon, N-ZAld-C material had very little carbon, even though it was subjected to the carburization process. It is interesting to note that the spent material contains carbon in lower quantity and quality. This suggests that the material is effective in removing carbon deposits, probably due to the presence of ZnO. Prior to the reaction, carbon deposits are highly crystalline, while after the reaction they are more amorphous deposits. It also comes with a D' peak between 1596 and 1599 cm$^{-1}$, depending on the exposure in question. The D' peaks are related to graphene shores as well as graphene defects. This is not the only instance where a D' peak is detected in this thesis, as will be studied later.

Finally, the N-ZAld-C and N-MAld-C materials are the materials that were subjected to carburization, so they contain a lot of carbon. These contain ZnO and MgO, respectively. The spent N-ZAld-C material contains very low amounts of carbon, compared to the fresh carburized sample. This suggests that ZnO can eliminate amounts of carbon by retaining and partially disassembling $CO_2$ into CO and reactive oxygen, which can then react with carbon. This mechanism has been described in recent years [72]. The condensed pathways can also be found in figure 37 in Annex A. For its part, the spent N-MAld-C material also has carbon formations, although they have intensities similar to those that existed before the reaction, which are attributable only to the carburization process.

## 6.3 Raman spectroscopy for Ni-Pt spent catalysts (long-term)

Raman spectroscopy analysis for spent catalysts will be divided into two sections, one of which focuses specifically on catalysts supported on Cach and another for Ald-supported materials.

The Raman spectra for catalysts leaving the reaction system after long-term testing are presented in Figure 30, which shows the positions of peaks D, G and 2D, from left to right. The existence of these peaks suggests the presence of crystalline carbon structures and are a common feature in catalysts that use Cach as support. It was possible to find small differences between the spent samples, mostly in ratio of intensities ID/IG, as well as $I_{2D}/I_G$ (table 11).

**Table 11.** Intensity ratios $I_D/I_G$ and $I_{2D}/I_G$.

| **Material** | **$I_D/I_G$** | **$I_{2D}/I_G$** |
|---|---|---|
| Ni-Cach | 0.71 | 0.8 |
| NiPt-Cach | 0.66 | 0.91 |
| NiPt-MgOCach | 0.69 | 1.04 |
| Ni-Cach-C | 1.06 | 0.59 |

Ni-Cach, NiPt-Cach, and NiPt-MgOCach spent materials had a less intense D-band (as compared to the G band). This trend is reversed in Ni-Cach-C material, whereby the D-band is more intense than the G-band. This exhibition also highlights a D' peak, which along with the D-band involves the existence of carbon nanocrystalline structures, as well as layers and edges of defective graphene [137]. These qualities are typical of graphene nanowalls, which upon rolling are a component of nanotubes [138]. The D' peak found in the Ni-Cach-C material was also detected in the Ni-ZnOAld-C material (in short-term tests). These two materials were subjected to the carburization process before undergoing DRM.

In addition to the prevalence of 2D bands, the low values found for the $I_{2D}/I_G$ ratio suggest that these samples could be graphene multilayers [139]. D peaks were always present, although usually with lower intensities, except for Ni-Cach-C. D peaks contribute directly to determining the degree of disorder in carbon. Because the D-peak is related to disordered carbon, the $I_D/I_G$ ratio provides a measure of the degree of defects in carbon species [140]. Thus, the $I_D/I_G$ ratio suggests that NiPt-Cach was more successful in preventing the formation of disordered carbon deposits. As for Ni-Cach-C, this material had a higher amount of disordered carbon, probably due to the presence of high carbon content prior to DRM. This sample also had the least crystalline 2D band of all samples, which is a main feature in graphene. It should be reaffirmed that nickel carbide has previously been described as a possible precursor to graphene and nanotubes [122].

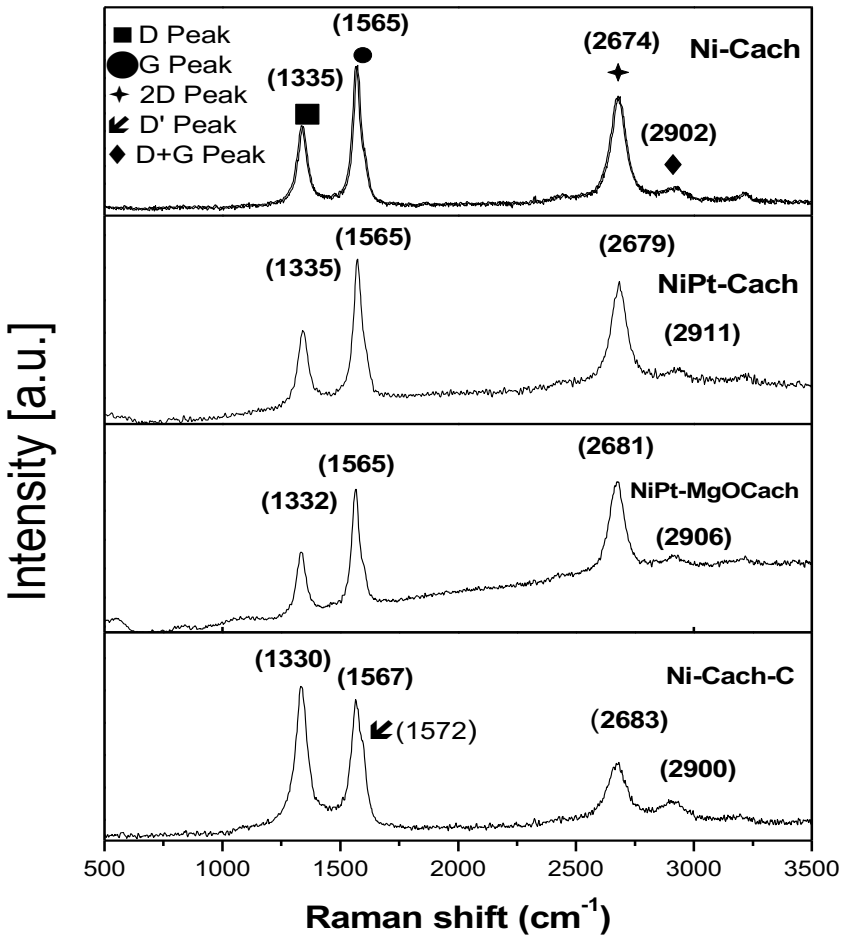


**Figure 30.** Raman spectra that correspond to spent Ni-Pt materials after long-term testing.

To complement this information, the absence of carbon peaks in materials supported on Ald is noteworthy. This correlates well with the low catalytic activity presented by these materials, as it practically confirms that there was no greater interaction between reactants and material. It could be argued that, due to the briefness of the experiments, there were no carbon formations. However, the materials supported on Cach and used in short-term testing came to show a full spectrum of carbon peaks. This information complements the idea of the existence of different deactivation mechanisms between materials with Ald and Cach.

Deactivation in materials with Ald silica is highly likely to be more related to sintering phenomena, rather than carbon deposition.

## 6.4 Raman spectroscopy for Ni-Mo spent catalysts

The results of these materials are of high interest, as the Raman spectra for this batch lacked peaks in general corresponding to carbon formations. However, it should be remembered that only short-term tests were performed, which had a maximum of 4 hours. These results are consistent with the Raman spectroscopy results of the series of materials presented in the previous section. The Raman spectra for this section are shown in Figure 31, although spectra for all materials are not shown.

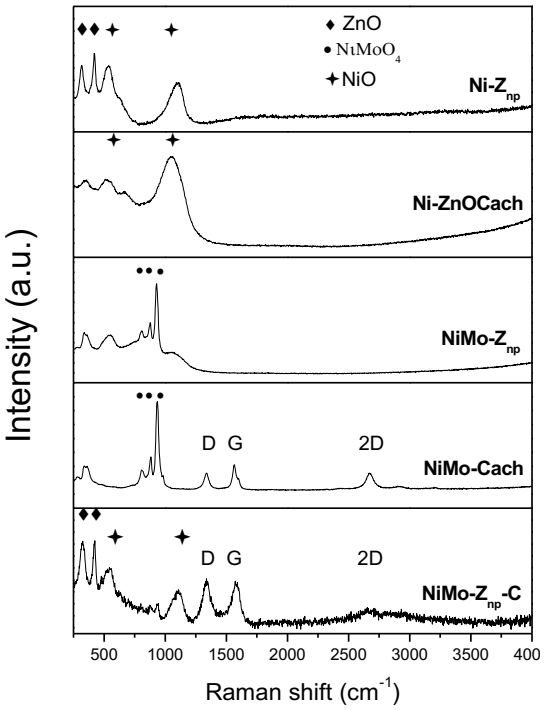


**Figure 31.** Raman spectra that correspond to Ni-Mo spent catalysts.

The reminder about argon scarcity is now important, which is why the other 3 materials were only in reaction for 1 hour. Therefore, no Raman tests were performed after DRM on these samples, as they would not have been comparable to those from 5-hour tests.

Firstly, materials Ni-$Z_{np}$, Ni-$Z_{np}$Cach and NiMo-$Z_n$ will be discussed. These materials have high percentages of ZnO. In the case of Ni-$Z_{np}$ and NiMo-$Z_{np}$, ZnO is the most prevalent material. However, the total absence of carbon deposit peaks is outstanding. It is interesting to note that there is a great contrast between the catalytic activity of Ni-$Z_{np}$ and NiMo-$Z_{np}$, as compared to Ni-$Z_{np}$Cach material. The Ni-$Z_{np}$Cach material had very low conversions in the 4-hour period, but there are no carbon formations to be found. This confirms suspicions about the deactivation process in the case of Ni-$Z_{np}$Cach, which does not have to do with sintering phenomena or catalytic surface poisoning, but with the lack of coupling between ZnO and mesoporous silica. This lack of coupling is probably related to a pore-blocking phenomenon following the addition of ZnO. Ni-$Z_{np}$ and NiMo-$Z_{np}$ materials, on the other hand, show slow deactivation, but it is more likely that they underwent sintering phenomena. The absence of carbon suggests that there is a mechanism for consumption of carbon, resulting in increased CO production.

NiMo-Cach is one of the materials with the highest presence of carbon, and it contrasts sharply with those discussed in the previous paragraph. The peaks corresponding to carbon formations are small compared to the other structures that appear in the spectrum. However, they are of similar intensity to the peaks that have discussed in section 6.3.

Material NiMo-$Z_{np}$-C contains peaks that correspond to carbon formations, albeit in low intensity. This is partly due to the presence of ZnO, but also to the fact that the molybdenum carbide phase was formed, as reported earlier in the XRD section. That is, the

carbon present in the spent sample is in the form of another compound, so the carbon peaks are of lower intensity.

## 6.5 Analysis of carbon formations for silica and Ni materials

A final study was devoted to characterizing carbon formations in $SiO_2$ and nickel materials, without performing a catalytic evaluation on these materials. The characterizations of XRD and Raman spectroscopy allowed for interesting correlations to be made regarding carbon formations, which were compared to physical carbon formations b weight. Similarly, information obtained in this study could be compared with that of some of the materials in section 3.3.1, although there were also discrepancies in the results obtained. The nomenclature used in this section is shown below (table 12).

**Table 12.** Nomenclature for materials used in this section.

| **Material** | **Composition** |
|---|---|
| Ni-Ald | Nickel/$SiO_2$-Ald |
| Ni-Cach | Nickel/$SiO_2$-Cach |
| Ni-SBA | Nickel/SBA-15 |

### 6.5.1 Characterizations on fresh materials

First, the elemental composition of the materials used in this section is shown (Table 13). The results were obtained with dispersive wave XRF.

**Table 13.** Composition results obtained via XRF for materials corresponding to carbon deposition studies.

| **Nomenclature** | **Ni** | **$SiO_2$** |
|---|---|---|
| Ni-SBA | 21.4 | 78.6 |
| Ni-Cach | 24.7 | 75.3 |
| Ni-Ald | 19.7 | 80.3 |

$N_2$-physisorption results again revealed large differences between the types of silica used. It should be remembered that this study also included SBA-15 as a support. The Ni-Ald and Ni-Cach materials maintain the same nomenclature that was assigned to them in the Ni-Pt catalyst section. The specific surface area reveals that the N-SBA matter has more than twice the Ni-Cach area, and more than 3 times the Ni-Ald material area. As for diameter pore, the Ni-Cach material has the smallest diameter of all. Although the pore diameter reveals that all materials are mesoporous in theory, the isotherms shown in Figure 32 demonstrate fundamental differences.

The Ni-SBA and Ni-Cach materials are mesoporous, although of a very different nature. The isotherms and hysteresis cycle of the N-SBA material reveal the existence of a highly ordered and uniform pore-sized material. The Ni-Cach material has a hysteresis cycle that is related to unorganized and non-uniform pore-sized materials. Meanwhile, the Ni-Ald material has isotherms that correspond to macroporous materials with $N_2$ adsorbed in multiple layers. The textural properties of these materials are shown in table 14.

**Table 14.** Textural properties of fresh pre-reaction materials.

| Assay | Specific surface area ($m^2/g$) | Pore diameter (nm) | Pore volume ($cm^3/g$) |
|---|---|---|---|
| Ni-Ald | 116.3 | 28.7 | 0.7 |
| Ni-SBA | 387 | 6.9 | 0.79 |
| Ni-Cach | 181.6 | 5.3 | 0.39 |

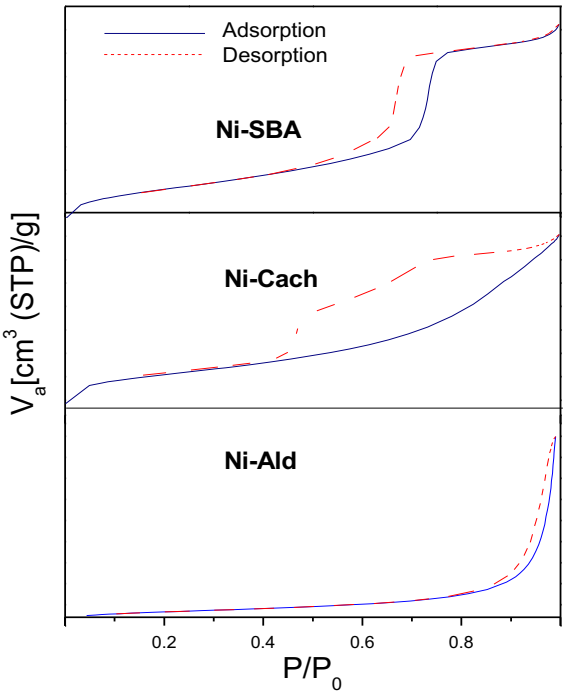


**Figure 32.** Adsorption and desorption isotherms in Nickel-silica materials.

$H_2$-TPR profiles showed significant variations between materials, which are shown in Figure 33. The highest hydrogen consumption peaks appeared at temperatures similar to those in study 3.3.1. In other words, the maximum hydrogen uptake occurred at temperatures between 366 and 376 °C. Thus, hydrogen consumption peaks were also visible at higher temperatures in the cases of Ni-Ald and Ni-Cach. In the case of Ni-SBA material, this peak appeared at 499 °C, whereas for Ni-Cach, the peak appeared at 545 °C, with two smaller peaks at higher temperatures. Secondary peaks in both mesoporous silicas suggest a great interaction between the support and the active phase. This interaction appears to be greater in the Ni-Cach material, as more peaks appear at higher temperatures. Due to the inert material quality of silica, these peaks are likely to have another explanation, such as an insertion of nickel particles within the $SiO_2$ framework. In addition, thanks to $N_2$ physisorption studies, it was concluded previously that there are different pore diameters. In

addition, the HR-TEM study reveals how there are smaller NiO particles than others, some of which can enter a fraction of the pores, where a phenomenon of encapsulation can certainly occur, thus increasing the interactions between support and the active phase. In this way it is possible to explain hydrogen consumption at different temperatures in a same material.

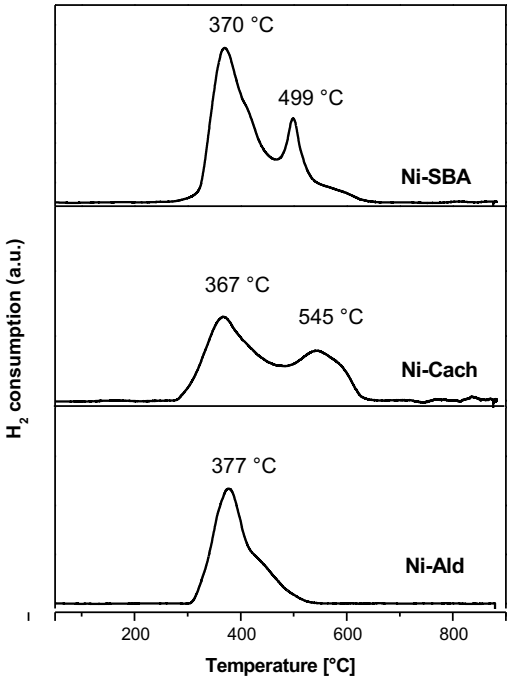


**Figure 33.** $H_2$-TPR profiles for silica and NiO materials.

## 6.5.2 Characterizations for spent materials

The results that correspond to spent catalysts are highly important, as there is a directly proportional relationship between heavy carbon deposits and spectrographic methods. The weight of the carbon deposits over time was reported in Figure 34, where the increase in the order Ni-SBA>Ni-Cach>Ni-Ald is easily distinguishable. It can be argued that the smaller crystal size for Ni in the Ni-Ald allowed less carbon deposition, as the

importance of particle size has been previously reported [66]. On the other hand, it has been previously concluded that Ald silica is an unsuitable support for DRM.

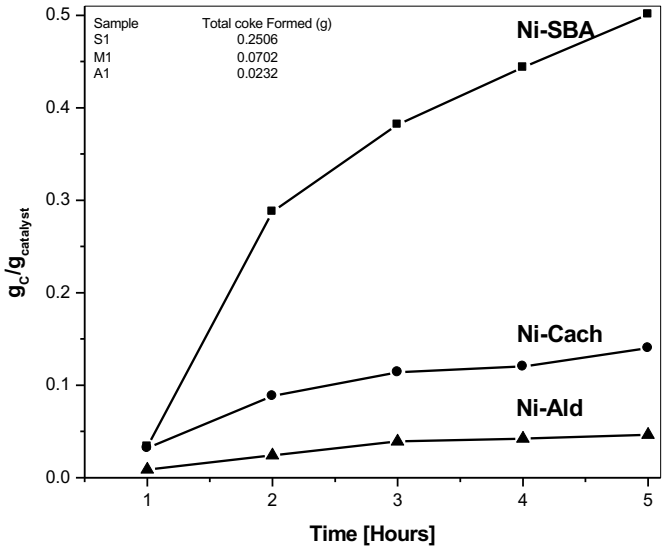


**Figure 34.** Physical monitoring results of carbon formations.

Regarding Ni-Cach material, although it is a highly active catalyst, carbon accumulated at a slower rate than in N-SBA. Because both materials have approximately the same crystal size (see table 15), this was not considered to be the cause of increased resistance to the formation of carbon deposits.

**Table 15.** Mean crystal size in spent materials.

| **Material** | **Crystal size (nm)** | |
|---|---|---|
| | **Carbon nanotubes (0 0 2)** | **Nickel (1 1 1)** |
| Ni-Ald | 5.6 | 24.7 |
| Ni-Cach | 6.1 | 36.1 |
| Ni-SBA | 6.5 | 37.0 |

The first observation that can be made is that, the larger specific surface area, the greater the amount of carbon deposited on the catalytic material as well. Although this can be considered valid for Ni-SBA and Ni-Cach materials, an explanation that is based solely on the area of area has disadvantages, as it has no valid basis in inert materials such as the material Ni-Ald.

The adsorption and desorption isotherms allowed for a more extensive explanation, as the hysteresis cycle in Ni-Cach materials reveals the existence of very varied pore diameters in catalyst, which in turn allows to increase an increase in the range corresponding to mesopores. The existence of a higher range of pore diameters generates an elongated hysteresis loop, extending down to the lowest relative pressures. Due to the large variation in pore diameters in the Ni-Cach material, it is possible that at least a fraction of the nickel is interacting strongly with the support, as can be seen in diagram $H_2$-TPR. However, adsorption and desorption isotherms can offer a very different perspective.

The hysteresis cycle of Ni-SBA reveals a highly ordered mesoporous material, with an order far higher than that of Ni-Cach. The N-SBA material is essentially a traditional mesoporous support. The high degree of organization offers a high specific surface area, which is much larger than that of any other material presented here. Thus, the existence of a higher metallic dispersion of nickel particles can be inferred. The existence of greater metal dispersion would theoretically render more active sites, so that better activity could be expected in the N-SBA catalyst. As a ordered material, it is also more likely that there will be less destruction of mesopores, whereby more stable catalytic activity can be expected. It has now been established that at the time when there is no contact between the active phase and the material, coke ceases to be produced. Therefore, if the Ni-SBA catalyst has a higher

order and surface area than the Ni-Cach material, it is to be expected that it will maintain a longer activity, in which carbon will also continue to be produced in greater quantity. Therefore, the carbon production rate is expected to be maintained for longer than in the other two materials. In turn, Ni-Cach will produce less carbon, as it is a disordered material that could lose activity quickly, at least in regions where there is a higher population of active phase.

The reduction with $H_2$ was a very valuable contribution, as it showed that there are fractions of NiO that are more difficult to reduce, indicating greater interactions between the support and the active phase. These interactions have previously been reported in carbon deposition studies. The highest reduction temperatures in the Ni-Cach material could be related to a scheme proposed by Wang *et al*. (2014),which suggests that CHO radical species be form in intermediate stages, prior to the dehydrogenation of methane [141]. Stronger interactions in this catalyst could be promoting this scheme, which allows for a decrease in carbon deposits and carbon consumption. The impact of dispersion on metal-support interactions has been previously studied, which presents an obstacle to sintering processes.

The results for the XRD patterns are shown in Figure 35. The 3 samples contain two phases that are easy to distinguish, which are metallic nickel and carbon nanotubes. The standard metallic nickel or nickel (PDF card 01-071-4654) has a cubic structure, with lattice parameters a=b=c=0.3525 nm. As for carbon nanotubes (PDF card 058-1638), the peak of graphite at 26 degrees 2is is the most notorious in all samples. The carbon nanotube diffraction pattern is a hexagonal lattice, with lattice parameters a=b=0.243 and c=0.687 nm. The angles that correspond to this lattice are α=β=90 °, y γ=120 °.

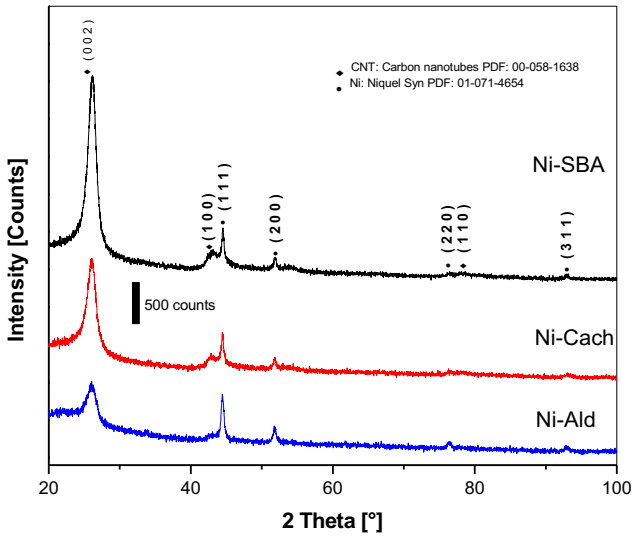


**Figure 35.** Diffraction patterns for spent Ni-$SiO_2$ materials.

The intensity of peaks between samples is varies, but they follow the same order of intensity with respect to carbon weighed-out deposits. This order is Ni-SBA>Ni-Cach>Ni-Ald. In the case of Ni-Cach material, it could initially be thought that, due to its higher metal nickel content, the material may have greater pore obstruction. This, in turn, could lead to larger carbon deposits. However, this was not the case.

Finally, Raman studies correlated very well with the results of XRD, as shown in figure 36. This sequence is repeated in the intensity of the carbon peaks, which is given in the order Ni-SBA>Ni-Cach>Ni-Ald. Regardless of the materials used, the D-peaks were always higher intensity than the G-peaks, which means that the detected carbon formations are highly disordered structures.

This is at odds with the experiments carried out in section 4.3.3, where most spent catalysts had a more intense G-peak. This discrepancy can be explained in the how the experiment in question was conducted. As mentioned above, the reaction was stopped every

60 minutes to weigh the increase in reactor weight, after which DRM was started again. This type of experiment could be inducing disorder in carbon layers due to each cooling stage between weight-monitoring times.

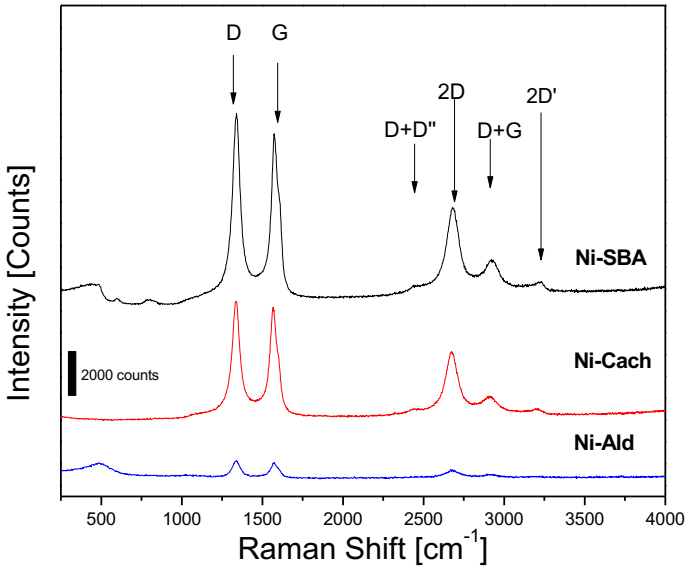


**Figure 36.** Raman spectra corresponding to Ni and silica spent materials. The easiest patterns to visualize correspond to carbon interactions.

## 6.6 Chapter Conclusions

Carbon formation studies enabled the study of important correlations between Raman spectroscopy, XRD and physical monitoring of carbon. In all three cases, the nickel supported on the commercial silica Ald generated lower amounts of carbon, followed by the Ni-Cach material. The material with the highest amount of carbon was N-SBA. In the case of XRD and Raman spectroscopy, the peak intensity was increasing, while in physical monitoring it was the mass that increased. From here it can be inferred that any of the 3 methods to carry out carbon deposit monitoring are completely reliable when trying to

estimate carbon formations. However, Raman diffraction and spectroscopy methods come to provide much more information about the type of carbon in question, as well as its quality. When comparing between mesoporous materials (Ni-Cach and Ni-Ald), it is highly likely that the amount of carbon deposits formed is depending on the surface area.

Finally, the types of carbon formations are mostly highly disordered carbon nanotubes. The Ratio $I_D/I_G$ was greater than 1 in all cases in Raman spectroscopy. This relationship is at odds with most Raman analyses on spent samples, where the ratio was less than 1. The few cases in which carbon formations had an $I_D/I_G$ ratio greater than 1 occurred when the samples contained carbon before DRM, due to the carburization process. The samples used to compare the Ni-Ald, Ni-Cach and Ni-SBA study were not carburized, so it is determined that the ratio greater than 1 was due to a disorder caused by disassembling the equipment at the end of each hour.

# Chapter 8:

# Conclusions and Future Research

First and foremost, it can be stated with confidence that the proposed hypothesis proved to be true. It is possible to carry out dry reforming over extended time periods and at temperatures below 800 °C over Ni and $SiO_2$-based materials without deactivation of catalytic materials. A set of catalysts with high activity for DRM was synthesized, which were supported on mesoporous silica Cach. The initial activity of these materials is around 90% initially, showing deactivation due to slow carbon deposition. Ni, Ni-Pt, Ni-Pt-MgO and $Ni_3C$ using Cach as a support remained active for at least 30 h. Interestingly, the carburization process used for creating $Ni_3C$ resulted in modification of the syngas composition, favoring formation of CO. On the other hand, materials supported on nanoparticulate silica had very low activity and deactivated quickly. Many types of carbon deposits were detected on these spent materials, including carbon nanotubes and graphene.

The batch of materials with Ni-Mo was not particularly effective for catalytic purposes, but provided interesting and complementary information, mainly for carbon deposit studies. Catalytic evaluations on these materials were unfortunately too brief to provide conclusive evidence. However, use of nanoparticulate ZnO as a support resulted in moderate conversions, as long as it was not used in conjunction with Cach. Lower conversion values for Ni-Mo materials is likely related to difficulty in reducing molybdenum oxides. It is interesting to note that the presence of ZnO results in virtually no detectable carbon formations by use of Raman spectroscopy.

Carbon deposits for materials containing only Ni-$SiO_2$ confirmed the existence of a correlation between the physical formation of carbon and XRD and Raman spectroscopy results, as observed in peak intensity. The correlation could be linked to both specific surface area and catalytic activity.

## Future Research

In conclusion, it should be recognized that great progress was made in the topics of synthesis, study and application of catalysts for DRM. This topic is certainly a new area of exploration in the IIIER, and the new findings reported herein are expected to direct the materials area to finding better catalysts and new options in characterization. There are many unknowns that need to be explored and solved in future work. These involve the study of mesoporous materials and little-used supports up to now for DRM, such as nanoparticulate ZnO. Some of the alloys or compounds formed during this thesis have only recently been reported in scientific journals, and remain an opportunity for research that could still make both IIIER and IPN-Zacatenco pioneers in this area of research.

These studies should involve carbon deposit removal mechanisms and the study of solid solutions, as well as more advanced characterization techniques, such as X-Ray photoelectron spectroscopy, as well as more exploration via transmission microscopy. Also, exploration of upstream technology is highly recommended, in the hope that a suitable biogas source for DRM can be developed on site or in collaboration with a company or farming communities.

# Chapter 9:
# References

[1] M. Pacesila, S. G. Burcea & S. E. Colesca, «Analysis of renewable energies in European Union,» *Renewable and Sustainable Energy Reviews,* vol. 56, 156-170, 2016.

[2] B. Beloff, «Lessons from the DeepWater Horizon debacle: a precautionary tale,» *Clean Technologies and Environmental Policy,* vol. 12, 331-333, 2010.

[3] R. W. Howarth, A. Ingraffea & T. Engelder, «Natural gas: Should fracking stop?,» *Nature,* vol. 477, 271-275, 2011.

[4] R. Tremblay, «In Iraq and Syria, A Vietnam-type Quagmire Over Oil and Gas?,» *Global Research,* 2014.

[5] B. Taub, «The New Yorker,» 2015. [Online]. Available: https://www.newyorker.com/news/news-desk/the-isis-oil-trade-from-the-ground-up. [Last access: 2019].

[6] T. Plümper & E. Neumayer, «The Unequal Burden of War: The Effect of Armed Conflict on the Gender Gap in Life Expectancy,» *International Organization,* vol. 60, 723-754, 2006.

[7] Y. Matsumura, « Stabilization of $Cu/ZnO/ZrO_2$ catalyst for methanol steam reforming to hydrogen by coprecipitation on zirconia support,» *Journal of Power Sources,* vol. 209, 109-116, 2013.

[8] M. V. Tsodikov, A. S. Fedotov, D. O. Antonov, V. I. Uvarov, V. Y. Bychkov & F. C. Luck, «Hydrogen and syngas production by dry reforming of fermentation products on porous ceramic membrane-catalytic converters,» *International Journal of Hydrogen Energy,* vol. 41, 2424-2431, 2016.

[9] D. J. Moon, «Hydrogen Production by Catalytic Reforming of Gaseous Hydrocarbons (Methane & LPG),» *Cataly Surv Asia,* vol. 12, 188-202, 2008.

[10] D. R. Lide, «Handbook of Chemistry and Physics,» *CRC Press,* vol. 85, 2004.

[11] J. M. Lavoie, «Review on dry reforming of methane, a potentially more environmentally-friendly approach to the increasing natural gas exploitation,» *Frontiers in Chemistry,* vol. 2, 1-17, 2014.

[12] R. Rauch, J. Hrbek & H. Hofbauer, «Biomass gasification for synthesis gas production and applications of the syngas,» *Wiley Interdisciplinary Reviews: Energy and Environment,* vol. 3, 343-362, 2014.

[13] S. Califano, Pathways to Modern Chemical Physics, Berlin Heidelberg: Springer-Verlag, 2012.

[14] N. I. Kokarev, A. S. Kozlov, S. I. Pechenkin, V. Y. Dzyuzer, A. A. Tsukanov & M. A. Gromkova, «Use of reformed natural gas for heating glass furnaces,» *Glass and Ceramics,* vol. 32, 14-16, 1975.

[15] H. J. Alves, C. Bley Junior, R. R. Niklevicz, E. P. Frigo, M. S. Frigo y C. H. Coimbra-Araújo, «Overview of hydrogen production technologies from biogas and the applications in fuel cells,» *International Journal of Hydrogen Energy,* vol. 38, 5215-5225, 2013.

[16] G. Iaquaniello, E. Antonetti, B. Cucchiella, E. Palo, A. Salladini, A. Guarinoni, A. Lainati & L. Basini, «Natural Gas Catalytic Partial Oxidation: A Way to Syngas and Bulk Chemicals Production,» de *Natural Gas - Extraction to End Use*, InTechOpen, 2012, 267-286.

[17] S. Al Arni, B. Bosio & E. Arato, «Syngas from sugarcane pyrolysis: An experimental study for fuel cell applications,» *Renewable Energy,* vol. 35, 29-35, 2010.

[18] B. V. Babu, «Biomasspyrolysis: a state-of-the-art review,» *Biofuels, Bioproducts and Biorefining,* vol. 2, 393-414, 2008.

[19] H. Balat & E. Kirtay, «Hydrogen from biomass - Present scenario and future prospects,» *International Journal of Hydrogen Energy,* vol. 35, 7416-7426, 2010.

[20] R. Goswami, P. Chattopadhyay, A. Shome, S. N. Banerjee, A. K. Chakraborty, A. K. Mathew & S. Chaudhury, «An overview of physico-chemical mechanisms of biogas production by microbial communities: a step towards sustainable waste management,» *3 Biotech,* vol. 6, 72, 2016.

[21] S. Sangsong, M. Phongaksorn, S. Tungkamani, T. Sornchamni & R. Chuvaree, «Dry Methane Reforming Performance of Ni-based Catalyst Coated onto Stainless Steel Substrate,» *Energy Procedia,* vol. 79, 137-142, 2015.

[22] «Encyclopedia Britannica,» 2018. [En línea]. [Last access: december 2019].

[23] C. M. Kalamaras & A. M. Efstathiou, «Conference Papers in Energy,» *Hydrogen Production Technologies: Current State and Future Developments,* vol. 3, 1-9, 2013.

[24] B. Albrecht, «Reactor Modeling and Process Analysis for Partial Oxidation of Natural Gas,» University of Twente, 2004.

[25] X. Zhao, B. Joseph, J. Kuhn & S. Ozcan, «Biogas Reforming to Syngas: A Review,» *iScience,* vol. 23, p. 101082, 2020.

[26] S. A. Al-Sayari, «Recent Developments in the Partial Oxidation of Methane to Syngas,» *The Open Catalysis Journal,* vol. 6, 17-28, 2013.

[27] E. Mancusi, L. Acampora, F. S. Marra & P. Altimarri, «Hysteresis in autothermal methane reforming over Rh catalysts: Bifurcation analysis,» *Chemical Engineering Journal,* vol. 262, 1052-1064, 2015.

[28] M.-P. Lai, W.-H. Lai, R.-F. Horng, C.-Y. Chen, W.-C. Chiu, S.-S. Su & Y.-M. Chang, «Experimental study on the performance of oxidative dry reforming from simulated gas,» *Energy Procedia,* vol. 29, 225-233, 2012.

[29] G. Eigenberger & R. Wilhelm, Ullmann's Encyclopedia of Industrial Chemistry || Catalytic Fixed-Bed Reactors, Weinheim: Wiley-VCH Verlag GmbH & Co. KGaA, 2000.

[30] K. Sutthiumporn & S. Kawi, «Promotional effect of alkaline earth over Ni–$La_2O_3$ catalyst for $CO_2$ reforming of $CH_4$: Role of surface oxygen species on $H_2$ production and carbon suppression,» *International Journal of Hydrogen Energy,* vol. 36, 14435-14446, 2011.

[31] Ş. Özkara-Aydınoğlu, E. Özensoy & A. E. Aksoylu, «The effect of impregnation strategy on methane dry reforming activity of Ce promoted Pt/$ZrO_2$,» *International Journal of Hydrogen Energy,* vol. 24, 9711—9722, 2009.

[32] A. I. Tsyganok, T. Tsunoda, S. Hamakawa, K. Suzuki, K. Takehira & T. Hayakawa, «Dry reforming of methane over catalysts derived from nickel-containing Mg–Al layered double hydroxides,» *Journal of Catalysis,* vol. 213, 191-203, 2003.

[33] P. Ferreira-Aparicio, I. Rodriguez-Ramos, J. A. Anderson & A. Guerrero-Ruiz, «Mechanistic aspects of the dry reforming of methane over ruthenium catalysts,» *Applied Catalysis A: General,* vol. 202, 183-196, 2000.

[34] J. P. Richardson, Principles of Catalyst Development, New York: Plenum Press, 1989.

[35] O. W. Perez-Lopez, A. Senger, N. R. Marcilio & M. A. Lansarin, «Effect of composition and thermal pretreatment on properties of Ni–Mg–Al catalysts for $CO_2$ reforming of methane,» *Applied Catalysis A: General,* vol. 303, 234-244, 2006.

[36] E. Dahdah, J. Abou Rached, S. Aouad, C. Gennequin, H. L. Tidahy, J. Estephane, A. Aboukais & E. Abi Aad, «$CO_2$ reforming of methane over NixMg6−x$Al_2$ catalysts: Effect of lanthanum doping on catalytic activity and stability,» *International Journal of Hydrogen Energy,* vol. 42, 12808-12817, 2017.

[37] E. Ruckenstein & Y. H. Hu, «Role of Support in $CO_2$ Reforming of $CH_4$ to Syngas over Ni Catalysts,» *Journal of Catalysis,* vol. 162, 230-238, 1996.

[38] Y. Vafaeian, H. Mohammad & A. Soghand, «Ultrasound assisted dispersion of different amount of Ni over ZSM-5 used as nanostructured catalyst for hydrogen production via $CO_2$ reforming of methane,» *Energy Conversion and Management,* vol. 76, 1093-1103, 2013.

[39] M. Usman, W. M. Wan Daud & H. F. Abbas, «Dry reforming of methane: Influence of process parameters—A review,» *Renewable and Sustainable Energy Reviews,* vol. 45, 710-744, 2015.

[40] S. Therdthianwong, C. Siangchin & A. Therdthianwong, «Improvement of coke resistance of Ni/al2O4 catalyst in $CH_4$/$CO_2$ reforming by $ZrO_2$ addition,» *Fuel Processing Techology,* vol. 89, 160-168, 2008.

[41] C. H. Bartholomew, «Mechanisms of catalyst deactivation,» *Applied Catalysis A: General,* vol. 212, 17-60, 2001.

[42] O. Bezkrovnyi, P. Kraszkiewicz, I. Krivtsov, J. Quesada, S. Ordoñez & L. Kepinsky, «Thermally induced sintering and redispersion of Au nanoparticles supported on $Ce_{1-x}Eu_xO_2$ nanocubes and their influence on catalytic CO oxidation,» *Catalysis Communications,* vol. 131, 2019.

[43] T. W. Hansen, A. T. DeLaRiva, S. R. Challa & A. K. Datye, «Sintering of Catalytic Nanoparticles: Particle Migration or Ostwald Ripening?,» *ACS Publications,* vol. 46, 1720-1730, 2013.

[44] S. Cimino & L. Lisi, «Catalyst Deactivation, Poisoning and Regeneration,» *Catalysts,* vol. 9, 668, 2019.

[45] P. L. Benito, A. G. Gayubp, A. T. Aguayo, M. Olazar & J. Bilbao, «Deposition and Characteristics of Coke over a H-ZSM5 Zeolite-Based Catalyst in the MTG Process,» *Ind. Eng. Chem. Res.,* vol. 35, 3991-3998, 1996.

[46] C. H. Bartholomew, «Carbon Deposition in Steam Reforming and Methanation,» *Catalysis Reviews,* vol. 24, 67-112, 1982.

[47] L. A. Arkatova, «The deposition of coke during carbon dioxide reforming of methane over intermetallides,» *Catalysis Today,* vol. 157, 170-176, 2010.

[48] C. J. Liu, J. Ye, J. Jiang & Y. Pan, «Progresses in the Preparation of Coke Resistant Ni-based Catalyst for Steam and $CO_2$ Reforming of Methane,» *ChemCatChem,* vol. 3, 529-541, 2011.

[49] K. Jabbour, N. El Hassan, S. Casale, J. Estephane & H. El Zakhem, «Promotional effect of Ru on the activity and stability of Co/SBA-15 catalysts in dry reforming of methane,» *International Journal of Hydrogen Energy,* vol. 39, 7780-7787, 2014.

[50] Y. M. Zhorov & L. A. Ostrer, «Coke deposition and deactivation of catalysts,» *Chemistry and Technology of Fuels and Oils,* vol. 26, 226-229, 1990.

[51] Y. H. Hu & E. Ruckenstein, «Catalytic Conversion of Methane to Synthesis Gas by Partial Oxidation and $CO_2$ Reforming,» *Advances in Catalysis,* vol. 48, 297-345, 2004.

[52] Y. Lou, M. Steib, Q. Zhang, K. Tiefenbacher, A. Horváth, A. Jentys, Y. Liu & J. A. Lercher, «Design of stable Ni/$ZrO_2$ catalysts for dry reforming of methane,» *Journal of Catalysis,* vol. 356, 147-156, 2017.

[53] S. S. Itkulova, G. D. Zakumbaeva, Y. Y. Nurmakanov, A. A. Mukazhanova & A. K. Yermaganbetova, «Syngas production by bireforming of methane over Co-based alumina-supported catalysts,» *Catalysis Today,* vol. 228, 194-198, 2014.

[54] C. H. Collett & J. McGregor, «Things go better with coke: the beneficial role of carbonaceous deposits in heterogeneous catalysis,» *Catalysis Science & Technology,* Vol. 6, 363-378, 6, 2016.

[55] E. Tracz, R. Scholz & T. Borowiecki, «High-resolution electron microscopy study of the carbon deposit morphology on nickel catalysts,» *Applied Catalysis,* vol. 66, 133-147, 1990.

[56] J. M. Ginsburg, J. Piña, T. El Solh & H. I. de Lasa, «Coke Formation over a Nickel Catalyst under Methane Dry Reforming Conditions: Thermodynamic and Kinetic Models,» *Industrial & Engineering Chemistry Research,* vol. 44, 4846-4854, 2005.

[57] L. Guczi, G. Stefler, O. Geszti, I. Sajó, Z. Pászti, A. Tompos & Z. Schay, «Methane dry reforming with $CO_2$: A study on surface carbon species,» *Applied Catalysis A: General,* vol. 375, 236-246, 2010.

[58] N. D. Charisiou, G. Siakavelas, L. Tzounis, V. Sebastian, A. Monzon, M. A. Baker, S. J. Hinder, K. Polychronopoulou, I. V. Yentekakis & M. A. Goula, «An in depth investigation of deactivation through carbon formation during the biogas dry reforming reaction for Ni supported on modified with $CeO_2$ and $La_2O_3$ zirconia catalysts,» *International Journal of Hydrogen Energy,* vol. 43, 18955-18976, 2018.

[59] L. Qian, Z. Ma, Y. Ren, H. Shi, B. Yue, S. Feng, J. Shen & S. Xie, «Investigation of La promotion mechanism on Ni/SBA-15 catalysts in CH4 reforming with $CO_2$,» *Fuel,* vol. 122, 47-53, 2014.

[60] M. Kogler, E. M. Köck, L. Perfler, T. Bielz, M. Stöger-Pollach, W. Hetaba, M. Willinger, X. Huang, M. Schuster, B. Klötzer & S. Penner, «Methane Decomposition and Carbon Growth on $Y_2O_3$, Ytria-Stabilized Zirconia, and $ZrO_2$,» *Chemistry of Materials,* vol. 26, 1690-1701, 2014.

[61] D. C. Carvalho, H. S. de Souza, J. M. Filho, A. C. Oliveira, A. Campos, E. R. Milet, F. F. de Sousa, E. Padron-Hernandez & A. C. Oliveira, «A study on the modification of mesoporous mixed oxides supports for dry reforming of methane by Pt or Ru,» *Applied Catalysis A: General,* vol. 473, 132-145, 2014.

[62] N. A. Aramouni, J. Zeaiter, W. Kwapinski & M. N. Ahmad, «Thermodynamic analysis of methane dry reforming: Effect of the catalyst particle size on carbon formation,» *Energy Conversion and Management,* vol. 150, 614-622, 2017.

[63] S. Sokolov, E. V. Kondratenko, M. M. Pohl, A. Barkschat & U. Rodemerck, «Stable low-temperature dry reforming of methane over mesoporous $La_2O_3$-$ZrO_2$ supported Ni catalyst,» *Applied Catalysis B: Environmental,* Vol. 113-114, 19-30, 2012.

[64] T. P. Braga, R. C. Santos, B. Sales, B. R. da Silva, A. N. Pinheiro, E. R. Leite & A. Valentini, «$CO_2$ mitigation by carbon nanotube formation during dry reforming of methane analyzed by factorial design combined with response surface methodology,» *Chinese Journal of Catalysis,* vol. 35, 514–523, 2014.

[65] J. Károlyi, M. Németh, C. Evangelisti, G. Sáfran, Z. Schay, A. Horváth & F. Somodi, «Carbon dioxide reforming of methane over Ni–In/SiO 2 catalyst without coke formation,» *Journal of Industrial & Engineering Chemistry,* vol. 58, 189-201, 2017.

[66] V. Y. Bychkov, Y. P. Tyulenin, A. A. Firsova, E. A. Shafranovsky, A. Y. Gorenberg & V. N. Korchak, «Carbonization of nickel catalysts and its effect on methane dry reforming,» *Applied Catalysis A: General,* vol. 453, 71-79, 2013.

[67] I. Alstrup, «A New Model Explaining Carbon Filament Growth on Nickel, Iron, and Ni-Cu Alloy Catalysts,» *Journal of Catalysis,* vol. 109, 241-251, 1988.

[68] J. Dou, R. Zhang, X. Hao, Z. Bao, T. Wu, B. Wang & F. Yu, «Sandwiched $SiO_2$@Ni@$ZrO_2$ as a Coke Resistant Nanocatalyst for Dry Reforming of Methane,» *Applied Catalysis B: Environmental,* vol. 254, 2019.

[69] P. Djinović, I. G. O. Črnivec & A. Pintar, «Biogas to syngas conversion without carbonaceous deposits via the dry reforming reaction using transition metal catalysts,» *Catalysis Today,* vol. 253, 155-162, 2015.

[70] J. M. Smith, H. C. Van Ness & M. M. Abbott, Introducción a la Termodinámica en Ingeniería Química, México, D.F. : McGraw-Hill/Interamericana Editores, 1997.

[71] J. G. Roblero, F. Pola-Albores, M. A. Valenzuela, E. Rojas-García, E. Ríos-Valdovinos & G. Valverde-Aguilar, «Ni and $Ni_3C$ catalysts supported on mesoporous silica for dry

reforming of methane,» *International Journal of Hydrogen Energy,* vol. 44, 10473-10483, 2019.

[72] Z. Bian, S. Das, M. H. Wai, P. Hongmanorom & S. Kawi, «A review on bimetallic Ni-Based catalysts for $CO_2$ reforming of methane,» *ChemPhysChem,* vol. 18, 3117-3134, 2017.

[73] J. H. Kim, D. J. Suh, T. J. Park & K. L. Kim, «Effect of metal particle size on coking during $CO_2$ reforming of $CH_4$ over Ni–alumina aerogel catalysts,» *Applied Catalysis A: General ,* vol. 197, 191-200, 2000.

[74] J. P. Pradier & C. M. Pradier, Carbon Dioxide Chemistry. Environmental Issues, Cambridge: Royal Society of Chemistry, 1994.

[75] S. Teuner, P. Neumann & F. von Linde, «The Calcor Standard and Calcor Economy Processes,» *OIL Gas European Magazine,* vol. 27, 44-46, 2001.

[76] D. Schuetzle, G. Tamblyn, M. Caldwell & R. Schuetzle, «Solar Reforming of Carbon Dioxide to Produce Diesel Fuel,» 2010.

[77] J. Kempf, «Process Worldwide,» 2015. [Online]. Available: www.process-worldwide.com/official-opening-of-linde-pilot-reformer-in-germany-a-508100/. [Last access: 2019].

[78] M. R. Riazi & D. Chiaramonti, Biofuels Production and Processing Technology, Boca Raton: CRC Press Taylor & Francis Group, 2018.

[79] E. Ruckenstein & Y. H. Hu, «Carbon dioxide reforming of methane over nickel/alkaline earth metal oxide catalysts,» *Applied Catalysis A: General,* vol. 133, 149-161, 1995.

[80] A. Shamsi, «Partial Oxidation and Dry Reforming of Methane Over Ca/Ni/K(Na) Catalysts,» *Catalysis Letters,* vol. 109, 189-193, 2006.

[81] Z. Alipour, M. Rezaei & F. Meshkani, «Effect of Ni loadings on the activity and coke formation of MgO-modified $Ni/Al_2O_3$ nanocatalyst in dry reforming of methane,» *Journal of Energy Chemistry,* vol. 23, 633—638, 2014.

[82] E. Ruckenstein & Y. H. Hu, «The effect of precursor and preparation conditions of MgO on the $CO_2$ reforming of $CH_4$ over NiO/MgO catalysts,» *Applied Catalysis A: General,* vol. 154, 185-205, 1997.

[83] M. J. Mosquera, D. M. de los Santos, L. Valdez-Castro y L. Esquivias, «New route for producing crack-free xerogels: Obtaining uniform pore size,» *Journal of Non-Crystalline Solids,* vol. 354, 645-654, 2008.

[84] Z. Jiang, X. Liao & Y. Zhao, «Comparative study of the dry reforming of methane on fluidised aerogel and xerogel $Ni/Al_2O_3$ catalysts,» *Applied Petrochemical Research,* vol. 2013, 91-99, 2013.

[85] B. Q. Xu, J. M. Wei, Y. T. Yu, J. L. Li & Q. M. Zhu, «Carbon Dioxide Reforming of Methane Over Nanocomposite $Ni/ZrO_2$ Catalysts,» *Topics in Catalysis,* vol. 22, 77-85, 2003.

[86] H. Arbag, S. Yasyerli, N. Yasyerli, T. Dogu & G. Dogu, «Coke Minimization in Dry Reforming of Methane by Ni Based Mesoporous Alumina Catalysts Synthesized Following Different Routes: Effects of W and Mg,» *Topics in Catalysis,* vol. 56, 18-20, 2013.

[87] D. C. LaMont & W. J. Thomson, «The influence of mass transfer conditions on the stability of molybdenum carbide for dry methane reforming,» *Applied Catalysis A: General,* vol. 274, 173-178, 2004.

[88] A. R. Darujati & W. J. Thomson, «Stability of supported and promoted-molybdenum carbide catalysts in dry-methane reforming,» *Applied Catalysis A: General,* vol. 296, 139-147, 2005.

[89] A. J. Brungs, A. P. York & M. L. Green, «Comparison of the group V and VI transition metal carbides for methane dry reforming and thermodynamic prediction of their relative stabilities,» *Catalysis Letters,* vol. 57, 65-69, 1999.

[90] A. J. Brungs, A. P. York, J. B. Claridge, C. Márquez-Álvarez & M. L. Green, «Dry reforming of methane to synthesis gas over supported molybdenum carbide catalysts,» *Catalysis Letters,* vol. 70, 117-122, 2000.

[91] T. Hirose, Y. Ozawa & M. Nagai, «Preparation of a Nickel Molybdenum Carbide Catalyst and Its Activity in the Dry Reforming of Methane,» *Chinese Journal of Catalysis,* vol. 32, 771-776, 2011.

[92] S. Li & J. Gong, «Strategies for improving the performance and stability of Ni-based catalysts for reforming reactions,» *Chemical Society Reviews,* vol. 43, 7245-7256, 2014.

[93] T. Xie, L. Shi, J. Zhang & D. Zhang, «Immobilizing Ni nanoparticles to mesoporous silica with size and location control via a polyol-assisted route for coking- and sintering-resistant dry reforming of methane,» *Chemical Communications,* vol. 50, 7250-7253, 2014.

[94] D. Kang, H. S. Lim & J. W. Lee, «Enhanced catalytic activity of methane dry reforming by the confinement of Ni nanoparticles into mesoporous silica,» *International Journal of Hydrogen Energy,* vol. 42, 1-13, 2017.

[95] X. Gao, H. Liu, K. Hidajat & S. Kawi, «Anti-Coking Ni/$SiO_2$ Catalyst for Dry Reforming of Methane: Role of Oleylamine/Oleic Acid Organic Pair,» *ChemCatChem,* vol. 7, 4188-4196, 2015.

[96] F. Huang, R. Wang, C. Yang, H. Driss, W. Chu & H. Zhang, «Catalytic performances of Ni/mesoporous $SiO_2$ catalysts for dry reforming of methane to hydrogen,» *Journal of Energy Chemistry,* vol. 25, 709-719, 2016.

[97] U. d. Grenada, «Departamento de Edafología y Química Agrícola,» [Online]. Available: http://edafologia.ugr.es/imaginter/arcillas/arcillas.htm. [Last access: 2019].

[98] S. Das, J. Ashok, Z. Bian, N. Dewangan, M. H. Wai, Y. Du, A. Borgna, K. Hidajat & S. Kawi, «Silica - Ceria sandwiched Ni core-shell catalyst for low temperature Dry Reforming of Biogas: Coke resistance and Mechanistic insights,» *Applied Catalysis B: Environmental,* vol. 30, 220-236, 2018.

[99] Z. Li & S. Kawi, «Facile Synthesis of Multi-Ni-Core@Ni Phyllosilicate@$CeO_2$ Shell Hollow Spheres with High Oxygen Vacancy Concentration for Dry Reforming of $CH_4$,» *ChemCatChem,* vol. 10, 2994-3001, 2018.

[100] Z. Li & S. Kawi, «Multi-Ni@Ni phyllosilicate hollow sphere for $CO_2$ reforming of $CH_4$: influence of Ni precursors on structure, sintering and carbon resistance,» *Catalysis Science & Technology,* vol. 8, 1915-1922, 2018.

[101] Z. Li, B. Jiang, Z. Wang & S. Kawi, «High carbon resistant Ni@Ni phyllosilicate@$SiO_2$ core shell hollow sphere catalysts for low temperature $CH_4$ dry reforming,» *Journal of $CO_2$ Utilization,* vol. 27, 238-246, 2018.

[102] Z. Li, M. Liuye, Y. Kathiraser & S. Kawi, « Yolk–Satellite–Shell Structured Ni–Yolk@Ni@$SiO_2$ Nanocomposite: Superb Catalyst toward Methane $CO_2$ Reforming Reaction,» *ACS Catalysis,* vol. 4, 1526-1536, 2014.

[103] X. Gao, K. Hidajat & S. Kawi, «Facile synthesis of Ni/$SiO_2$ catalyst by sequential hydrogen/air treatment: A superior anti-coking catalyst for dry reforming of methane,» *Journal of $CO_2$ Utilization,* vol. 15, 146-153, 2016.

[104] J. Juan-Juan, M. C. Román-Martínez & M. J. Illán-Gómez, «Nickel catalyst activation in the carbon dioxide reforming of methane: Effect of pretreatments,» *Applied Catalysis A: General,* vol. 355, 27-32, 2009.

[105] M. Wolters, H. Daly, A. Goguet, F. C. Meunier, C. Hardacre, J. H. Bitter, P. E. de Jongh & K. P. de Jong, «DRIFTS/MS/Isotopic Labeling Study on the NO-Moderated Decomposition of a Silica-Supported Nickel Nitrate Catalyst Precursor,» *The Journal of Physical Chemistry C,* vol. 114, 7839-7845, 2010.

[106] Z. Li, S. Das, P. Hongmanorom, N. Dewangan, M. H. Wai y S. Kawi, «Silica-based micro- and mesoporous catalysts for dry reforming of methane,» *Catalysis Science and Technology,* vol. 8, 2763-2778, 2018.

[107] Z. Navas-Anguita, P. L. Cruz, M. Martín-Gamboa & D. Iribarren, «Simulation and life cycle assessment of synthetic fuels produced via biogas dry reforming and Fischer-Tropsch synthesis,» *Fuel,* vol. 235, 1492-1500, 2019.

[108] L. Wang, T. Qi, Y. Zhang & J. Chu, «Morphosynthesis route to large-pore SBA-15 microspheres,» *Microporous and Mesoporous Materials,* vol. 91, 156-160, 2006.

[109] J. Haber, J. H. Block & B. Delmon, «Manual of Methods and Procedures for Catalyst Characterization,» *Pure & Applied Chemistry,* vol. 67, 1257-1306, 1995.

[110] E.-J. Ras & G. Rothenberg, «Heterogeneous catalyst discovery using 21st century tools: a tutorial,» *Royal Society of Chemistry Advances,* vol. 4, 5963–5974, 2014.

[111] P. A. Webb, «Introduction to Chemical Adsorption Analytical Techniques and their Applications to Catalysis,» *MIC Technical Publications,* 2003.

[112] D. D. LePevelen, «NIR FT-Raman,» de *Encyclopedia of Spectroscopy and Spectrometry*, Academic Press, 98-109, 2017.

[113] A. Mourhly, M. Kacimi, M. Halim & S. Arsalane, «New low cost mesoporous silica (MSN) as a promising support of Ni-catalysts for high-hydrogen generation via dry reforming of methane (DRM),» *International Journal of Hydrogen Energy,* vol. 45, 11449-11459, 2018.

[114] Y. Fu, Y. Wu, W. Cai, B. Yue & H. He, «Promotional effect of cerium on nickel-containing mesoporous silica for carbon dioxide reforming of methane,» *Science China,* vol. 58, 148-155, 2015.

[115] W. Cai, L. Ye, L. Zhang, Y. Ren, B. Yue, X. Chen & H. He, «Highly Dispersed Nickel-Containing Mesoporous Silica with Superior Stability in Carbon Dioxide Reforming of Methane: The Effect of Anchoring,» *Materials,* vol. 7, 2340-2355, 2014.

[116] M. Tang, L. Zhou, M. Du, Z. Lyu, X.-D. Wen, X. Li & H. Ge, «A novel reactive adsorption desulfurization Ni/MnO adsorbent and its hydrodesulfurization ability compared with Ni/ZnO,» *Catalysis Communications,* vol. 61, 37-40, 2015.

[117] N. Wang, X. Yu, K. Shen, W. Chu & W. Qian, «Synthesis, characterization and catalytic performance of MgO-coated Ni/SBA-15 catalysts for methane dry reforming to syngas and hydrogen,» *International Journal of Hydrogen Energy,* vol. 38, 9718-9731, 2013.

[118] B. Huang, X. Li, S. Ji, B. Lang, F. Habimana & C. Li, «Effect of MgO promoter on Ni-based SBA-15 catalysts for combinedsteam and carbon dioxide reforming of methane,» *Journal of Natural Gas Chemistry,* vol. 17, 225-231, 2008.

[119] W. Lin, A. A. Herzing, C. J. Kiely y I. E. Wachs, «Probing Metal-Support Interactions under Oxidizing and Reducing Conditions: In Situ Raman and Infrared Spectroscopic and Scanning Transmission Electron Microscopic-X-ray Energy-Dispersive Spectroscopic Investigation of Supported Platinum Catalysts,» *The Journal of Physical Chemistry C,* vol. 112, 5942-5951, 2008.

[120] C. Mahendiran, D. Rajesh, T. Maiyalagan & K. Prasanna, «Pd Nanoparticles-Supported Carbon Nanotube-Encapsulated NiO/MgO Composite as an Enhanced Electrocatalyst for Ethanol Electrooxidation in Alkaline Medium,» *Energy Technology and Environmental Science,* vol. 2, 11438–11444, 2017.

[121] N. Mironova-Ulmane, V. Skvortsova, A. Kuzmin, U. Ulmanis, I. Sildos, E. Cazzanelli & G. Mariotto, «Magnetic Ion Exchange Interactions in NiO–MgO Solid Solutions,» *Physics of the Solid State,* vol. 47, 1516-1522, 2005.

[122] B. C. Bayer, D. A. Bosworth, F. B. Michaelis, R. Blume, G. Habler, R. Abart, R. S. Weatherup, P. R. Kidambi, J. J. Baumberg, A. Knop-Gericke, R. Schloegl, C. Baehtz, Z. H. Barber, J. C. Meyer & S. Hofman, «In Situ Observations of Phase Transitions in Metastable Nickel (Carbide)/Carbon Nanocomposites,» *The Journal of Physical Chemistry,* vol. 120, 22571-22584, 2016.

[123] Y. Leng, H. Shao, Y. Wang, M. Suzuki & X. Li, «A new method to synthesize nickel carbide ($Ni_3C$) nanoparticles in solution,» *Journal of Nanoscience and Technology,* vol. 6, 221-226, 2006.

[124] A. Hastir, N. Kohli & R. C. Singh, «Ag Doped ZnO Nanowires as Highly Sensitive Ethanol Gas Sensor,» *Materials Today: Proceedings,* vol. 4, 9476-9480, 2017.

[125] Ş. Özkara-Aydınoğlu & A. E. Aksoylu, «A comparative study on the kinetics of carbon dioxide reforming of methane over Pt–Ni/$Al_2O_3$ catalyst: Effect of Pt/Ni Ratio,» *Chemical Engineering Journal,* Vol. 215-216, 542-549, 2013.

[126] B. Zhoufeng, I. Y. Suryawinata & K. Sibudjing, «Highly carbon resistant multicore-shell catalyst derived from Ni-Mg phyllosilicate nanotubes@silica for dry reforming of methane,» *Applied Catalysis B: Environmental,* vol. 195, 1-8, 2016.

[127] J. Ashok, Z. Bian, Z. Wang & S. Kawi, «Ni-phyllosilicate structure derived Ni–$SiO_2$–MgO catalysts for bi-reforming applications: acidity, basicity and thermal stability,» *Catalysis Science and Technology,* vol. 8, 1730-1742, 2018.

[128] C. Macías, M. Haro, J. B. Parra, G. Rasines & C. O. Ania, «Carbon black directed synthesis of ultrahigh mesoporous carbon aerogels,» *Carbon,* vol. 63, 487-497, 2013.

[129] R. V. Siriwardane, M.-S. Shen, E. P. Fisher & J. Losch, «Adsorption of $CO_2$ on Zeolites at Moderate Temperatures,» *American Chemical Society,* vol. 19, 1153-1159, 2005.

[130] S. Sokolov, J. Radnik, M. Schneider & U. Rodemerck, «Low-temperature $CO_2$ reforming of methane over Ni supported on ZnAl mixed metal oxides,» *International Journal of Hydrogen Energy,* vol. 42, 9831-9839, 2017.

[131] D. S. Lee & D. J. Min, «A Kinetics of Hydrogen Reduction of Nickel Oxide at Moderate Temperature,» *Metals and Materials International,* vol. 25, 982-990, 2019.

[132] A. Zhang, A. Zhu, B. Chen, S. Zhang, C. Au & C. Shi, «In-situ synthesis of nickel modified molybdenum carbide catalyst for dry reforming of methane,» *Catalysis Communications,* vol. 12, 803-807, 2011.

[133] H. Ait ahsane, M. Zbair, M. Ezahri, A. Benlhachemi, B. Bakiz, F. Guinneton & J. R. Gavarri, «Structural and Temperature-dependent vibrational analyses of the non-centrosymmetric $ZnMoO_4$ molybdate,» *Journal of Materials and Environmental Science,* vol. 7, 3076-3083, 2016.

[134] Y. Xu, H. Xuan, Y. Gao, T. Liang, X. Han, J. Yang, Y. Zhang, H. Li, P. Han & Y. Du, «Hierarchical three-dimensional $NiMoO_4$-anchored rGO/Ni foam as advanced electrode material with improved supercapacitor performance,» *Journal of Materials Science,* vol. 53, 8483–8498, 2018.

[135] M. Dieterle & G. Mestl, «Raman spectroscopy of molybdenum oxides. Part II. Resonance Raman spectroscopic characterization of the molybdenum oxides $Mo_4O_{11}$ and $MoO_2$,» *Physical Chemistry Chemical Physics,* vol. 4, 822-826, 2002.

[136] T.C. Xiao, A. P. York, V. C. Williams, H. Al-Megren, A. Hanif, X.Y. Zhou & M. L. Green, «Preparation of Molybdenum Carbides Using Butane and Their Catalytic Performance,» *Chem Mater,* vol. 12, 3896–3905, 2000.

[137] M. Takateru, M. Hiramatsu, K. Yamakawa, T. Keigo & H. Masaru, «Fabrication of carbon nanowalls using electron beam excited plasma-enhanced chemical vapor deposition,» *Diamond & Related Materials,* vol. 17, 1513–1517, 2008.

[138] Y. Wu, B. Yang, B. Zong, H. Sun, Z. Shen & Y. Feng, «Carbon nanowalls and related materials,» *Journal of Materials Chemistry,* vol. 14, 469-477, 2004.

[139] V. T. Nguyen, H. D. Le, V. C. Nguyen, T. T. T. Ngo, D. Q. Le, X. N. Nguyen & M. P. Phan, «Synthesis of multi-layer graphene films on copper tape by atmospheric pressure chemical vapor deposition method,» *Adv. Nat. Sci.: Nanosci. Nanotechnol,* vol. 4, 035012, 2013.

[140] M. Baro, P. Nayak, T. T. Baby & S. Ramaprabhu, «Green approach for the large-scale synthesis of metal/metal oxide nanoparticle decorated multiwalled carbon nanotubes†,» *J. Mater. Chem. A,* vol. 1, 482-486, 2012.

[141] Z. Wang, X. M. Cao, J. Zhu & P. Hu, «Activity and coke formation of nickel and nickel carbide in dry reforming: A deactivation scheme from density functional theory,» *Journal of Catalysis,* vol. 311, 469-480, 2014.

[142] K. Wittich, M. Krämer, N. Bottke & S. A. Schunk, «Catalytic Dry Reforming of Methane: Insights from Model Systems,» *ChemCatChem,* vol. 12, 2130-2147, 2020.

[143] E. Akpan, Y. Sun, P. Kumar, H. Ibrahim, A. Aboudheir & R. Idem, «Kinetics, experimental and reactor modeling studies of the carbon dioxide reforming of methane (CDRM) over a new Ni/$CeO_2$-$ZrO_2$ catalyst in a packed bed tubular reactor,» *Chemical Engineering Science,* vol. 62, 4012-4024, 2007.

[144] T. Osaki & T. Mori, «Role of Potassium in Carbon-Free $CO_2$ Reforming of Methane on K-Promoted Ni/$Al_2O_3$ Catalysts,» *Journal of Catalysis,* vol. 204, 89-97, 2001.

[145] A. D. Ballarini, S. R. de Miguel, E. L. Jablonski, O. A. Scelza & A. A. Castro, «Reforming of CH4 with $CO_2$ on Pt-supported catalysts Effect of the support on the catalytic behaviour,» *Catalysis Today,* Vol. 107-108, 481-486, 2005.

[146] X. Li, D. Li, H. Tian, L. Zeng, Z.-J. Zhao & J. Gong, «Dry reforming of methane over Ni/$La_2O_3$ nanorod catalysts with stabilized Ni nanoparticles,» *Applied Catalysis B: Environmental,* vol. 202, 683-694, 2017.

[147] K. Tomishige, O. Yamazaki, Y. Chen, K. Yokoyama, X. Li & K. Fujimoto, «Development of ultra-stable Ni catalysts for $CO_2$ reforming of methane,» *Catalysis Today,* vol. 45, 35-39, 1998.

[148] B. Valle, B. Aramburu, A. Remiru, J. Bilbao & A. G. Gayubo, «Effect of calcination/reduction conditions of Ni/$La_2O_3$–$\alpha Al_2O_3$ catalyst on its activity and stability for hydrogen production by steam reforming of raw bio-oil/ethanol,» *Applied Catalysis B: Environmental,* vol. 147, 402-410, 2014.

[149] K. Liu, X. Xu, J. Xu, X. Fang, L. Liu & X. Wang, «The distributions of alkaline earth metal oxides and their promotional effects on Ni/$CeO_2$ for $CO_2$ methanation,» *Journal of $CO_2$ Utilization,* vol. 38, 113-124, 2020.

[150] Y. H. Hu & E. Ruckenstein, «An optimum NiO content in the $CO_2$ reforming of $CH_4$ with NiO/MgO solid solution catalysts,» *Catalysis Letters,* vol. 36, 145-149, 1996.

[151] Y. G. Chen, K. Tomishige & K. Fujimoto, «Promotion in Activity and Stability of Nickel-Magnesia Solid Solution Catalyst by Structural Rearrangement via Hydration for Reforming of $CH_4$ with $CO_2$,» *Chemistry Letters,* vol. 26, 999-1000, 1997.

[152] P. K. Davies & A. Navrotsky, «Thermodynamics of Solid Solution Formation in NiO-MgO and NiO-ZnO,» *Journal of Solid State Chemistry,* vol. 38, 264-276, 1981.

[153] S. M. Masoom Nataj, S. M. Alavi & G. Mazloom, «Catalytic performance of Ni supported on ZnO-$Al_2O_3$ composites with different Zn content in methane dry reforming,» *Journal of Chemical Technology and Biotechnology,* vol. 94, 1305-1314, 2019.

[154] J. A. North, A. B. Narrowe, W. Xiong, K. M. Byerly, G. Zhao, S. J. Young, S. Murali, J. A. Wildenthal, W. R. Cannon, K. C. Wrighton, R. L. Hettich & R. F. Tabita, «A nitrogenase-like enzyme system catalyzes methionine, ethylene, and methane biogenesis,» *Science,* vol. 28, 1094-1098, 2020.

[155] A. Rabii, A. Saad, Y. Dahman & E. Elbeshbishy, «A Review on Anaerobic Co-Digestion with a Focus on the Microbial Populations and the Effect of Multi-Stage Digester Configuration,» *Energies,* vol. 12, 1106, 2019.

# Annexes and Appendices

# Annex A:

# Bimetallic catalysts and alkalinity on DRM

Nickel and platinum catalysts showed little to no difference in their ability to convert methane and $CO_2$. However, Raman analyses suggest the existence of smaller disordered carbon deposits in the Ni-Pt material. Thus, Pt could be providing an important effect in the long run. Smaller carbon deposits are explained by the ability of Pt to catalyze the conversion of carbon back to partially hydrogenated carbon, which does not occur as frequently over Ni, as reported by Schulz *et al.* (2015). Pt has a smaller tendency to convert carbon into CO, which is in opposition to the capabilities of Ni [142]. However, both metals are very able to convert $CO_2$ into CO via different pathways, which depend on ionized oxygen or OH over an active site (marked as *). Ni is capable if inducing a dissociative adsorption in $CO_2$, opposed to Pt, which can only transform this reactant with help of other intermediates. As noted previously, the active phase can eliminate carbon deposits if contact exists with the active phase. Carbon elimination processes involve hydrogenation (methanization), gasification (needing water or OH intermediates) and the reverse Boudouard reaction. This ability is augmented when the active phase is partially confined in pores of the material. The importance of active sites is not to be underestimated, as catalytic mechanisms depend on neighboring atoms to perform the transformation of reactants. Now, Pt and Ni are reportedly highly effective when used together, due to their capabilities of undergoing surface reconfiguration, as layers of both can intercalate or become fully mixed (intercalated atoms) when heated, and then reorganize once again when coming into contact with oxygen (adsorbate). Their combined use can thus prevent or decrease the deposition of carbon and improve the conversion of $CO_2$.

The rate-determining step in DRM remains somewhat unclear, although the consensus has focused on the dissociative adsorption of methane, which has been demonstrated for surfaces with an oxygen lattice. This knowledge is helpful when analyzing the capabilities of some materials containing metallic oxides, such as MgO. This alkaline compound tends to form solid solutions, which result in stronger interactions with nickel. Material NiPt-MgOCach was highly stable, especially in the short-term studies, which have already been explained previously. A surface containing Ni, Pt and MgO and solid solutions is highly capable of adsorbing and transforming $CO_2$ and $CH_4$, as well as preventing sintering. It should be noted that not all oxides can form solid solutions, and that some solid solutions can create too strong of an interaction with the active phase, which can adsorb but materials but not desorb them. Further surface reactions occurring during DRM are shown below, which have been demonstrated previously [143].

$$CH_4 + 2^* \rightleftarrows CH_3^{(*)} + H^* \quad \textbf{(R8)}$$

$$CH_3^{(*)} + {}^* \rightleftarrows CH_2^{(*)} + H^* \quad \textbf{(R9)}$$

$$CH_2^{(*)} + {}^* \rightleftarrows CH^{(*)} + H^* \quad \textbf{(R10)}$$

$$CH^{(*)} + {}^* \rightleftarrows C^{(*)} + H^* \quad \textbf{(R11)}$$

$$C^* + O_x \rightleftarrows CO + O_{x-1} + {}^* \quad \textbf{(R12)}$$

$$CO_2 + O_{x-1} \rightleftarrows O_x + CO \quad \textbf{(R13)}$$

$$4H^* \rightleftarrows 2H_2 + 4^* \quad \textbf{(R14)}$$

$$H_2 + O_x \rightleftarrows O_{x-1} + H_2O \quad \textbf{(R15)}$$

Regarding alkalinity, the role of alkaline materials in DRM has been extensively researched in the past. The explanations provided evolve around the crystalline geometry or the electronic nature of the basic materials. The presence of an alkaline material can reduce the chances of a $CH_4$ molecule adhering to a surface and can interfere with the rate of carbon formation and the reforming rate [144]. This was the case for material NiPt-MgOCach. It was believed initially that alkaline materials could increase the amounts of adsorbed oxygen once $CO_2$ was chemisorbed and dissociated (forming CO). In theory, adsorbed oxygen should contribute to increasing the oxidation of methane (an existing mechanism), which can reduce the formation of carbon (see figure 37)]. However, once this was proven to be false, other possible perspectives were analyzed, such as the importance of alkaline groups in reducing the size of nickel particles.

The addition of promoters can improve catalytic activity even for noble metals [145]. A relationship between alkalinity and to chemisorb $CO_2$ is suggested once again. Alkaline regions, having a natural affinity for $CO_2$, tend to evade $CH_4$. Therefore, carbon deposition can be completely suppressed when the active phase of a catalyst is dispersed into a metal oxide with a strong Lewis basicity. That is, a strongly alkaline support (and without amphoteric properties), will provide an increased resistance to carbon formation. Surfaces devoid of alkaline metal oxides are those that will react with $CH_4$, as nickel in strongly alkaline areas will be surrounded by $CO_2$ molecules. In this way, methane will be forced to look for areas with low basic presence in order to be chemisorbed. $CO_2$, on the other hand, will go directly to CO, thanks to the low carbon that is being deposed on the surface of the catalyst.

There are cases where acid supports have been used in conjunction with alkaline promoters, which show a large reduction in accumulated carbon, compared to materials supported only on the acid material. The role that strongly alkaline materials play is based on an intense adsorption of $CO_2$ species, which react easily with deposited carbon. Figure 37 shows the mechanism by which $CO_2$ and $CH_4$ and carbon deposits will transform into CO and $H_2$.

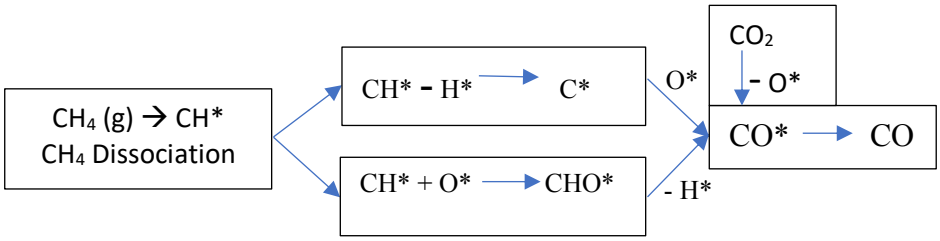


**Figure 37.** Possible dissociation routes of methane and $CO_2$ during DRM **[72]**.

One of the most explored alkaline metals is $La_2O_3$, which has interesting peculiarities that can perhaps be compared to other alkaline oxides such as MgO. For example, a correlation between calcination and reduction temperatures in a mixture of NiO with $La_2O_3$ was found. As calcination temperatures increase, the NiO content tends to decrease, whereby a bimetallic oxide ensues. Therefore, the reduction of this mixed oxide tends to become more difficult [146]. Mixed oxide formation is very common in other materials, and similar results are also available for MgO and NiO [147]. The difficulty in reducing materials by increasing calcination and reduction temperatures has also been observed in mixtures of NiO, $La_2O_3$ and $Al_2O_3$ [148]

Now, a solid solution refers to a temporarily liquid mixture of metals, which when crystallized forms a single crystalline structure. With special reference to the use of MgO, it

is known that this material has the ease of generating solid solutions at high temperatures with the NiO. Both materials have the same crystal structure.

A solid solution of these materials will usually result in weak and moderate alkaline sites on the material´s surface. Induction of $CO_2$ methanation have been linked to both weak and moderate sites, whereas activity of the catalyst has only been related to the moderate ones [149]. These properties result in a mixture highly resistant to carbon deposition. The existence of a solid solution is easily provable by $H_2$-TPR analysis, where fractions of a material are shown to be reducible only at higher temperatures. The rest of the material will likely have peaks in hydrogen consumption at reduction temperatures within a more "normal" range, especially for NiO, as demonstrated in this thesis in the NiPt-MgOCach material. In this particular case, the maximum calcination temperature was limited to 500 °C, and it can be speculated that, had higher temperatures been used, there would have been a higher fraction of NiO/MgO solid solution. Within solid solutions, only a fraction of the NiO will be reducible, resulting in smaller nickel particles. A smaller particle size then results in less carbon deposition, as has already been discussed in previous chapters. Nickel particles have been shown to become so tiny in a solid solution that even high-resolution microscopy cannot contribute to the detection of reduced metal. The behaviors of solid solutions have been visualized in other metal pairs, with which carbon-free surfaces have been effectively predicted.

A relationship has been defined between high conversions of reactants and the composition of the solid solution (percentages of NiO in the mixture), synthesis conditions of the same, and properties of the MgO. It has been recognized that it is important to find a nickel range that is sufficiently available for the reaction surface, but that prevents the start

of sintering processes. In this way, it is believed that using between 7 and 22.5% Ni, will result in highly stable catalysts [150]. A study conducted by Chen *et al.* (1997) stated that a post-synthesis treatment with distilled water to a 7% Ni catalyst charred at 950 $^{o}$C can generate a catalyst with a high CO formation rate, and a low rate of deposed carbon [151]. This same catalyst was used in another study, where zero carbon formation was reported after 2 hours by thermogravimetric analysis [147]. On the other hand, interesting studies were made in terms of carbon formation analysis, where a clear distinction was made between alfa- and beta-carbon, where alfa-type formations are highly reactive particles, from which CO arises. They conclude that alfa-carbon is a fragmented CH4 cluster on the nickel surface, where even carbonate and methane species can occur. Beta-carbon is more difficult to remove and is the one that tends to disable catalysts [151].

According to multiple studies of Hu and Ruckenstein, an acceptable surface area for catalysts with MgO is approximately 50 $m^2/g$. This is a value very close to the one reported for NiPt-MgOCach material in this thesis. Another factor that has a great weight in the decomposition of the reactants (especially $CH_4$) is the presence of nickel alloys with some noble metal, which is also a likelihood for NiPt-MgOCach.

The influence of the crystal structure is of great importance, although there are also other important variants. A similarity in atomic radii, electronegativity and oxidation numbers will result in better solid solutions. These parameters are reviewed below.

If the crystal structure is different in nature, more energy is required to get into the minority group (in percentage), due to the need to rearrange atoms, rather than simply incorporating it into the solution. On the other hand, a big difference in electronegativity will result in the formation of new compounds, rather than solid solutions. In cases where the

difference in electronegativity is too high, the probability of an ion bond is increased. The atomic radius can have an influence due to the internal tension that may occur within the atomic lattice, in case the difference in atomic radius is too large. Too much stress will require too much energy, so the system is unsustainable, and very little metal could enter the solid solution. Finally, an excess of electrons is more tolerable than a deficit of them, so metals with higher oxidation numbers will dissolve better in a metal with lower oxidation number.

Before ending this chapter, an attempt will be made to explain the use of ZnO as a support for DRM reaction, as well as why in certain cases it was a total failure. First, the case in which nickel was used only with ZnO as a support, and subsequently cases where nickel was used with ZnO and Cach, will be reviewed. Finally, the case in which nickel with molybdenum and ZnO was used will be reviewed briefly. Unfortunately, the short duration of the experiments (maximum of 5 h) does not allow further assertions.

The nanoparticulate ZnO proved to be a support that initially provides acceptable conversions. However, it is a material that, although very difficult to reduce, allows a slow sintering of the active phase. This is explained by the very low surface area of the Ni-$Z_{np}$ catalyst (8.3 $m^2/g$).

The following cases are those in which ZnO was used in conjunction with Cach mesoporous silica. A total of 3 materials were used for the reaction, none of which offered a conversion greater than 10% for any reactant. The effect in these cases was the opposite of what was observed with the addition of MgO, so it should be assumed that these materials are of very different properties and tend to behave differently when used in conjunction with NiO. Upon observing information on NiO and ZnO lattice parameters, it is relatively easy to predict that solid solutions are difficult to create. It has been reported that the solid solutions

of these two compounds are formed only from 1000 °C at atmospheric pressure, provided that there is at least 60% NiO in the mixture [152].

One of these materials had macroporous silica content, which demonstrated its null effectiveness for DRM (Ni-ZnOAld-C). In the case of the other two materials (Ni-$Z_{np}$Cach and Ni-$Z_{np}$Cach-2), they were supported on the Cach silica, and resulting specific surface area was above 100 $m^2/g$. However, there was no catalytic activity. In addition to the low probabilities of a solid solution, it was shown that new compounds were formed, which likely reduced catalytic activity. In addition, they were more difficult components to reduce, as demonstrated by $H_2$-TPR.

The synthesis of these two materials was simply through a physical mixture of ZnO with Cach, and then incorporating the NiO by incipient wet impregnation. This differs from the method used by Masoom Nataj *et al.* (2018), who synthesized zinc aluminates using a co-precipitation method of precursors under strongly alkaline pre-calcination conditions [153]. This study further demonstrates that it is important to add low amounts of zinc, to avoid losses in the surface area, something that was also very noticeable in this thesis. It is highly likely that an ineffective method has been used in this work, and a reaction between $SiO_2$ and ZnO is unlikely.

To complete the analysis of catalytic materials with ZnO, the case of nickel, molybdenum and ZnO is briefly mentioned. Due to the formation of multiple compounds, it is likely that more than one of them had catalytic activity. However, the most common material was ZnO, with which sintering processes were inevitable. Also, metal dispersion was very likely poor, due to the low specific surface area in the material. The carburized version of this material had a similar activity, probably thanks to the formation of nickel and

zinc carbide. However, it is demonstrated by the works of Brungs *et al*. (1999), that the disappearance of the carburized phase is a matter of time, unless carbide is protected from oxidative processes. A decrease in the amount of carbon in the NiMo-$Z_{np}$-C material was observable thanks to Raman spectroscopy analysis.

To conclude this section, details are yet to be elucidated in terms of the contributions that the ZnO may make. Thanks to the low number of reports with this metal oxide, it is still possible to be a pioneer in DRM with these materials. It is of the utmost importance to understand the effect of the ZnO synthesis method and some accompanying support before being able to make more positive contributions with this alkaline material. Thus, it is also necessary to understand the use and formation of solid solutions that could allow this metal to be more easily useable.

# Annex B: Biogas Generation

## Generalities

This chapter will begin by mentioning a few details that should be kept in mind throughout the chapter.

- Methodology included in this section is merely descriptive, as most experiments that were undertaken at Hochshule Emden/Leer (University of Applied Sciences), were not part of this doctoral dissertation.
- The work carried out in Emden, Germany, was done in collaboration with M. Eng. Lena Peters, as part of her doctoral thesis. Thanks to this collaboration, many crucial elements pertaining to the production of biogas were approached.
- The methods described briefly herein are not of interest for DRM, which is why they were not included in chapter 3.
- In the hope that similar work can be undertaken at UNICACH-IIIER, this chapter is written out as a technical report, as opposed to a profound study.

.

## Biogas generation and Flexibla project

Flexibla project is a project taking place between Hochschule Emden-Leer and some companies that shall not be disclosed. Flexibla has as its main objective to prove that a modification of feed amounts can have an impact on biogas generation, i.e.,when fed less, less biogas will leave the biodigester and vice versa. If the objectives are successful, biogas could serve as a temporary substitute for seasons when less solar and wind energy are generated in Germany.

Practically any substrate can generate biogas, if it is in contact with an appropriate inoculum. That is, if microbiota dominating the inoculum are mostly methanogenic bacteria. Substrates can be of different origin, both animal and vegetal. Vegetal samples can be dry

straw and silage, whereas animal samples can be any waste from the food industry, such as bread meal, milk whey, or seafood. In general, vegetal materials will generate biogas that is quite balanced in its content of $CH_4$ and $CO_2$, although methane may dominate slightly. Whey can also generate a balanced mixture. Balanced mixtures of methane and $CO_2$ are usually related to high carbohydrate contents. Biogas with a higher content of fat are likely to generate more methane.

## Development stages in biodigesters

Production of biogas is a completely anaerobic process that occurs in waste materials. This anaerobic digestion is a process that involves a seemingly coordinated chain of events by different groups of bacteria. Initially, molecules with a high molecular weight must be broken down by hydrolytic bacteria. Ensuing monomers and oligomers will be transformed into short-chain acids and alcohols, which is why the second stage is termed acidogenesis. Among these organic acids, propionic acid, lactic acid, acetic acid can be found. Acids formed during acidogenesis then transform mostly into acetic acid, although hydrogen and $CO_2$ can also ensue. The final stage is known as methanogenesis, whereby acetic acid is transformed into methane by methanogenic Archaea, which is known as the acetoclastic route. It is interesting to note that there are recent findings where bacteria have been reported to be involved in the production of methane via nitrogenase-like enzymatic systems, albeit not necessarily in biodigesters [154]. Also, hydrogen is partly consumed and can also give rise to more methane, which is a step performed by hydrogenotrophic Archaea. A reaction that takes place before methanogenesis is homoacetogenesis, whereby acetic acid is generated by a reaction between $CO_2$ and hydrogen or viceversa [155]. Like traditional catalysis, there is also a rate-limiting step in this chain of events, which is usually

methanogenesis, although this can change when processing materials with a high content of lignin. In such cases, hydrolysis is the rate-limiting step [20].

## Main activities regarding biodigesters

Activities at Hochschule Emden regarding biodigesters are described below.

a) Large reactor.
    a. Flexible feeding with corn silage before 8 in the morning.
    b. Flexible addition of trace metals to reactor.
    c. Keeping record of produced biogas volume
    d. Filling water bath that keeps system at 45 °C.
    e. Changing adsorption silica gel pearls that prevent moisture from entering biogas sensors.
    f. Changing adsorption of material that eliminates $H_2S$ from biogas output.
    g. Pouring silicon oil into biogas counter.
b) Small reactor
    a. Fixed feeding briefly after 8 AM and briefly after 4 PM with corn silage.
    b. Adding fixed amount of trace elements to reactor.
    c. Keeping record of produced biogas volume.
    d. Filling water bath.
    e. Pouring silicon oil into biogas counter.

## Ankom systems

The Ankom Gas Production Measurement System is a design that allows total gas production to be monitored. It does not make a distinction between produced gases, as it only reports cumulative pressure via software. It is a highly useful technique for quantifying the amount of biogas that is being generated in small batch tests.

## VOA/TIC and pH value of inoculums

VOA/TIC is a ratio between volatile acids and inorganic carbon. This can also be known by the German term FOS/TAC, meaning *Flüchtige Organische Säuren*/*Total Anorganische Carbonat*. This is translated as volatile organic acids/total inorganic carbonate and is a measure of the buffering capacity of the biodigester. Values below 0.2 and 0.6 are regarded as too little and too much feed going into the biodigester, respectively, although some exceptions to this range exist. An optimal FOS/TAC ratio will be between 0.3 and 0.4. It is important to keep these values as controlled as possible, as they serve as a forewarning of over or underfeeding of the biodigester, which can eventually lead to a loss of the experiment. An excess of volatile acids can inhibit methanogenic Archaea.

Before being able to carry out these determinations, inoculum was first pumped out of the biodigesters (between 400 and 800 mL). Once inoculum was available, both VOA/TIC and pH values could be determined on a HACH biogas titration manager equipment (HACH, USA). VOA/TIC is basically a titration with diluted sulfuric acid, and the endpoint of titration is near a pH value of 4.5. However, titration is performed automatically.

## Proximate and Van Sosten analyses

Proximate analysis (also called Weende) is a traditional set of tests that can quantify moisture, ashes or mineral content, crude fat content, crude protein content and crude fiber content. Also, by simple subtraction from a 100% value (original weight), a nitrogen-free extract can be calculated, which is basically all carbohydrates that cannot be determined otherwise.

Moisture is a very simple test, whereby sample is placed in small trays or crucibles and allowed to dry overnight at 100 °C. The dried samples can be used for all other analyses. In order to determine the ash content, a dry sample must be calcined at 550 °C for up to 5 hours. Crude fat content is carried out with petroleum ether with help of a Soxhlet extraction equipment. Fat extraction continues for an estimated 6 hours.

Crude protein is somewhat more complicated, as there are 3 main stages in the Kjeldahl method. The first of these involves a digestion with sulfuric acid, followed by neutralization with a NaOH solution and finally a titration with HCl 0.1 M. As for crude fiber, this component is determined in two stages, the first in a partial digestion with diluted sulfuric acid, and afterwards in a NaOH solution.

Finally, Van Sosten analyses are all related to cell wall contents and are divided into neutral detergent fiber (NDF), acid detergent fiber (ADF) and acid detergent lignin (ADL). In general, the following can be said about these components:

a) A low content of ADF means that a sample is easy to digest by bacteria. A low value of ADF will mean a higher content of NDF, which can be interpreted as easily degradable hemicellulose.
b) Cellulose content is the result of subtracting ADL from ADF.

c) ADL is the content of lignin. A high content of lignin can be interpreted as a substrate that is difficult to degrade.

These analyses are carried out in a similar manner to that of crude fiber, whereby only the solution needed for digestion changes.

# Annex C: Cach information

This thesis has mesoporous silica Cach and metallic nickel as its most important materials. However, there is a combination of factors that was explored in parallel during DRM. The presence of non-mesoporous materials, alkaline materials, carbon and the use of platinum and molybdenum are also factors to be reckoned with.

A complementary section was the study of the relationship between mesoporous materials and carbon deposits that appear during DRM.

The Cach material was without a doubt one of the most interesting surprises of all this work. It has neither the surface area nor the degree of organization of a material such as SBA-15, but it demonstrated satisfactory qualities for DRM. Among the peculiarities of the synthesis are the use of ambient temperature (approximately 35 °C) and trimethylbenzene. Trimethylbenzene is generally used as a pore expander at higher temperatures but had a significant effect regardless. Another peculiarity of this synthesis is post-synthesis heat treatment. The synergistic effect resulting from the combined use of trimethylbenzene and heat treatment has been previously reported. The measurable response is pore size and volume. A larger pore size provides expanded capabilities in a media, which directly translates into the ability to introduce larger quantities of some secondary support or active phase.

It is highly likely that the application of mesitylene was the material that defined the capacities of the Cach material as a proper support for active phases. However, it is also

likely that the attractive features of Cach would not have been developed without a post-synthesis thermal treatment.

The characteristics of Cach material are those of a mesoporous support. It has a mean pore diameter of 5 nm, and the $N_2$-physisorption isotherms reveal a highly disorganized material. The specific surface area is between 450 and 475 $m^2/g$. It should be mentioned that the process used in making this material is reproducible. The described features are maintained between one synthesis and another. Since the synthesis temperatures of an organized material such as SBA-15 are almost threefold higher, a variation of two or three degrees in Cach synthesis will most likely not result in major changes.

# Appendix 1:
# Mathematical Deduction for Equilibrium constants

Equilibrium constants for DRM reaction were calculated for different temperatures and pressures, as well as for variations in methane, $CO_2$ and argon (diluent) quantities. The required thermodynamic information was obtained from HSC Chemistry 5.11 (Pori, Finland) software. In order to know the constants, it was necessary to know the maximum conversion of the limiting reagent (which was arbitrarily assigned to $CH_4$). For this purpose, formulas were introduced in the Excel software, where equations were solved for a specific cell using the "Find Target" function (Buscar objetivo under Análisis de Hipótesis in Spanish commands). The mathematical formula and its deduction are broken down below.

$$e^{-\Delta G^{\circ}_T/RT} = K_a \qquad \textbf{(Eq. 4)}$$

$$K_a = \frac{[(Y_c P)^{\gamma_c}]}{[(Y_a P)^{\gamma_a}]} x \frac{[(Y_d P)^{\gamma_d}]}{[(Y_b P)^{\gamma_b}]} \qquad \textbf{(Eq. 5)}$$

Where $Y_c$ and $Y_d$ represent the molar fraction of C and D. Likewise, $Y_a$ and $Y_b$ represent the molar fraction of reagents A and B. Multiplied by P, the result represents partial pressures. $\gamma$ represents the number of moles within the original equation. In the case of DRM, $\gamma_c$ and $\gamma_d$ have each a value of 2, whereas $\gamma_a$ and $\gamma_b$ have a value of 1.

Now, each molar fraction can be expressed in terms of the reagents, as will be seen in next page.

The following deduction takes A as the limiting reagent. X represents the conversion of the limiting reagent in the equilibrium state.

Initial Moles for $A = A_0$

Moles for A at a given time [A(t)= $A_0 - X A_0$

Initial Moles for $B = B_0$

Moles for B at a given time [$B$(t)= $B_0 - XA_0$]

Initial moles for $C = 0$

Moles for C at a given time [$C(t) = 2XA_0$]

Moles for $D = 0$

Moles for D at a given time [$D(t) = 2XA_0$]

Introducing Argon into the equation will give us a new value, which is $E_0$, and remains unchanged during the reaction.

Total initial moles are expressed as $A_0$+$B_0$+$E_0$, which can be condensed as $N_0$.

Total moles at any given time result from adding moles at a given time for A, B, C, D and E.

Total moles [$N_T$]= $A_0$ - $X$$A_0$ + $B_0$ -$X$$A_0$ + 2$X$$A_0$ + 2$X$$A_0$ + $E_0$ = $\mathbf{N_0 + 2XA_0}$

Substituting these values in Eq. 5, we have the following result.

$$K_a = \frac{\left(\frac{2xA_0(P)}{N_0 + 2XA_0}\right)^2 \left(\frac{2xA_0(P)}{N_0 + 2XA_0}\right)^2}{\left(\frac{A_0(1-x)(P)}{N_0 + 2XA_0}\right)^1 \left(\frac{(B_0 - xA_0)(P)}{N_0 + 2XA_0}\right)^1} \qquad \textbf{(Eq. 6)}$$

Substituting $A_0$ for $CH_4$ and $B_0$ for $CO_2$, we arrive at Eq. 7.

$$\frac{(2CH_4X)^4}{(N_0+2XA_0)^2(CH_4(1-X))(CO_2-CH_4X)}P^2-(e^{-\Delta G/RT})=0 \qquad \textbf{(Eq. 7)}$$

The value taken for P in these calculations was 0.76 atm, which is the atmospheric pressure in Mexico City, where all DRM experiments were carried out.

Once all these values have been correctly inserted into Excel, the following should be done:

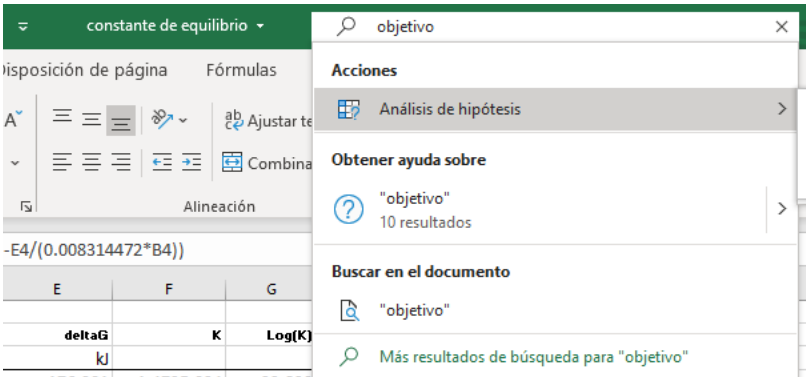


Once the Find Target window is open, a value near zero should be inserted as the desired value for the defined cell. The cell that is to be modified (which will be the conversion value), must also be defined.